Development of High Fidelity Digital Inline Holographic Particle Tracking Velocimetry for 3D Flow Measurements

A DISSERTATION
SUBMITTED TO THE FACULTY OF
UNIVERSITY OF MINNESOTA
BY

Mostafa Toloui

IN PARTIAL FULFILLMENT OF THE REQUIREMENTS
FOR THE DEGREE OF
DOCTOR OF PHILOSOPHY

Advisor: Jiarong Hong

March 2016

Acknowledgements

First of all, I would like to express my sincere gratitude to my adviser Professor Jiarong Hong, who unconditionally supported my academic endeavors and paved the way in all stages of my PhD research. Through him, I have gained insight and perspective to approach scientific research problems and had the opportunity of working on a variety of extraordinary research projects. I consider myself very privileged to have him as my academic advisor who has been guiding, supportive and encouraging of my freedom to pursue my ideas in the research.

During my PhD, I have had the pleasure of collaborating with a great number of outstanding faculties and researchers (Prof. Fotis Sotiropoulos, Prof. Michele Guala, Prof. Leo Chamorro and Prof. John Sartori, Dr. Wing Lai and Dr. Dan Troolin) that I am incredibly thankful for their time and fruitful scientific discussions.

I also want to thank Professor Terry Simon who has kindly accepted to serve as the chair of my thesis committee. I would like to send my appreciations to other members of my thesis committee, i.e. Professor Fillipo Coletti and Professor Cari Dutcher, for agreeing to serve in the committee and providing useful feedback.

Furthermore, I would like to thank Professor James Leger and Professor Ellen Longmire who have always been inspiring teachers to me and the doors of their offices have been always open for discussion and guidance.

In addition, I would like to thank all members of the flow field imaging lab for their help, discussions and feedback during my PhD research: David Brajkovic, Kevin Mallery, Santosh Kumar, Teja Desari and Nolan St. John.

Over the course of my life, I have been always very fortunate to have wonderful and supportive friends that I am greatly thankful to. Here, I want to thank Hamzeh Kheradmand, Elizabeth Tammen, Amin Tadayon, Pietro Ferrero, Hamidreza Badri, Mohammad Ebtehaj, Pouya Hemmati, Davide Giannuzzi, Taher Ghasimakbari, Mammad Nasiri, Eyoab Zegeye, Andras Nemes, Omid Amili, Deepak Adhikari, Yan Ming Tan, Kyle Winters, I consider myself very lucky for having you in my personal and academic life.

Finally I must thank my wonderful family for always dropping everything whenever I needed them and being there for me through the best and worst of my life. I

deeply believe that I would have never reached this goal if it was not for their tremendous love, support and encouragement.

This work was supported financially by the startup package of Prof. Hong, my MnDrive and Interdisciplinary Fellowships all from University of Minnesota.

Dedication

To my lovely parents, Aliakbar Toloui and Khoshghadam Sharghi Tabrizi, and my amazing brother, Morteza Toloui, for their tremendous love, inspiration and support.

Abstract

Three-dimensional non-invasive measurement capability is often a necessity to unravel the physical phenomenon in fluid mechanic problems such as flow field characterization in wall-bounded turbulent flows and microfluidic devices. Among all the 3D optical flow diagnostic techniques, digital inline holographic particle tracking velocimetry (DIH-PTV) provides the highest spatial resolution with low cost, simple and compact optical setups. Despite these advantages, DIH-PIV suffers from major limitations including poor longitudinal resolution, human intervention (i.e. requirement for manually determined tuning parameters during tracer field reconstruction and extraction), limited tracer concentration, small sampling volume and expensive computations. These limitations have prevented this technique from being widely implemented for high resolution 3D flow measurements. In this study, we present our novel high-fidelity DIH-PTV algorithm with the goal of overcoming all the above mentioned limitations. Specifically, the proposed particle extraction method consists of multiple steps including 3D reconstruction, 3D deconvolution, automatic signal-to-noise ratio enhancement and thresholding, particle segmentation and centroid cacluation, and inverse iterative particle extraction. In addition, the processing package is enriched with a multi-pass 3D tracking method and a cross-correlation based longitudinal displacement refinement scheme. The entire method is implemented using GPU-based algorithm to increase the computational speed significantly.

Validated with synthetic particle holograms, the proposed method can achieve particle extraction rate above 95% with ghost particles less than 3% and maximum position error below a particle diameter for holograms with particle concentration above 3000 particles/mm^3 within sampling volumes of ~1 mm longitudinal length. Such improvements will substantially enhance the implementation of DIH-PTV for 3D flow measurements and enable the potential commercialization of this technique. The applicability of the technique is validated using the experiment of laminar flow in a microchannel and the synthetic tracer flow fields generated using a DNS turbulent channel flow database. In addition, the proposed method is applied to smooth- and rough-wall turbulent channel flows under two different settings of high-resolution near-wall and whole-channel measurements (i.e.

sampling volume is extended to the entire depth of the channel). In the first case, using a microscopic objective and local seeding mechanism, DIH-PTV resolves near-wall flow structures within a sampling volume of $1 \times 1.5 \times 1$ mm^3 (streamwise × wall-normal × spanwise) with velocity resolution of ~100 μm (vector spacing). In the second case, the measurement volume is extended to the whole-channel depth by seeding the entire channel. Under this setting, the 3D velocity fields are obtained within a sampling volume of $14.7 \times 50.0 \times 14.4$ mm^3 with a velocity resolution of ~ <1.3 mm per vector, comparable to other the-state-of-the-art 3D whole-field flow measurement techniques. Overall, the presented DIH-PTV measurements under two different settings highlight the potential of DIH-PTV to obtain 3D characterization of the turbulent structures over a full range of scales, covering both the near wall and the out-layer regions of wall-bounded turbulent flows.

Table of Contents

List of Figures

Chapter 1: Introduction

The study of wall-bounded turbulent flow plays a critical role in a variety of engineering applications including aerodynamics, heat transfer, turbomachinery, and pollutant transport. For instance, more than 48% of the total drag acting on a flying airplane comes from skin friction (Dean and Bhushan 2010), and any improvements to achieve more efficient flight control strategies demand a better characterization of flow physics in the near-wall. These flows are often defined in terms of the characteristics and interactions of their 3D flow structures, which cover a broad spectrum in scales whose range varies at different distances away from the wall. These features necessitate measurement techniques with three-dimensional, non-invasive and whole-field capabilities to experimentally characterize turbulent flows, making wall-bounded turbulent flow measurement one of the most challenging areas of experimental fluid mechanics. Contrary to point-wise measurement techniques (e.g. hot-wire anemometry, laser Doppler velocimetry), particle image velocimetry (PIV) is an optical method that provides a whole-field non-intrusive measure of the fluid motion and arguably the most popular optical technique currently in use. However, its implementation in three dimensions (3D) faces many challenges and remains an active research area. Specifically, the widely-used 3D PIV techniques – including scanning PIV (Brücker 1992), defocusing PIV (Willert and Gharib 1992), and tomographic PIV (Elsinga *et al.* 2006) – require expensive and complicated optical set-ups (multi-view or scanning components). In addition, they are still insufficient in their ability to resolve inherently 3D and unsteady turbulent structures and flows near solid boundaries due to the limited spatial or temporal resolutions. A more complete discussion of each of these techniques' restrictions and complexities and a comprehensive review on their applications to wall-bounded turbulent flow measurements are provided in Chapter 2 of this dissertation.

Turbulent flow measurement is not the only field in experimental fluid mechanics where the 3D dimensionality of the flow phenomenon imposes challenges and limitations on the implementation of particle image velocimetry. For example, in microfluidic systems, where the relevant length scales range in the submillimeter domain, the out-of-plane motion of tracer particles results in a considerable level of measurement noise and

uncertainty for micro PIV (μPIV) applications. This motion in microfluidics is mainly caused by the Brownian diffusion or even the 3D features of the device (e.g. flow in micromixers or micropumps). Notably, these motions are relevant and important characteristics of the flow physics in microfluidic devices. In attempts to overcome this issue, stereo and confocal imaging concepts have been integrated into μPIV systems (e.g. Lindken *et al.* 2006. and Lima *et al.* 2006). Nevertheless, confocal and stereo μPIV configurations are still limited in their ability to resolve the micro-scale flows with adequate spatial and temporal resolution. Specifically, the temporal resolution of confocal microscopy is constrained by the hardware speed involved in the scanning mechanism. Stereo implementation in μPIV also suffers from conflicting requirements between the spatial resolution and accuracy of the out-of-plane velocity component (Wereley and Meinhart 2010) because high spatial resolution necessitates using objective lenses with high numerical aperture (NA) which consequently limits the off-axis viewing angle.

These examples and many other examples in fluid mechanics highlight the importance and constant need for development and improvement of 3D PIV/PTV measurement techniques for full understanding of the underlying flow physics in different flow problems.

1.1 Background and Motivation

Digital holography is a 3D imaging technique capable of capturing 3D information in a single acquisition. This technique in an inline configuration can provide a simple and low-cost solution for simultaneous 3D optical sensing of shape, concentration and velocity. Specifically, digital inline holographic imaging set-up includes a single camera and a laser source with low power and coherence level requirements. In addition to low cost optical components, inline holography benefits from an easy image calibration and a simpler and more stable optical set-up, and can provide optical sensing to regions with limited optical access (due to its single axis imaging set-up). Digital inline holography (DIH) also has a great potential for miniaturization and integration with other measurement and field monitoring devices (e.g. microscopes and submersible ROVs). These advantages has made DIH one of the best solutions for 3D imaging in a wide range of applications including microbiology (e.g. Burns *et al.* 2007 and Hong *et al.* 2012), low cost bio-sensing device development (e.g. Seo *et al.* 2009 and Im *et al.* 2015), methodology (e.g. Kaikkonen *et al.* 2014 and Beals *et al.* 2015), field chemical and biological monitoring (e.g. Graham *et al.*

2010 and Sullivan *et al.* 2011), 3D micro PIV (e.g. Singh and Panigrahi 2015) and etc. Notably, in combination with particle tracking velocimetry (namely DIH-PTV) and a microscopic setup, this technique has been provided superior resolution compared to all other 3D techniques for wall-bounded turbulent flow measurements (e.g. Sheng *et al.* 2008 and Talapatra and Katz 2013).

Despite all these advantages, its application for 3D flow measurements is severely restricted by a number of limitations including poor longitudinal resolution, human intervention (i.e. requirement for manually determined tuning parameters during tracer field reconstruction and extraction), limited tracer concentration, small sampling volume and expensive computations. These limitations prevent this technique from being widely implemented for high resolution 3D flow measurements. In this study, we present our work on improving holographic PTV algorithm with the goal of overcoming the abovementioned limitations. Our new DIH-PIV processing method has been successfully implemented on multiple experimental cases ranging from 3D flow measurement within a micro-channel to imaging coherent flow structures in smooth- and rough-wall turbulent channel flows.

1.2 Thesis Outline

This dissertation consists of two major parts of: (1) background review and technique development (Chapters 2 and 3) and; (2) applications in a wide range flow experiments (Chapters 4 and 5). Specifically, an overview of the currently existing 3D PIV/PTV methods (including holographic PIV/PTV, scanning-PIV, defocusing PIV and tomographic-PIV) with the focus on their applications for 3D measurement of turbulent flows are presented in Chapter 2. In Chapter 3, we present our novel high-fidelity DIH-PTV algorithm to minimize the above mentioned limitations and challenges associated with implementation of DIH-PTV for 3D flow measurements. Chapter 4 provides the showcase of the implementation of the proposed method in a wide range of applications including microchannel flow, DNS turbulent channel flow, and experimental turbulent channel flow investigations through both near-wall and whole-field settings. Chapter 5 focuses on the application of the proposed DIH-PTV technique to investigate the effect of surface roughness on wall-bounded turbulent channel flows. Finally, the thesis concludes with Chapter 6 summarizing the main improvements, findings and the ongoing work for

further improving the capabilities of the technique for more accurate turbulent channel characterizations.

Chapter 2: Background: 3D Whole-field Flow Measurement

2.1 Introduction

Several different techniques have been developed and implemented for flow measurements, e.g. hot-wire anemometry (HWA) (Bruun1996), laser Doppler velocimetry (LDV) (Nezu and Rodi 1986) and particle image velocimetry (PIV) (Adrian 1991). Among all the techniques, optical-sensing based methods have received the most attention due to their non-intrusive nature. Within the optical sensing methods, PIV has gained the most popularity and became the most common measurement technique in the field of fluid mechanics (as is illustrated in Figure 2.1 by Westerweel *et al.* 2013). In this technique, the flow field is seeded with scattering particles and the flow velocity is measured imaging the tracer particle displacements. Specifically, PIV uses successively recorded images of tracer particles, which are illuminated with a light sheet, to quantify their local displacement through measuring the motion of a group of particles in small interrogation regions via auto/cross correlation. Similarly, the displacement could be measured by tracking individual tracer particles, which is categorized as particle tracking velocimetry (PTV). These whole-field measurement techniques (PIV and PTV) both provide the instantaneous spatial distribution of velocity through measuring the particle motions simultaneously at many points within the sampling region.

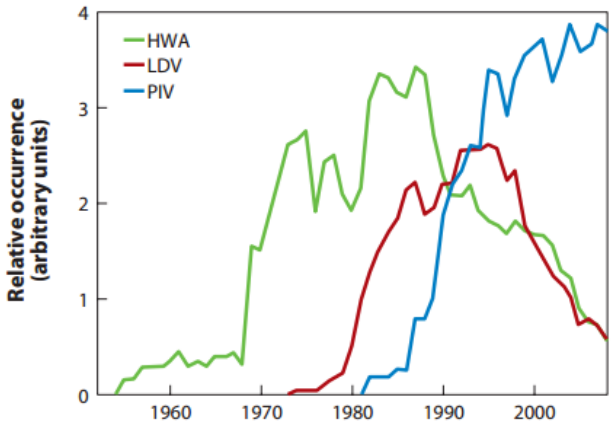

Figure 2.1: The occurrence of PIV versus HWA and LDV in Google Books (http://books.google.com) between 1952 and 2008 (Westerweel *et al.* 2013).

Since its development, PIV has been improved and implemented in a variety of applications to capture the flow physics in problems with more complex flows and geometries. For example, using in vivo imaging PIV was implemented to measure intra-cardiac flow forces in zebrafish embryos (Hove *et al.* 2003) or has been used for in-situ probing of the atmospheric boundary layer, through taking advantage of natural snowfall, within a field of view up to ~38×38 m^2 (Toloui *et al.* 2014 and Hong *et al.* 2014). In addition, several attempts has been made in order to extend the application of PIV and PTV to all three dimensions, mainly by employing the multi-view (tomographic PIV by Elsinga *et al.* 2006 and defocusing PIV by Willert and Gharib 1992), scanning (scanning PIV by Brücker 1992) or diffraction (Holographic PIV e.g. Meng *et al.* 2004) based imaging concepts. Despite all these efforts, turbulent flow measurement still imposes a significant challenges on implementation of particle image velocimetry (PIV) to resolve inherently 3D and unsteady turbulent structures and flows near solid boundaries due to the limited spatial or temporal resolutions. In addition to turbulent flow measurements, the 3D dimensionality of the flow phenomenon in microfluidic systems introduces challenges and limitations on application and validity of commonly used 2D micro-PIV (μPIV) in this field. Specifically, the out-of-plane motion of tracer particles across the volumetric illumination in μPIV often results in a considerable level of measurement noise and uncertainty. This motion in microfluidics is mainly attributed to Brownian motion (Olsen and Adrian 2000); or (2) 3D flows induced by the geometry of microfluidic devices such as micromixers and micropumps (Yoon and Kim 2006).

The aforementioned examples, from two major areas in experimental fluid mechanics (i.e. wall-bounded turbulence and microfluidics), highlight the constant need and importance of the development and implementation of 3D PIV/PTV measurement techniques, which is necessary to obtain a full understanding of the underlying flow physics. In the next section, we will provide an overview of the currently existing 3D PIV/PTV methods (including holographic PIV/PTV, scanning-PIV, defocusing PIV and tomographic-PIV) and some of their applications to 3D measurement of turbulent flows.

2.2 Review of Existing 3D Whole-field Technologies for Turbulent Flow

2.2.1 Scanning PIV:

Scanning approach for volumetric PIV measurements was first introduced in 1992 (Brücker 1992), where an oscillating mirror was employed to continuously sample the flow field at different in-depth planes. In brief, scanning PIV conducts planar or stereoscopic PIV on several in-depth planes that are illuminated in sequence through a scanning light-sheet mechanism. Specifically, particle images are acquired using a single camera (Planar PIV) or two cameras (Stereoscopic PIV) from a laser sheet that scans the sampling volume in depth direction (see Figure 2.2).

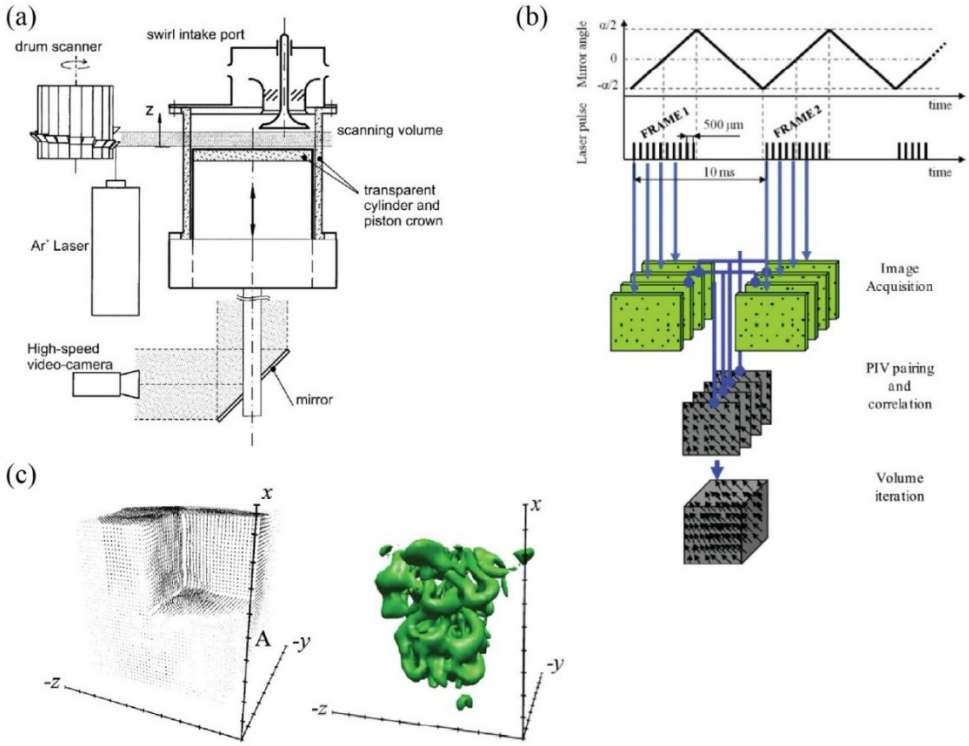

Figure 2.2: (a) A sketch of a scanning PIV optical set-up (Brucker 1997). (b) A schematic presentation of laser and scanning mirror timing diagram as well as the corresponding PIV calculation and stitching process to reconstruct volumetric velocity field in scanning PIV (Cheng *et al.* 2011). (c) A sample of instantaneous 3D velocity field and its corresponding iso-surfaces of vorticity at far-field of a turbulent jet measured by scanning PIV (Hori and Sakakibara 2004).

This technique has been used for 3D velocimetry in a variety of fields including in-vitro respiratory flows (e.g. Soodt *et al.* 2012), micro-fluidics using confocal microscopy (e.g. Lima *et al.* 2006), internal combustion (Brücker 1997), 3D velocimetry on a far-field

turbulent jet (Brucker *et al.* 2013 and Hori and Sakakibara 2004), and turbulent flow measurement within a mixing tank (Lawson and Dawson 2014). Here, we review some of the measurement aspects of the latter application of scanning PIV, which is the latest among other examples and more relevant to the scope of our study. Lawson and Dawson (2014) implemented stereoscopic scanning PIV to study the axisymmetric homogeneous turbulence generated within a large water tank. The sampling volume and velocity spatial are reported to be 125×23.5×123 mm^3 (streamwise × in-depth × spanwise), 6 mm. Similar to planar PIV, scanning PIV is capable of handling higher seeding densities compared to other 3D PIV/PTV techniques. Despite this advantage, scanning PIV suffers from limited temporal resolution, which is determined by the speed of the hardware involved in the scanning mechanism. This makes the technique not suitable for measuring highly 3D and unsteady fluid motions (e.g. wall-bounded turbulent flow applications). In other words, the flow speed and timescales must be quite slow in order to satisfy the "frozen flow" condition during scanning (Brücker *et al.* 2013 and Lawson and Dawson 2014). In addition, the spatial resolution of scanning PIV in longitudinal direction is lower compared to the lateral ones, which is caused by and related to the thickness of the light sheet. Figure 2.2 shows a schematic of a scanning PIV used in Brücker (1997), a schematic of an approach used for the 3D velocity field reconstruction from scanning PIV images by Cheng *et al.* (2011) and a sample of instantaneous 3D velocity field and the distribution of corresponding coherent structures from a far-field of a turbulent jet measurement using scanning PIV by Hori and Sakakibara (2004).

2.2.2 Defocusing PIV:

Defocusing PIV, introduced in 1992 (Willert and Gharib 1992), is a 3D PIV method that images particles from three different angles (three cameras or a camera with three apertures all on the same optical axis) and through pattern matching extracts the 3D location of particles (Figure 2.3a). This approach is fundamentally different from the triangulation methods used in stereo-vision photogrammetry (Pothos *et al*. 2009), i.e. each particle is represented by a triangle whose size is proportional to the depth location of the particle (Figure 2.3b). Then, the identified particles are tracked in 3D in order to calculate the 3D velocity fields.

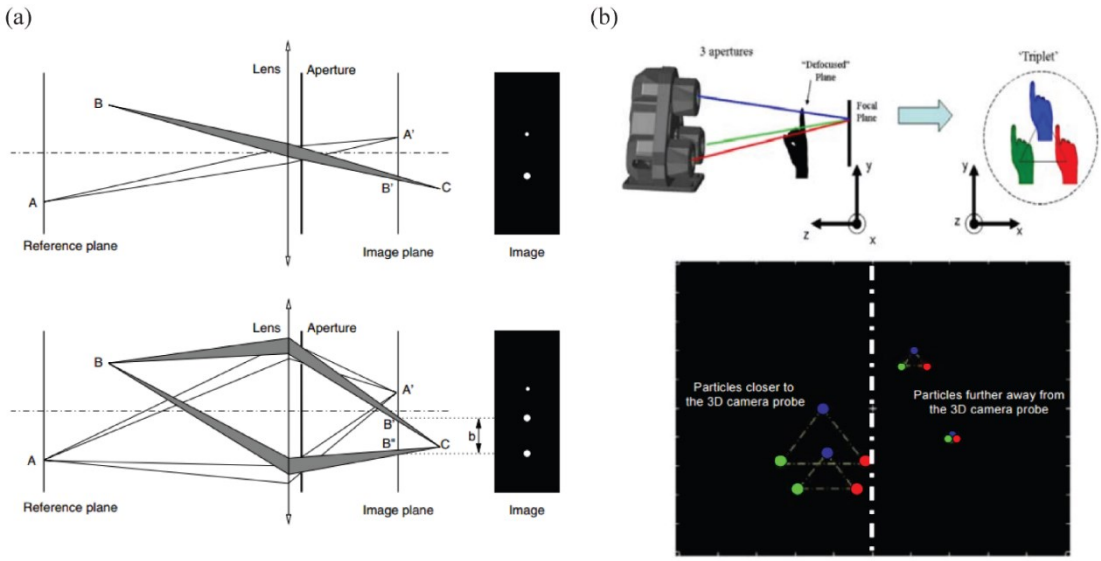

Figure 2.3: (a) The standard imaging (top) versus the defocusing imaging system (Pereira and Gharib 2004). (b) A schematic showing the concept of triplet (i.e. each particle creates a triangle in the image domain) in defocusing imaging using 3 cameras or one camera with 3 apertures (Pothos *et al.* 2009).

Defocusing PIV has been used for flow measurements in laboratory-scale and on a variety of subjects including bio-locomotive flows (e.g. Flammang *et al.* 2011 and Liu *et al.* 2013), 3D model wind turbine wake flows (Chamorro *et al.* 2013), cardiovascular flows (e.g. Le *et al.* 2013) and wall-bounded turbulent flows (e.g. Ortiz-Dueñas *et al.* 2011). In the case of wall-bounded turbulent flow measurements, Ortiz-Dueñas *et al.* (2011) investigated the effects of upstream cylindrical obstacles on the turbulent boundary layer within a 120 × 120 × 50 mm^3 sampling volume spanning 2.1 mm to 39.5 mm (52 y^+ to 1000 y^+) in wall-normal direction. The velocity spatial resolution of 3 mm was reported in all directions for this study. In a larger sampling volume (i.e. 120 ×140 × 60 mm^3), Chamorro *et al.* (2013) achieved 4 mm average velocity spatial resolution for a 3D flow measurement within the near wake region of a miniature 3-blade turbine model located within a turbulent boundary layer water channel. Recently, using index matching technique Toloui *et al.* (2015) studied rough-wall turbulent channel flow above cylindrical roughness elements within a sampling volume of 60×15×40 mm^3 sampled with 1 mm velocity spatial resolution (see Figure 2.4c).

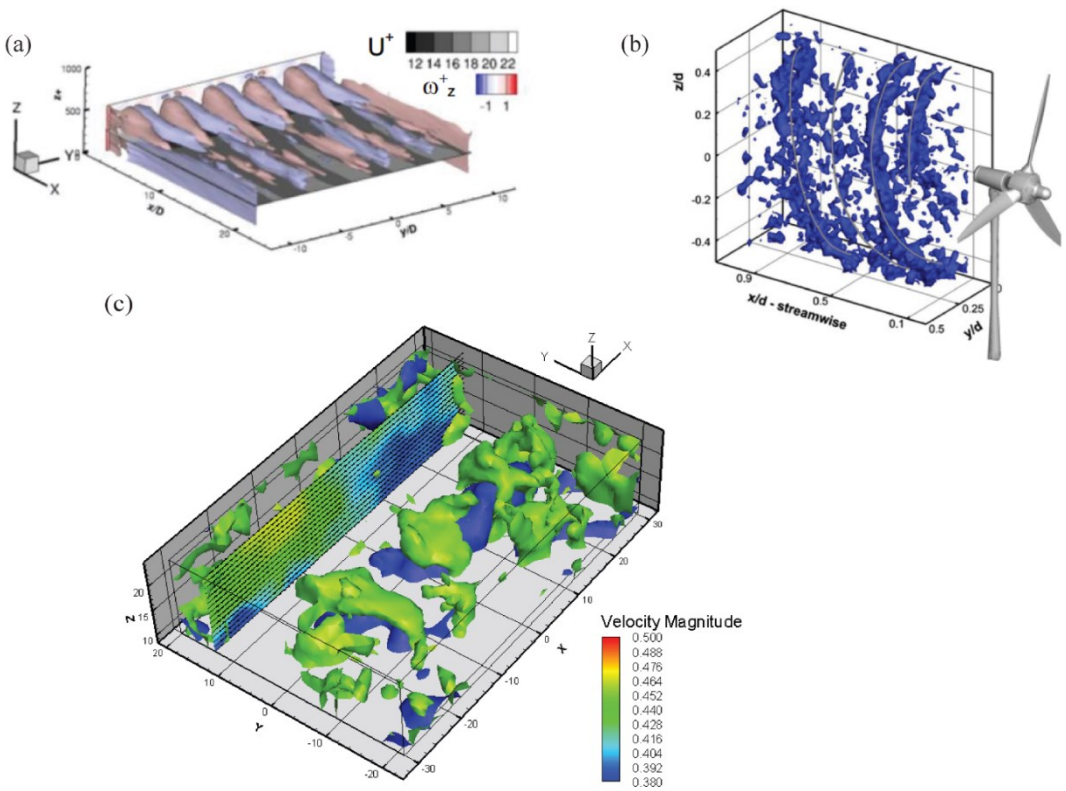

Figure 2.4: Some examples of defocusing PIV application in turbulent flow measurements: (a) a sample of instantaneous snapshot of iso-surfaces of wall-normal vorticity (blue and red) and stream-wise velocity contours (in grey-scale) from a water channel measurement (Ortiz-Dueñas *et al.* 2011); (b) a sample of instantaneous and dimensionless iso-vorticity magnitude contours behind a miniature wind turbine model within a water channel (Chamorro *et al.* 2013); and (c) a sample of 3D instantaneous velocity field from a rough-wall channel flow using defocusing PIV showing the interaction of low-speed streak (blue iso-surface) with looped vertical structure above it (iso-surfaces of vorticity magnitude, in green) from Toloui *et al.* (2015).

Overall, this technique requires a multi-view imaging system and the calibration process requires acquiring images of the calibration plate from all different angles and at several in-depth locations. The bounds of the sampling volume are restricted to the region scanned in calibration process (i.e. by moving the calibration plate in longitudinal intervals). This, consequently, makes near-wall flow measurement almost impossible within already constructed pipes or channels. In addition, in the case of flow measurements above roughness elements, the optical aberrations from slight mismatch of refractive indices between fluid and solid propagates through the entire reconstructed optical field, which contaminates the extracted particle field in the entire depth of measurements (similar to other multi-view PIVs).

2.2.3 Tomographic PIV:

Tomographic PIV or Tomo-PIV (introduced by Elsinga *et al.* 2006) is another multi-view 3D PIV technique where the 3D information of the flow field is captured on particle images recorded simultaneously at different viewing angles. The 3D particle fields at each time step of the acquisition are reconstructed from all corresponding particle images through an inverse mathematical algorithm. Notably, since the problem is underdetermined (i.e. a single set of projections can result from many different 3D objects), the tomographic reconstruction requires an iterative approach (e.g. multiplicative algebraic reconstruction technique called MART). Finally, the 3D cross-correlation is implemented on particle fields of successive tomographic recordings to calculate the 3D velocity fields within the volume of interest.

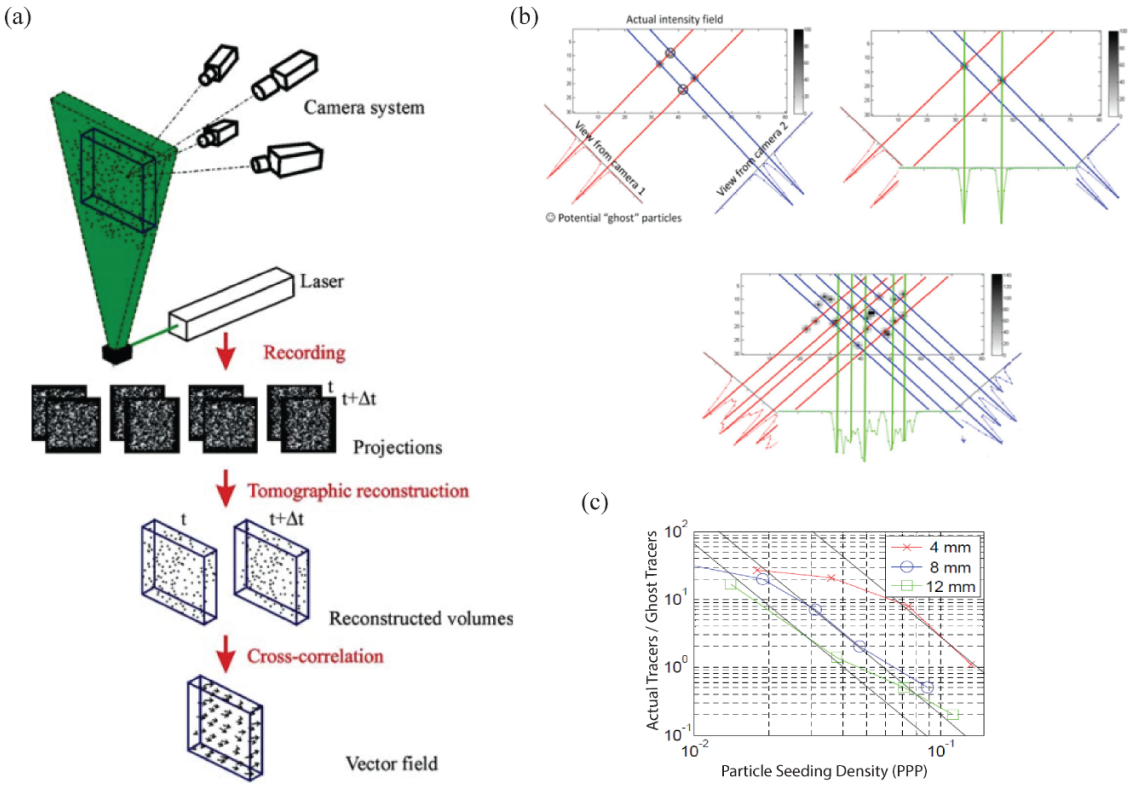

Figure 2.5: (a) Schematic of tomographic PIV working principle (Elsinga *et al.* 2006), (b) ghost particle formation in tomographic PIV caused by the intersection of lines of sight demanding higher number of viewing angles (i.e. more cameras) and limiting the seeding density (Scarano 2012) and (c) the inverse relation of number of actual tracer particles versus ghost particles in Tomographic PIV with particle image density and light sheet thickness (Elsinga 2008).

Figure 2.5a illustrates the working principle of Tomo-PIV. Tomographic PIV have been successfully implemented on many different research areas including turbulent boundary layer measurements (e.g. Schröder *et al.* 2011), flow characterization around swimming fish and organisms (e.g. Adhikari *et al.* 2015), cardiovascular flows (e.g. Buchmann *et al.* 2009) and etc. However, its volume reconstruction through an inverse approach demands expensive computations and causes generation of "ghost" particles, which increases its measurement uncertainty (see Figure 2.5b). In addition, as Figure 2.5c shows, the number of these ghost particles also increases with increasing the light sheet thickness (i.e. larger depth for sampling volume) or particle seeding density, since an increase in any of these two factors deteriorates the signal-to-noise ratio of the Tomo-PIV recordings (Elsinga 2008). Finally, due to its complicated set-up (e.g. requiring multiple axes of optical access), this technique has not been widely implemented for small-scale 3D flow measurements (i.e. microfluidics).

Figure 2.6 shows some results from different implementations of tomographic PIV in turbulent flow measurements within water channels. Schröder *et al.* (2011) employed tomographic PIV to study the evolution of coherent turbulent structures within the logarithmic region of a turbulent boundary layer (TBL) in a sampling volume of 63×15×68 mm^3. They achieved the velocity spatial resolution of 2.5 mm × 2.5 mm × 2.5 mm (streamwise, wall-normal and spanwise) corresponding to 55 y^+ × 55 y^+ × 55 y^+. In another study, Ghaemi and Scarano (2013) used tomographic PIV with an improved velocity resolution of 1.7 mm× 0.9 mm× 1.7 mm (43 y^+ × 22 y^+ × 43 y^+), to investigate the turbulent structures of high-amplitude pressure peaks within a TBL over a sampling volume of 16 × 6 × 24 mm^3. Recently, Zhang *et al.* (2015) used tomographic PIV in combination with Mach–Zehnder interferometry (MZI) to simultaneously measure 3D velocity fields as well as the wall deformations. To the best of our knowledge, this work reported the best velocity resolution for implementation of tomographic PIV for turbulent channel flow measurements (i.e. 0.69 mm equal to 63 y^+ in all directions) within a sampling volume of 30 × 10 × 10 mm^3 corresponding to 2778 y^+ × 926 y^+ × 929 y^+.

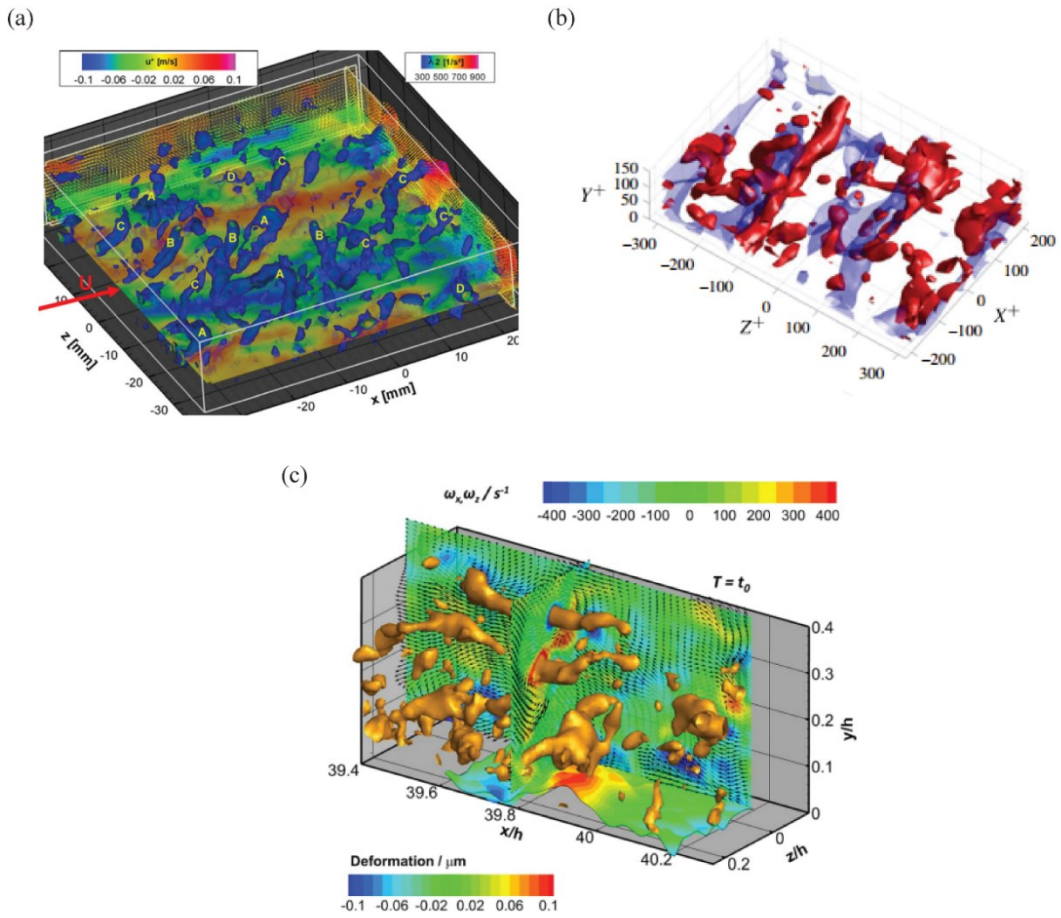

Figure 2.6: Some selected results from different implementations of Tomo-PIV for wall-bounded turbulent flow measurements: (a) an instantaneous 3D velocity volume superimposed by flow structures (iso-surfaces of λ_2 in blue) by Schröder *et al.* (2011), (b) an unsteady organization of the low-speed streaks (blue) and the vortical structures (red) visualized within a TBL (Ghaemi and Scarano 2013) and (c) a sample of instantaneous 3D flow velocity and a 2D distributions of the wall deformation, iso-surfaces of λ_2 are plotted in yellow and the color contours are spanwise and streamwise vorticities (Zhang *et al.* 2015).

2.2.4 Holographic PIV and PTV:

Holography is a single camera 3D imaging method that is capable of capturing 3D information in a single acquisition. The 3D information of imaged objects are encoded on their corresponding diffraction fringe patterns forming a holographic image (hologram) on a digital or film sensor. Specifically, these fringe patterns are formed from the interference of the light scattered from each object (object wave) with the reference light beam illuminating the sampling volume. Then, the 3D distribution of the object wave, containing

the 3D shape and position information of the objects, could be optically or computationally reconstructed from the 2D recorded image (hologram).

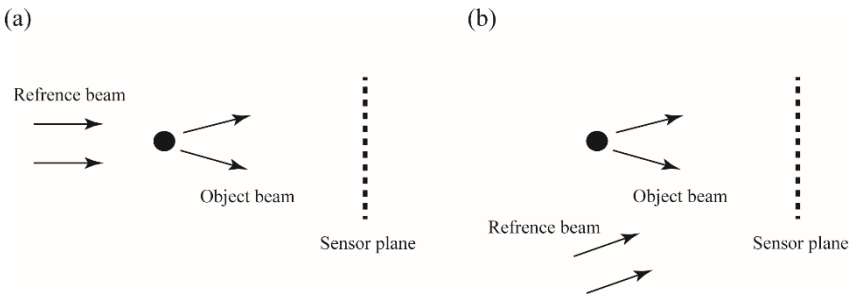

Figure 2.7 Holographic recording configurations: (a) in-line and (b) off-axis.

Holographic recording methods are generally categorized, based on the angle between the incident light beam and the scattered light wave front, into two major configurations: (1) in-line and (2) off-axis (Figure 2.7). Using a tilted plane reference wave instead of a uniform plane wave results in a clear spatial separation of real and virtual image in off-axis recording, which generates fringe recordings with higher signal-to-noise ratio compared to those of inline recording. This allows higher number of detectable objects/particles in off-axis recordings. Despite this advantage, the off-axis set-up suffers from complexity of optical set-up and strict requirements for laser energy and coherence level. In addition to low cost optical components, inline holography benefits from an easy image calibration, simpler and more stable optical set-ups (highlighting its unique potential for usage in miniaturized optical sensing applications), and can provide optical sensing to regions with limited optical access (due to its single axis imaging set-up).

In Holographic PIV/PTV the objects are tracer particles, and 3D instantaneous velocity fields are calculated through conducting volumetric cross-correlation or 3D tracking on consecutive reconstructed particle fields (reconstructed from corresponding holographic recordings). In brief, as Figure 2.8 shows, holographic PIV/PTV technique mainly includes 3 steps of: (1) recording; (2) 3D particle extraction; and (3) 3D particle tracking or volumetric cross-correlation. A detailed mathematical framework and description of holographic recording and reconstruction will be presented in the next chapter.

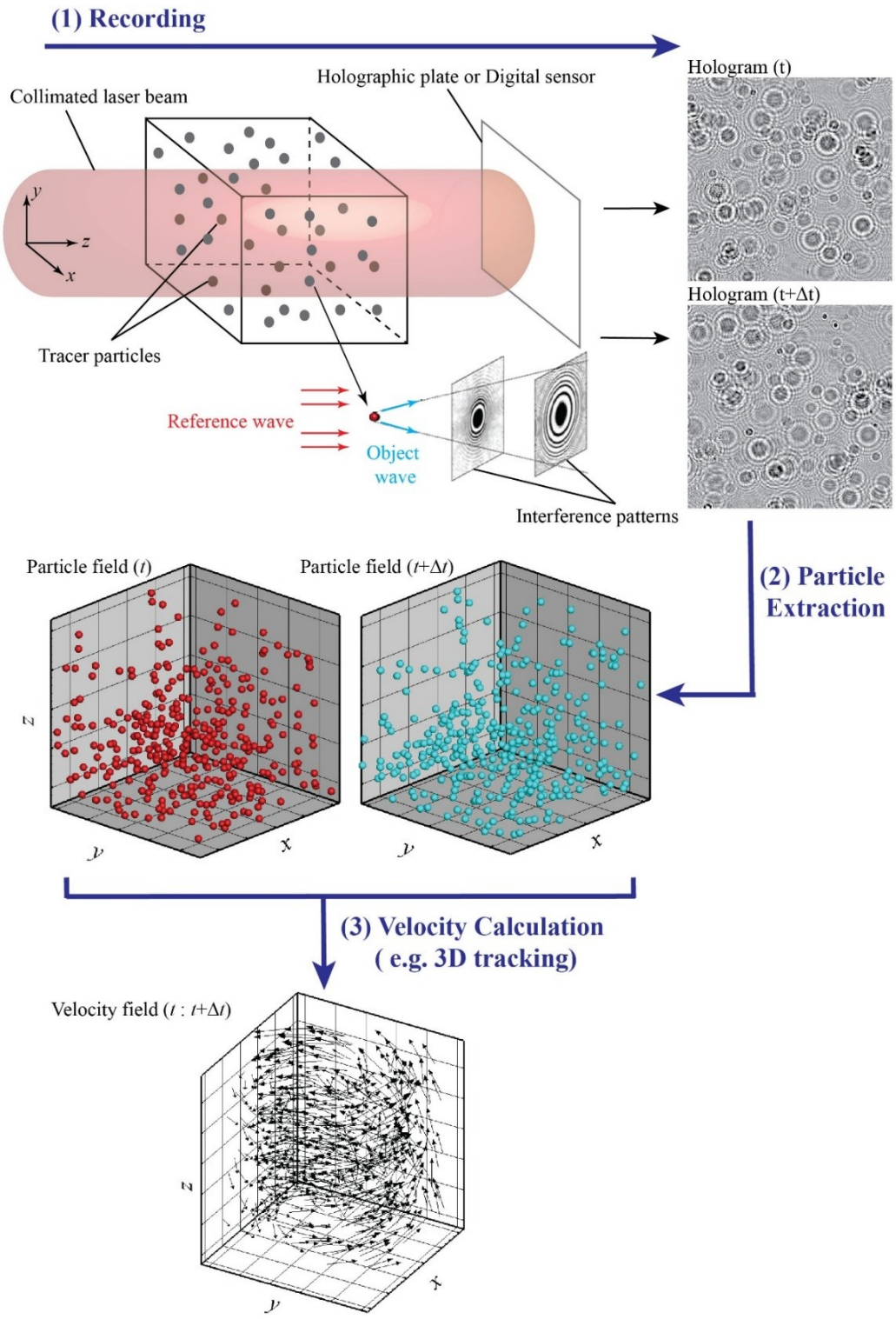

Figure 2.8: Principle of HPIV and HPTV.

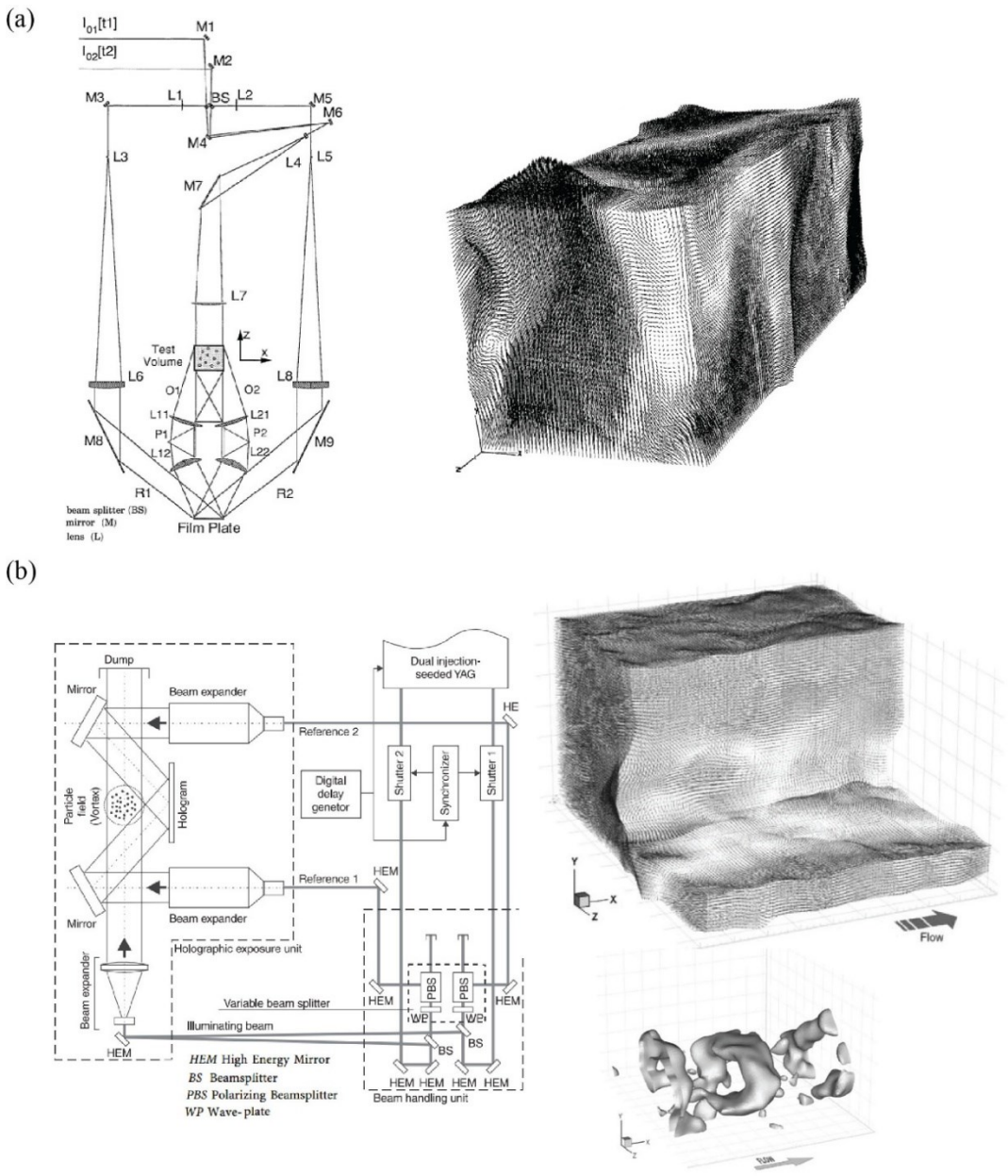

Figure 2.9: (a) Left: an off-axis holographic optical system used by Barnhart *et al.* (1994) and right: a sample of their 3D velocity field measurements from a pipe flow. (b) Left: an off-axis holographic optical system developed by Pu and Meng (2000) and right: a sample of their 3D velocity field and vorticity iso-surface measurements behind a mixing tab.

Off-axis holographic recording using film plate holograms have been used in different off-axis configurations in holographic PIV (HPIV) measurements. For example, Barnhart *et al.* (1994) employed phase conjugate holographic set-up (Figure 2.9a) to measure 3D velocity fields within a turbulent pipe flow. They performed HPIV through an in-situ

reconstruction over a sampling volume of 24.5 × 24.5 × 60 mm^3 and obtained more than 400000 vectors (i.e. < 450 μm velocity spatial resolution). In another study, Pu and Meng (2000) developed an off-axis HPIV set-up using a dual reference beam to capture the 90 degrees scattering of tracer particles (see Figure 2.9b). This system was used to characterize the 3D wake of a surface mounted in a water channel through utilizing an in-situ reconstruction, and achieved ~80000 vectors within a sampling volume of 44 × 56 × 32 mm^3, which corresponds to less than 1 mm velocity spatial resolution. Despite these decent values of velocimetry resolution and sampling volume size that were achieved using film-based off-axis HPIV, the cumbersome optical set-up alignment and reconstruction process have hindered this technique from being widely implemented for flow measurements. In addition, the use of plates or films greatly limits the ability to study dynamic phenomena (Katz and Sheng 2010).

Therefore, holographic PIV/PTV has switched to digital recording and in-line configuration for 3D flow measurements since beginning of 2000 (e.g. Meng *et al.* 2004 and Hinsch 2002) due to its simplicity of the optical set-up and reconstruction procedure. The digital recording eliminates the chemical processing required for film-based holography as well as cumbersome optical reconstruction, which are replaced with digital camera recording and numerical reconstruction, respectively. In addition, digital holographic imaging does not require the use of off-axis recording schemes, since the advantages of using off-axis recording (e.g. the spectrally separated image waves and the multiplexing capability) are no longer needed in digital recording (Meng *et al.* 2004). Hence, digital holography has been mainly focused on the in-line configuration for recording, which benefits from simple and low cost optical set-up (a single camera 3D imaging system with low laser power requirement due recording the *forward-scattering*) with an easy image calibration. These advantages make digital inline holography (DIH) one of the best solutions for 3D imaging in a wide range of applications over a variety of research fields including microbiology (e.g. Burns *et al.* 2007 and Hong *et al.* 2012), low cost bio-sensing device development (e.g. Seo *et al.* 2009 and Im *et al.* 2015), methodology (e.g. Kaikkonen *et al.* 2014 and Beals *et al.* 2015), field chemical and biological monitoring (e.g. Graham *et al.* 2010 and Sullivan *et al.* 2011), 3D micro PIV (e.g. Toloui and Hong 2015 and Singh and Panigrahi 2015) and etc.

However, the effective hologram aperture is much smaller in digital HPIV than that of film-based HPIV (Meng *et al.* 2004), which results in at least an order of magnitude lower resolution for digitally recorded holograms compared to film-based recordings (Katz and Sheng 2010). Moreover, in an inline recording a 2D hologram records the interference fringe patterns of all the objects contained in the laser path. Therefore, as tracer concentration increases, the noise generated from the cross-interference among adjacent particles and the particles that are outside of the measurement region but within the light path increases. This significantly increases speckle noise (i.e. lowers the signal-to-noise ratio (SNR)) in holographic recordings, which reduces the number of extractable particles. Therefore, despite its advantages, this issue limits DIH-PIV/PTV measurements to lower seeding densities (i.e. poor velocity spatial resolution) and smaller sampling volumes in comparison with other 3D whole-field flow measurement techniques. In order to tackle this issue, several different creative methods have been developed and implemented for DIH turbulent flow measurements. Below, we will briefly introduce and review some of these methods.

(1) ***90^o scattering***: In an attempt to enable DIH-PIV/PTV for flow measurements within a larger sampling volume with high seeding density of tracer particles (i.e. comparable to other 3D tracer based methods), Cao *et al.* (2008) introduced a hybrid system (Figure 2.10a) with an off-axis in-line recording system (< 1^o off-axis recording angle). This method benefits from the speckle noise suppression feature of off-axis (side) scattering as well as the lower resolution requirement of on-axis (in-line) recording. They used this technique to study particle clustering in a large cubic box of an isotropic turbulence, where more than 1000 particles are extracted from a measurement volume of 8 × 6 × 5 mm^3 (i.e. an average of ~ 620 μm particle spacing). The flexibility on controlling the location, size and boundaries of the sampling volume (through controlling the size and location of the illumination beam) is the biggest advantage of this technique. However, this comes with the price of significantly weaker scattering efficiency at 90◦ compared to the forward scattering as well as requirement for a laser source with a longer coherence length compared to those used for conventional in-line recordings.

(2) ***Probe-based DIH***: Allano *et al.* (2013) designed and developed an illumination probe using fiber optics to guide the laser beam to the desired region and restrict the

scattering particles to those located within the region of interest. Specifically, as Figure 2.10b shows, a fiber coupled laser diode inserted into a wind tunnel (entirely seeded with fog droplets) through a metallic needle in order to restrict the sampling volume to smaller volume within the near-wall region. The presence of the laser probe and its holder within the wind tunnel produces flow disturbances, which makes this method an intrusive flow diagnostic.

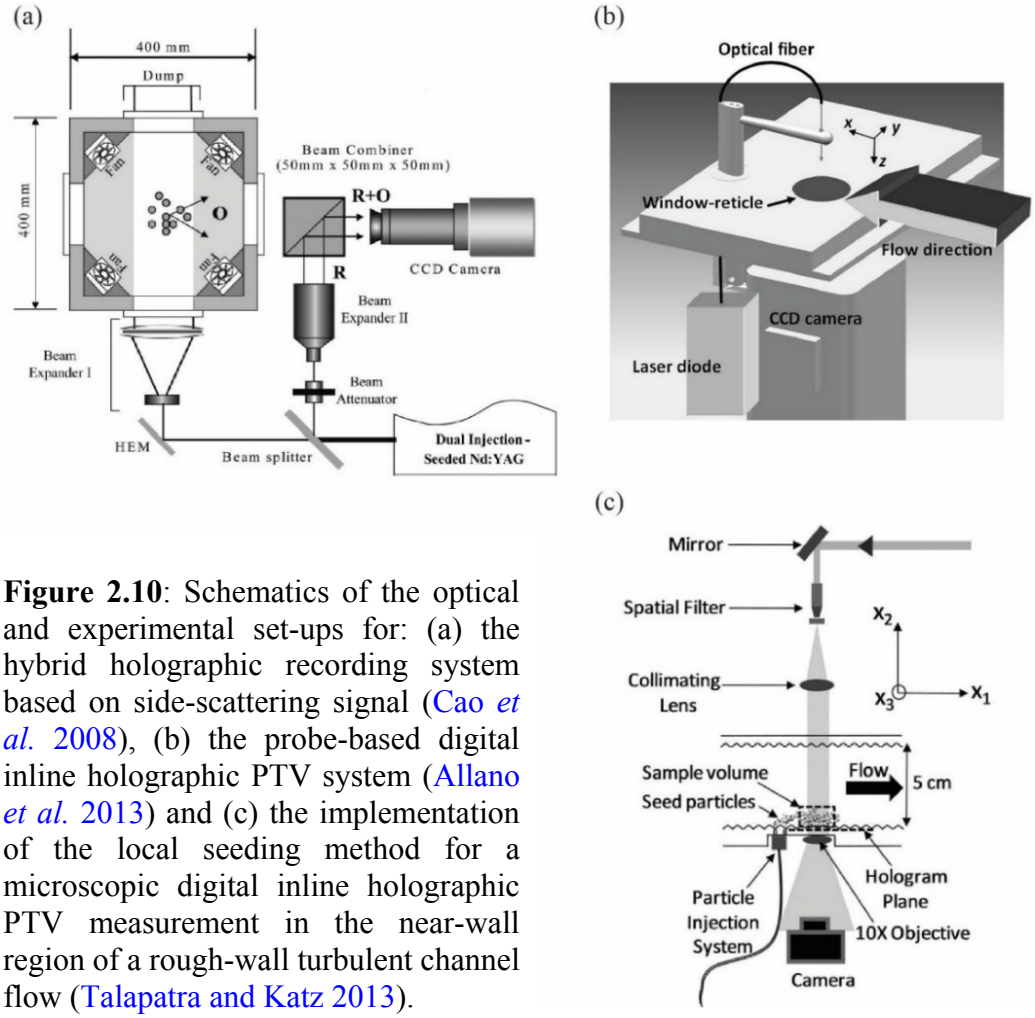

Figure 2.10: Schematics of the optical and experimental set-ups for: (a) the hybrid holographic recording system based on side-scattering signal (Cao *et al.* 2008), (b) the probe-based digital inline holographic PTV system (Allano *et al.* 2013) and (c) the implementation of the local seeding method for a microscopic digital inline holographic PTV measurement in the near-wall region of a rough-wall turbulent channel flow (Talapatra and Katz 2013).

(3) ***Local seeding***: In combination with the use of microscopic inline holography, Sheng *et al.* (2008) introduced a simple but an effective mechanism that benefits from restricting the sampling volume to the near-wall region without inserting any probe or measurement device into the flow facility. This enables DIH flow measurements over the near-wall region of the turbulent channel flow with significantly high seeding density of

tracers. Specifically, a 10X microscopic objective is employed to improve the depth of focus while the local seeding mechanism limits the scattering volume to the near-wall region with a minimal level of flow disturbance (Figure 2.10c). In this method, the flow is locally seeded through a set of five small holes (50 μm in diameter) drilled to the bottom wall of the channel (57×57 mm^2 square duct facility), which are located immediately upstream of the sampling volume. This minimizes the deterioration of the reference beam caused by the particles cross-interference along the depth of the flow channel. In order to minimize the flow disturbance caused by the local seeding, particle solution injection rate (using a syringe pump) and its location are set to 1% of the channel mean velocity and 800 injector diameter (upstream of the sampling volume), respectively. Sheng *et al.* (2008) achieved a velocity spatial resolution of 51 μm × 136 μm × 17 μm (3 y^+ × 8 y^+ × 1 y^+) in streamwise, wall-normal and spanwise directions in a smooth-wall channel flow within a sampling volume of 1.5 × 2.5 × 1.5 mm^3 starting at ~ 3.5 μm (0.2 y^+) from the wall (see Figure 2.11a). Recently, based on refractive-index-matching (RIM) technique, Talapatra and Katz (2013) has employed a similar method (i.e. local seeding for DIH-PTV) to examine the turbulent flow structures within and above the roughness sublayer over a rough-wall composed of acrylic pyramidal roughness elements (Figure 2.11b). As Figure 2.11c shows, their results for mean flow velocity and Reynolds stresses match to those of a two-dimensional PIV measurement conducted with the same experimental condition and over the same rough-surface (Hong *et al.* 2012). Overall, although, this method provides comparatively unmatchable spatial resolution and wall proximity, it is currently restricted to much smaller measurement volume compared with other 3D whole-field methods. In addition, the local seeding approach suffers from time-varying tracer particle concentration in the sampling volume, which consequently results in time-varying velocimetry resolution of DIH-PTV.

Notably, unlike all other previously reviewed methods, holographic PIV/PTV is not a multi-view or a scanning technique, but a single camera 3D imaging technique. In the next section, we will explain the principles and mathematical frame work of DIH imaging for both recording and reconstruction phases as well as our approach to tackle the issues associated with this technique.

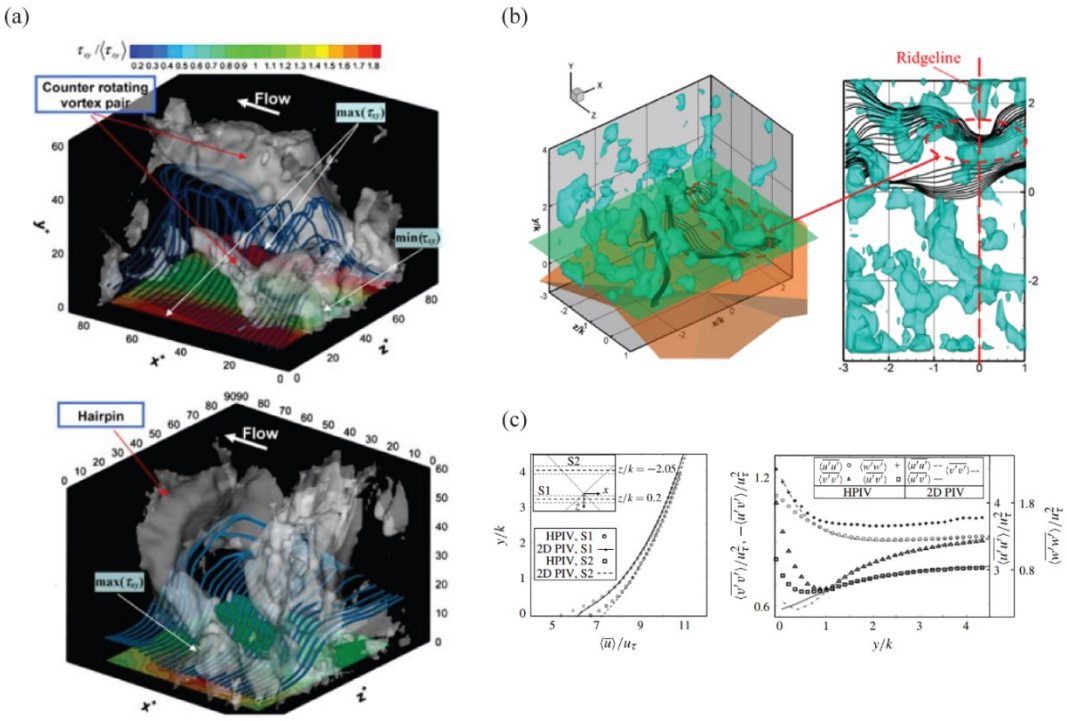

Figure 2.11: (a) Samples of instantaneous distribution of λ_2 iso-surfaces, wall shear stress and vortex lines in smooth-wall channel flow measured by DIH-PTV using local seeding mechanism (Sheng *et al.* 2008), and (b) an instantaneous iso-surface of λ_2 and sample vortex lines depicting a strong ejection event in near-rough-wall region of turbulent channel flow measured by DIH-PTV using local seeding mechanism (Talapatra and Katz 2013).

Chapter 3: High Fidelity Digital Inline Holographic PTV Method for Flow Measurements

Overview

Among all the 3D optical flow diagnostic techniques, digital inline holographic particle tracking velocimetry (DIH-PTV) provides the highest spatial resolution with low cost, simple and compact optical setups. Despite these advantages, DIH-PTV suffers from major limitations including poor longitudinal resolution, human intervention (i.e. requirement for manually determined tuning parameters during tracer field reconstruction and extraction), limited tracer concentration, limited sampling volume size and expensive computations. These limitations prevent this technique from being widely used for high resolution 3D flow measurements. In this study, we present our novel high-fidelity DIH-PTV algorithm with the goal of overcoming all the above mentioned limitations. Specifically, the proposed particle extraction method (Toloui and Hong 2015) consists of multiple steps involving 3D deconvolution, automatic signal-to-noise ratio enhancement and thresholding, and inverse iterative particle extraction. In addition, a multi-pass 3D tracking method along with a cross-correlation based longitudinal displacement refinement scheme are developed for the 3D displacement calculation, which reduces the longitudinal displacement uncertainty to below ~ a fraction of the tracer particle size. The entire method is implemented using GPU-based algorithm to increase the computational speed significantly. Validated with synthetic particle holograms, the proposed method can achieve particle extraction rate above 95% with ghost particles less than 3% for holograms with particle concentration above 3000 particles/mm^3. Such improvements will substantially enhance the implementation of DIH-PTV for 3D flow measurements and enable the potential commercialization of this technique.

3.1 Introduction

Particle Image Velocimetry (PIV) is a well-established technique for whole-field velocity measurements, arguably the most popular optical technique currently in use. However, implementing PIV for measuring flows in three dimensions (3D) is inherently a very challenging task. The widely used 3D PIV techniques, including scanning PIV (Hori and

Sakakibara 2004), defocusing PIV (Willert and Gharib 1992), tomographic PIV (Elsinga *et al.* 2006) and digital in-line holographic (DIH) PIV and PTV (e.g. Pan and Meng 2001 and Katz and Sheng 2010, referred to as DIH-PIV and DIH-PTV hereafter) are still limited in their ability to resolve detailed turbulent structures and flows near solid boundaries due to the stringent requirements on spatial and temporal resolution.

In brief, temporal resolution of scanning PIV is constrained by the hardware speed involved in the scanning mechanism, and is inherently not suitable for measuring highly 3D and unsteady fluid motions. Both V3V and tomographic PIV are multi-camera-based imaging techniques which require expensive hardware and volumetric calibration, i.e., all cameras record the images of the calibration target spanning the volume of interest. In the case of tomographic PIV, volume reconstruction through an inverse approach based on the intersection of lines of sight demands expensive computations and causes generation of "ghost" particles increasing its measurement uncertainty. On the other hand, DIH imaging benefits from a simple and low cost optical set-up with an easy image calibration and synchronized data acquisition. Specifically, the DIH set-up (see Figure 3.1) only includes one single camera, collimating optics and a low-power laser source (owing to recording of *forward-scattering*, e.g. less than ~0.1% the power compared to other 3D PIV methods for particles ≥ 2 µm, see Figure 3.2). In addition, compared with the other aforementioned 3D whole-field techniques, DIH-PTV provides unmatchable spatial and temporal resolution in quantifying 3D turbulent flow near solid surfaces, where the relevant scales range from µm to sub-mm. For example, 85 µm × 42.5 µm × 85 µm (i.e. 5×2×5 wall units) in the streamwise, wall-normal and spanwise directions, respectively, and within the measurement volume of $1.5 \times 2.5 \times 1.5$ mm^3 (Sheng *et al.* 2008) and 60 µm in all directions reported by Talapatra and Katz (2013). Comparatively, the highest spatial resolution achieved for Tomographic PIV, to the best of our knowledge, is 0.69 mm (equal to 63 wall units) within $26 \times 12 \times 11.5$ mm^3 (Zhang *et al.* 2015), and 1 mm in a volume of $50 \times 25 \times 50$ mm^3 for defocusing PIV (Toloui *et al.* 2015). The temporal resolution of DIH-PIV is inherently limited by acquisition rate of the imaging camera. With a high-speed camera and continuous laser source, the 3D time-resolved turbulent flows can be measured using DIH-PIV under many flow settings.

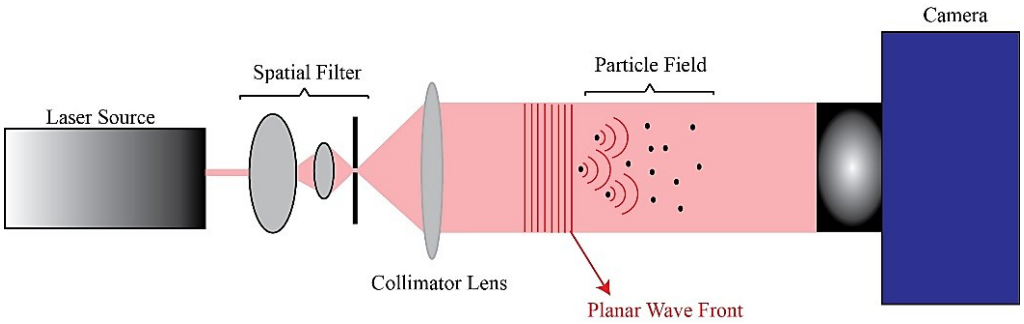

Figure 3.1: The optical setup of digital in-line holography.

Despite all these advantages, the implementation and development of DIH-PTV for 3D flow measurement is severely hindered by a number of challenges and limitations, described below:

1- **Poor longitudinal resolution**: Due to extended depth-of-focus (DOF), DIH yields significantly lower longitudinal resolution than that in the lateral direction. This limitation results from the substantial elongation of the reconstructed tracers in the depth direction. According to Katz and Sheng (2010), a spherical particle of size 20-μm generates an elongated ellipsoidal of ~ 1 mm long under green laser illumination. This limitation causes large uncertainty in the measurement of the longitudinal velocity component.

2- **Human intervention**: The extraction of 3D tracer information from a hologram requires sophisticated image processing, which involves a number of tuning parameters. Many of these parameters (e.g., gray-scale threshold) need to be manually provided by the user at different steps of the processing, based on the image quality, tracer properties, and flow conditions, etc. Hence, the optimal selection of these parameters requires several iterations, and is highly dependent on the user's judgment and experience.

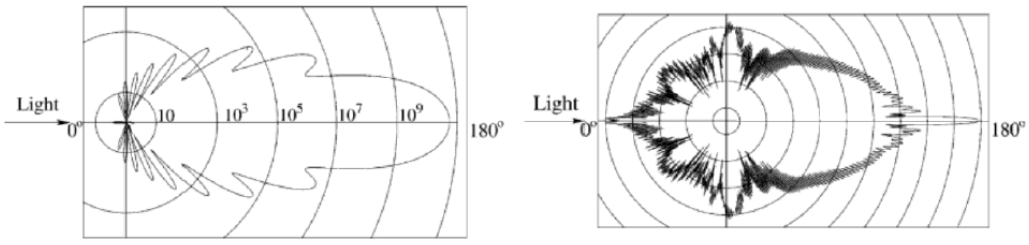

Figure 3.2: Particle scattering in water: (left) 1 μm and (right) 10 μm glass particles (Raffel *et al.* 1999).

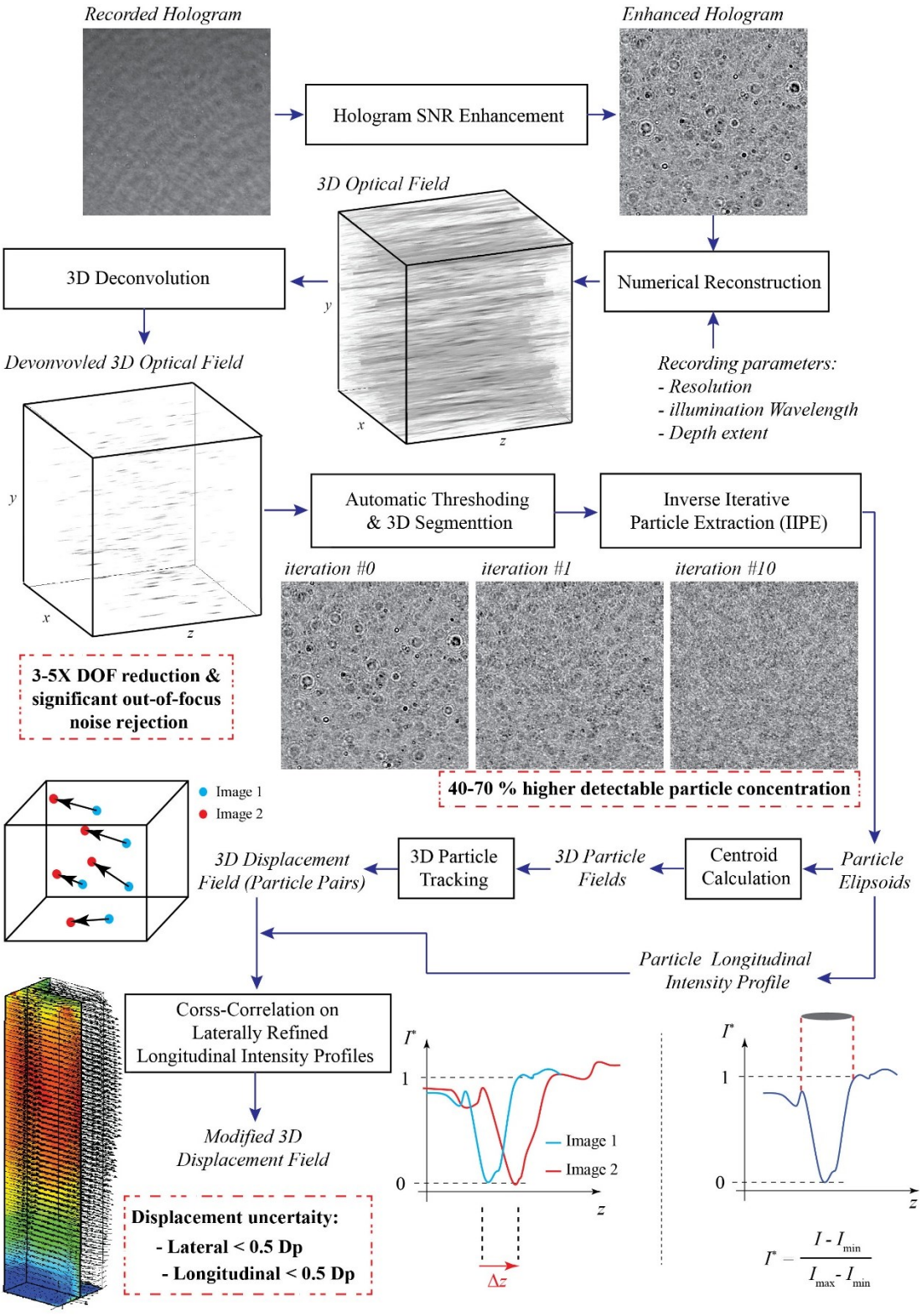

Figure 3.3: The flow chart of the DIH-PTV algorithm for 3D flow measurements.

3- **Limited Tracer Concentration**: In DIH, the 2D hologram records the interference fringe patterns of all the objects contained in the laser path. As tracer concentration increases, the noises generated from the cross-interference among adjacent particles and the particles that are outside of the measurement region but within the light path increase, which significantly lowers the signal-to-noise ratio (SNR) of holograms. Therefore, DIH-PTV generally operates with low tracer concentration, which limits the spatial resolution of the velocity field.

4- **Expensive computation**: DIH-PTV involves a number of complex numerical processing steps. In particular, 3D holographic reconstruction and particle image segmentation involve processing a large volume of 3D data (e.g., reconstructing a 1 MB hologram typically produces a ~1 GB 3D dataset). These computational steps are limited by the throughput and memory bandwidth capabilities of modern processors.

A standard DIH-PTV method includes 3 major steps: holographic recording, 3D particle extraction from the recorded holograms, and particle tracking to generate a velocity vector field. In the current study, we introduce a series of novel holographic particle extraction and tracking methods (illustrated in Figure 3.3) that overcome the above mentioned challenges and makes DIH-PTV a mature technique for 3D flow measurements. The chapter is structured as follows. Sec. 3.2 provides a detailed description of each step of our particle extraction method and concludes with a synthetic holographic study highlighting its effectiveness and efficiency. In Sec. 3.3, we present our 3D velocity field calculation method including the multi-pass 3D tracking and cross-correlation based displacement methods. The chapter concludes with a summary and discussion in Sec. 3.4.

3.2 Particle Extraction

For DIH-PTV implementation, the most critical and the most challenging step is the extraction of 3D locations of tracer particles from recorded holograms. In this section, we first present an overview of currently existing particle extraction methods and discuss their both advantages and drawbacks. Then, we introduce our methodology to improve the step of particle extraction.

Different methods have been used to extract information of 3D particles including their size and position from digitally recorded holograms, which can be categorized into the following main methods.

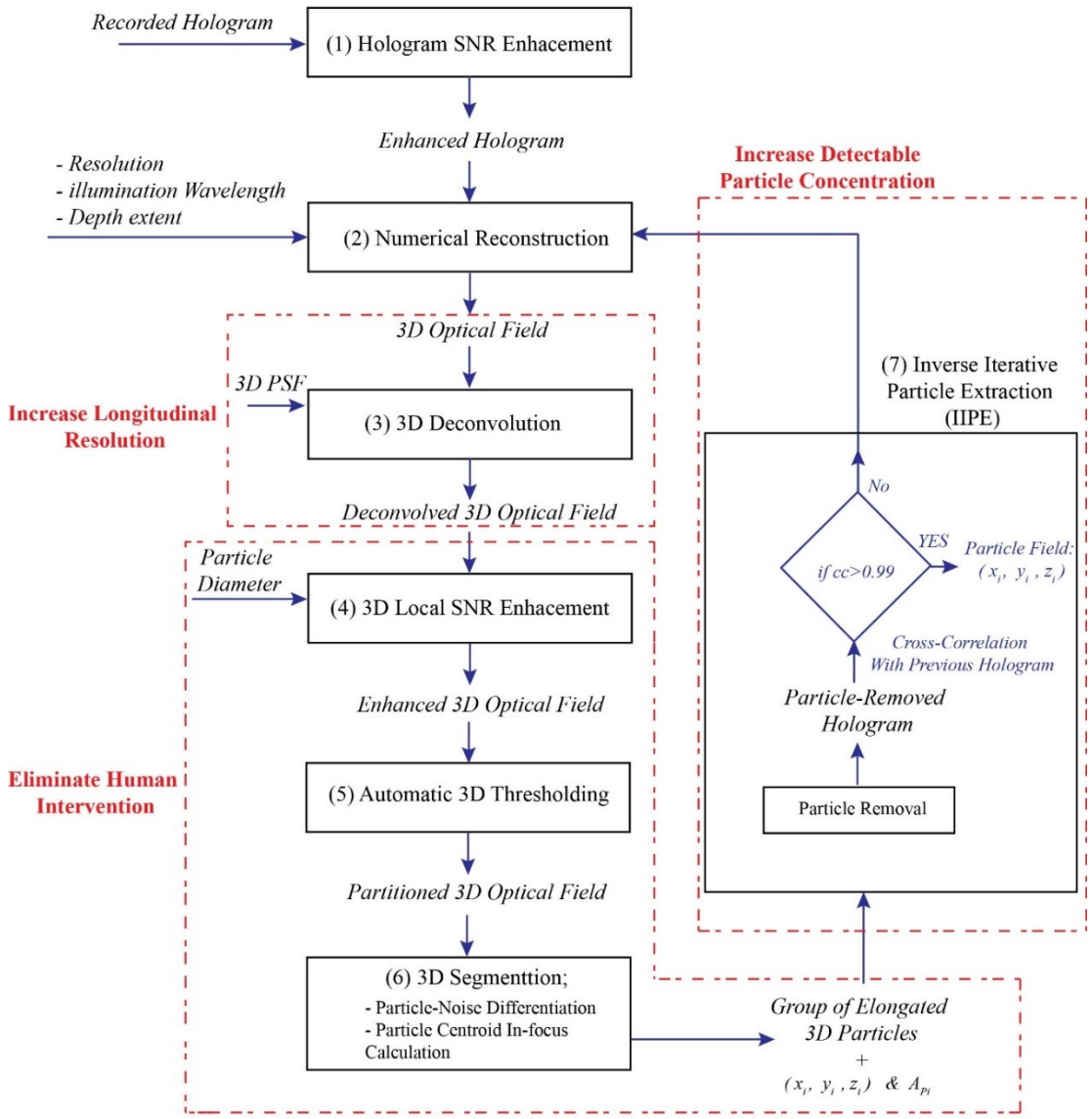

Figure 3.4: The flow chart of our DIH-PTV particle extraction procedure.

(a) *Focus metric based on 2D projection* (e.g. Tian *et al.* 2010 and Guildenbecher *et al.* 2012): The 2D minimum intensity map of reconstructed 3D image is used to detect objects and determine their lateral positions, and in-depth location of the objects are determined by different focus metrics such as the intensity distribution, the sharpness, etc. This approach uses 2D image for object segmentation, which significantly improves the

computational speed and lowers the memory requirements of DIH-PTV. However, using 2D projection for particle detection is susceptible to the noise generated by the cross-interference of laterally-adjacent particles, which can produce a large number of fake particles as the particle concentration increases. In addition, the longitudinal resolution of this approach relies on accurate detection of particle edges. Large uncertainty can be generated when applying this approach to smaller objects such as flow tracers of typically around 2-3 pixel in diameter. For the techniques that employ minimum intensity as a focus metric (e.g. Tian *et al.* 2010), a user defined intensity threshold is used to detect and segment objects, which is subjected to changes under different hologram recording conditions.

(b) *Inverse simulation and residual calculation* (e.g. Soulez *et al.* 2007). The inverse approach first generates a modeled hologram based on diffraction theorem using prescribed parameters (e.g. 3D location and object size, etc.). Then, through an iterative process, these parameters are being gradually refined to minimize the difference between the modeled hologram and the recorded one. The refined parameter at the end provides an estimate of object location and size. Although the inverse approach can provide subpixel resolution in the longitudinal direction, it is susceptible to the noises from the background and the cross-interference of objects, which is not suitable for applications with dense tracer holograms. In addition, the iterative modeling of holograms by scanning through several in-depth positions and calculation of residual hologram leads to a highly expensive set of computations.

(c) *3D segmentation* (e.g. sheng *et al.* 2008, Talaptra and Katz 2013 and Meng *et al.* 2004): It uses reconstructed 3D optical fields to simultaneously detect objects and calculate their 3D locations. In this approach, each cross section of reconstructed 3D optical fields is first segmented based on user defined intensity threshold. Then, the 2D segments of each object in adjacent cross sections are joined together to form 3D elongated objects, and the 3D centroid location of each object is determined using geometric average or intensity-weighted average of the location of each voxel within the object. Compared with focus metric based on 2D projection, this approach can work with higher concentration for small tracer particles, and it reduces the uncertainty on particle detection significantly. However, this approach still suffers from poor longitudinal resolution associated with depth-of-focus

(DOF) (Katz and Sheng 2010) issue, and requires substantial human intervention to optimize the intensity threshold for segmentation. It is also computationally expensive compared with the focus metric approach.

In summary, none of these existing methods can provide high-fidelity and efficient particle extraction for the DIH-PIV implementation. In this chapter, we introduce a new method with the intention to overcome the main challenges mentioned above. As illustrated in Figure 3.4, the proposed method for particle extraction consists of seven major steps including: (1) hologram enhancement; (2) numerical reconstruction; (3) 3D deconvolution; (4) 3D local SNR enhancement; (5) automatic thresholding; (6) 3D segmentation; and (7) inverse iterative particle extraction (IIPE).

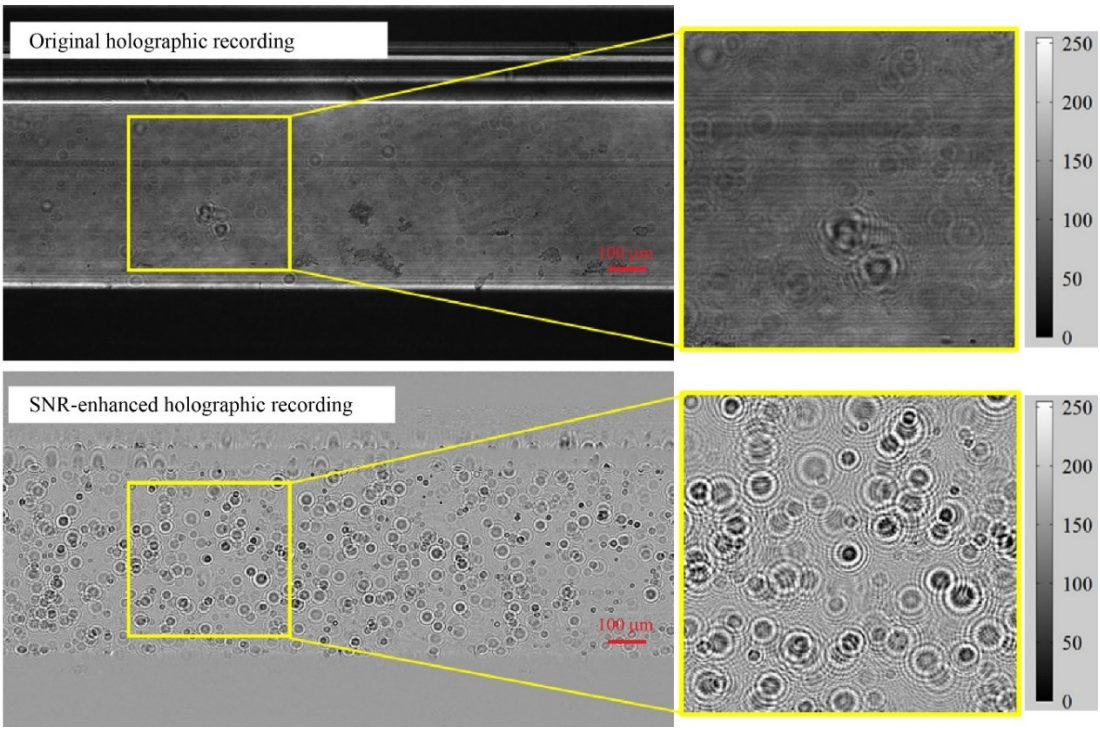

Figure 3.5: A sample hologram from a water flow within a micro-channel (seeded with $D_p = 2$ μm tracer particles up to 1500/mm^3 concentration) before (top) and after (bottom) our hologram SNR-enhancement implementation.

Specifically, the hologram enhancement is conducted through subtraction of holograms from corresponding time-averaged hologram followed by gray-scale equalization. As Figure 3.5 shows, for a sample of holographic recording from a water flow within a 1×1 mm^2 cross-section microchannel seeded with 2 μm silver coated silica particles, the

implementation of our hologram enhancement algorithm improves the fringe pattern SNR significantly. In addition, to increase the longitudinal resolution of DIH, we enriched our holographic processing algorithms with a 3D deconvolution technique (Step No.3). To minimize human intervention and enable automatic particle extraction, we develop an automatic 3D local SNR enhancement and thresholding algorithm for 3D segmentation (Step No.4-6). IIPE (Step No.7) is introduced to maximize the number of extractable particles from highly concentrated particle holograms. Finally, the entire DIH particle extraction process is accelerated using graphics processing units (GPUs), which reduces the computation time required for DIH processing (e.g. ~ 15 minutes, depending on number of particles, for a 2k×2k holograms with 1024 longitudinal scans on a system with an Intel Core i5-4690S 3.20 GHz CPU, a GeForce GTX 970 GPU and a 16 GB RAM).

Below, first we will present the working principle of DIH imaging and then a detailed description of the abovementioned new ingredients introduced for DIH-PTV particle extraction processing including their mathematical frameworks, algorithms and the test results using holographic data from experiments and synthetic simulations.

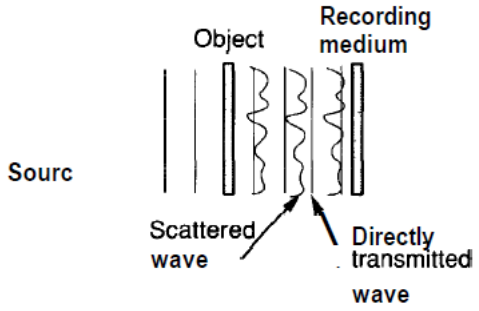

Figure 3.6 The geometry Gabor hologram recording geometry (Goodman 1968).

3.2.1 Principles of Digital Inline Holographic Imaging

In 1948, Dennis Gabor (Gabor 1948) proposed a novel two-step, lens-less imaging process (see Figure 3.6) which he called wavefront reconstruction or holography (Goodman 1968). He recognized that in presence of a coherent light beam as an illumination source the light interference of the reference wave and the reflected, diffracted or scattered light from the objects results in a wave front that includes the information of both phase and amplitude of the generated light waves. This wave-front consists of two components: (1) reference planar wave (r, constant) and (2) scattered wave generated by presence of objects, $u_p(x,y)$.

In general, 3D imaging using holography includes two major steps of recording and reconstrcution. In brief, in the recording phase the 3D information of the object field is recorded and compressed onto a 2D image (hologram). The 3D image of the object field is then reconstructed through decoding the correpsonding fringe patterns on the hologram. Below, these two phases are introduced in more detial separately.

The inline holographic imaging set-up only includes a coherent light source (e.g. a laser) and an imaging device including a camera (e.g. a charge-coupled device (CCD) or a complementary metal–oxide–semiconductor (CMOS)). This set-up can be equiped with a spatial filter, a collimator lens and an imaging lens to achive better incoming illumination quality and desired magnification. Figure 3.1 shows a schematic of a digital inline holographic microscopic (DIHM) imaging set-up. The holographic imaging set-up with these components benefits from higher quality incoming wave-front as well as uniformity of the magnification within the sampling volume. Nevertheless, the DIH set-up can be simplified to only a laser and a camera, which makes it adequate for application where miniaturization of the optical sensing system is required (e.g. lab-on-chip device developments).

Since the recording media (digital camera or traditional photographic films/holograms) are only capable of recording light intensity, a holographic recording is mathematically formulated as:

$$I_h(x_h, y_h) = |u_h(x_h, y_h)|^2 = \left|u_p(x_h, y_h) + r\right|^2 = u_p u_p^* + r r^* + u_p r^* + r u_p^* \quad (3.1)$$

where the asterisk and (x_h, y_h) show the complex conjugate and the coordinate system on the hologram or sensor plane, respectively. The first and the second terms are the DC term and the noise terms, respectively. The third and fourth terms of the equation are responsible for generating the interference pattern where the 3D information of shape and position of objects are encoded. Specifically, as it is shown in Figure 3.7, this 3-D information is stored in two major frequencies of the fringe patterns on the hologram (i.e. high and low frequencies that include the longitudinal location and the size information of the illuminated object). For example, for a spherical particle the high-frequency component is a function of $(x^2+y^2+z^2)/\lambda z$ while the low frequency component of the fringe patterns vary with $(x^2+y^2+z^2)D_p/\lambda z$ (Katz and Sheng 2010), where x,y, and z represent the object 3D location, D_p is the particle diameter and λ shows the illumination wavelength.

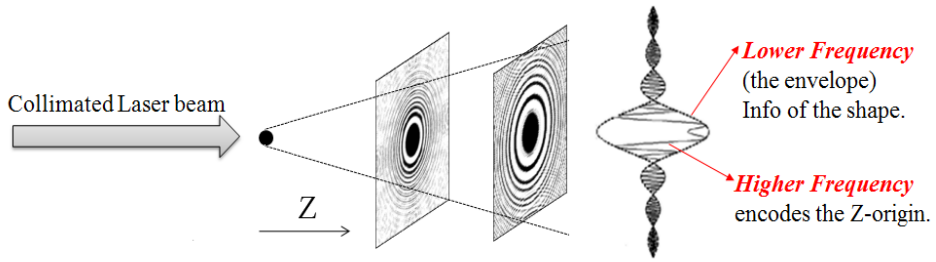

Figure 3.7 Schematic of holographic interference pattern for a spherical particle.

3.2.2 Increasing longitudinal resolution: 3D deconvolution

To increase the longitudinal resolution of DIH-PTV, we adapt the computational deconvolution approach, used in conventional fluorescence microscopy, for processing tracer particle holograms. For completeness, we will first briefly describe the reconstruction process of DIH, and then discuss the DIH deconvolution approach in detail.

After normalizing the object coordinates to those of the image plane, the DIH becomes a linear space-invariant imaging system and as a result the object-image relation can be formulated as a convolution integral of diffraction point spread function (PSF) and the 3D object (Goodman 1968). Deriving from simplified version of Max-well equations (i.e. Helmholtz equation), a variety of diffraction models are presented for the PSF of inline holographic imaging system. For example, two most frequently PSF models are:

- Rayleigh-Sommerfeld:

$$h\,(x,y,z) = \frac{1}{j\lambda\sqrt{x^2+y^2+z^2}}\,exp\,[jk\left(\sqrt{x^2+y^2+z^2}\right)] \qquad (3.2)$$

- Kirchhoff-Fresnel:

$$h\,(x,y,z) = \frac{\exp(jkz)}{j\lambda z}\,exp\,[\frac{jk}{2z}(x^2+y^2)] \qquad (3.3)$$

where k is the propagation vector and λ is the wavelength length of the illumination beam. Notably, the Kirchhoff-Fresnel is a simplified version of Rayleigh-Sommerfeld formula under the assumption of paraxial approximation, i.e., $\sqrt{x^2+y^2} \ll z$. In DIH imaging, by treating the recorded hologram as a 2D aperture the 3D image of the objects (the 3-D complex optical field) can be reconstructed through:

$$u_p(x,y,z) = I_h(x,y) \otimes h(x,y,z) \qquad (3.4)$$

where u_p is the reconstructed 3D optical field, x,y, and z are lateral and longitudinal locations respectively, $\otimes$ represents the convolution operator and h (x,y,z) is the point-spread function (PSF) introduced by diffraction. Therefore, the 3D image of the objects can be scanned at any in-depth/longitudinal location. This highlights the great advantage of inline holography for 3D imaging through digitally refocusing of a single shot in comparison to other 3D imaging methods which either require multi-view recording or expensive hardware for scanning mechanism.

In order to accelerate the computation, the convolution integral is usually calculated as a simple multiplication in the Fourier domain using fast Fourier transform as below:

$$u_p(x,y,z) = FFT^{-1}\{FFT[I_h(x,y)] \times FFT[h(x,y,z)]\} \quad (3.5)$$

where *FFT* [] represents the fast Fourier transform operator. In brief, through convolving the recorded hologram (I_h(x,y)) with the diffraction PSF (h(x,y,z)), the corresponding 3D optical field including stack of longitudinal scans is reconstructed. Figure 3.8a shows reconstructed optical field of a particle hologram recorded from 2 μm particles scanned at two different longitudinal locations. This optical field represents the 3D image of the corresponding particle field, which suffers from DOF problem and noises associated with the cross-interference of adjacent objects and out-of-focus objects. Due to DOF the 3D image of any object is extended much larger than its actual size in the longitudinal direction in the 3D reconstructed optical field, which consequently limits the longitudinal accuracy of DIH-PIV/PTV. Figure 3.8b shows the 3D reconstructed optical field of a 2 μm spherical particle on its lateral and longitudinal in-focus planes, which clearly highlights the longitudinal elongation of particles in DIH. In addition, since in DIH imaging both virtual and real images are on the same axis, the overlapping twin images (i.e. coexistence of both real and virtual image objects at any reconstructed depth) worsens the depth of focus in holographic measurement (see Figure 3.8c).

Similar problem (i.e. DOF and out-of-focus noise) is present in another linear and space-invariant imaging system, i.e. florescence microscopy, where the volumetric information of objects is captured on a stack of imaging planes at different longitudinal positions. In florescence microscopy, this problem was first tackled through a computational image restoration technique called deconvolution by Agard (1984).

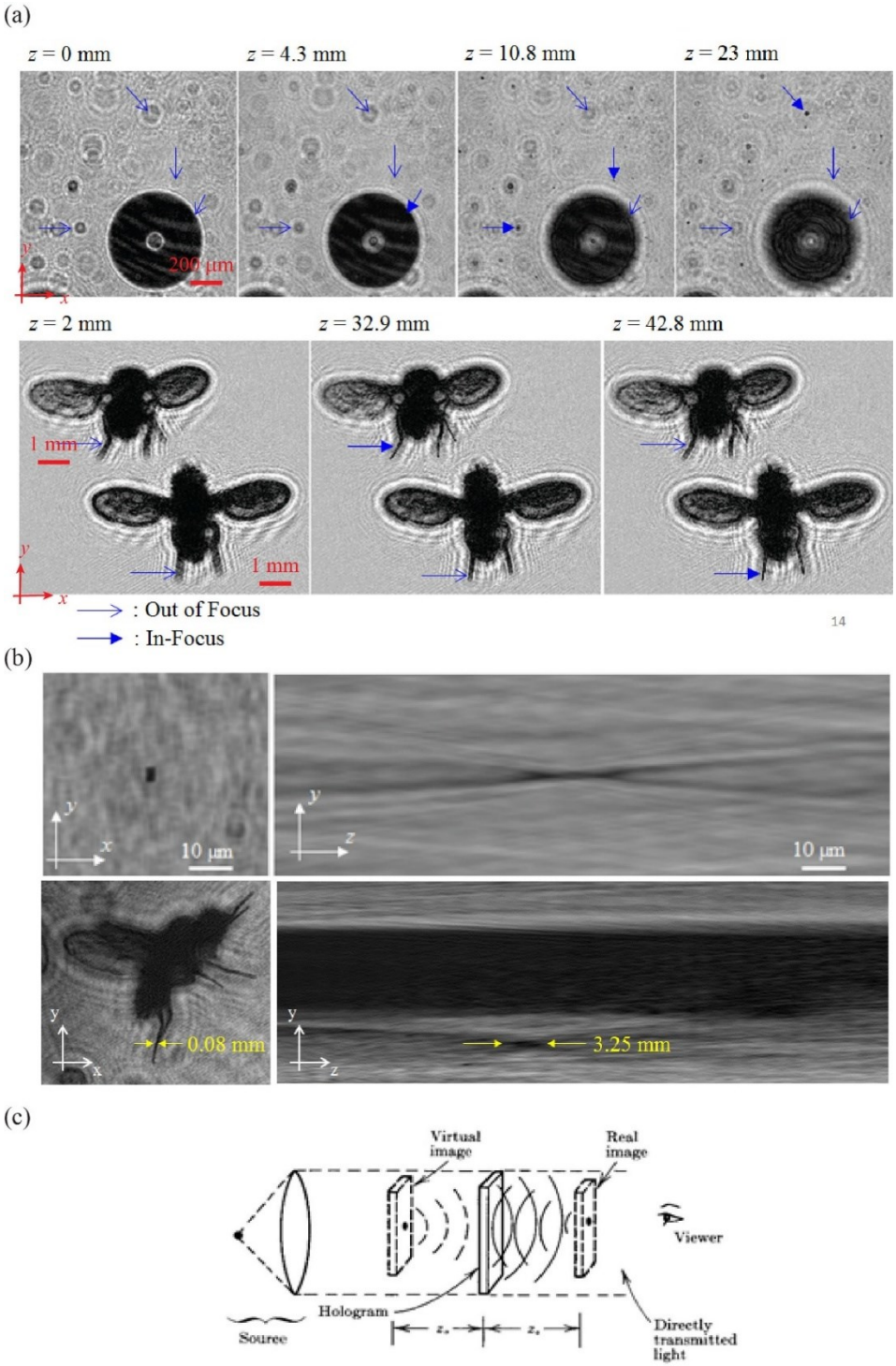

Figure 3.8: (a) Samples of reconstructed scans for application of DIH to particle laden multi-phase flow (top) and flying fruit flies (bottom) (b) and in-focus lateral (left) and longitudinal (right) in-focus planes of the 3D reconstructed optical fields for a 2 μm spherical particle (top) and a single flying fruit fly (bottom), and (c) a schematic illustration of twin images coexistence in in in-line holographic imaging (Goodman 1968).

The 3D deconvolution based on Wiener filtering formulation was successfully adapted for DIH images through instant 3D deconvolution, and was proved to reduce the DOF and consequently increase the longitudinal resolution significantly (Latychevskaia *et al.* 2010, Dixon *et al.* 2011 and Latychevskaia and Fink 2014). An iterative scheme for 3D deconvolution of holograms was also proposed by Latychevskaia *et al.* (2010), which requires larger memory and higher computational cost. We have tested the performance of both instant and iterative deconvolution schemes for concentrated particle fields, which shows that the instant scheme detects higher number of particle traces with lower SNRs compared to the iterative scheme. Therefore, to extract more particles with a feasible computational time, we employ instant 3D deconvolution for DIH-PTV processing. The drawback of a lower SNR compared to that of the iterative approach is also resolved in the subsequent processing steps of our method. The instant deconvolution scheme computes the deconvolved 3D optical field as follows:

$$u_{p'}(x,y,z) = F^{-1}\left\{\frac{F[I_{PSF}(x,y,z)]^* \times F[I_p(x,y,z)]}{(F[I_{PSF}(x,y,z)]\times F[I_{PSF}(x,y,z)]^*)+\beta}\right\} \qquad (3.6)$$

where I_{PSF} and I_P represent the intensity distributions of PSF of the optical system and the original reconstructed 3D optical field, respectively, u'_p is the corresponding deconvolved field, and β is a small constant used to prevent probable divisions by zero. The value of β should be smaller than the magnitude of the other term in the denominator, and is selected as ~0.5 for a wide range of tested tracer holograms. The 3D PSF function of the optical system (I_{PSF}) is modeled, using Rayleigh-Sommerfield's diffraction, as a 3D reconstruction of a synthetic hologram generated for a one pixel size aperture located in the center of measurement volume. It is noteworthy that the 3D PSF function can be also obtained experimentally through reconstruction of a hologram of a point-like object.

To demonstrate the improvement using this method, the reconstructed 3D optical fields from a tracer field hologram before and after deconvolution are presented in Figure 3.9. The hologram is obtained from a flow experiment in a 1×1 mm^2 cross-section microchannel operated with water seeded with 2 μm silver coated silica particles. As Figure 3.9d-e shows, the DOF of the particle field is reduced ~ 20%-40% of its original length after deconvolution. In addition, the distinction between in-focus particles and the background

noises from out-of-focus particles is improved substantially, as illustrated in Figure 3.9c and Figure 3.9d.

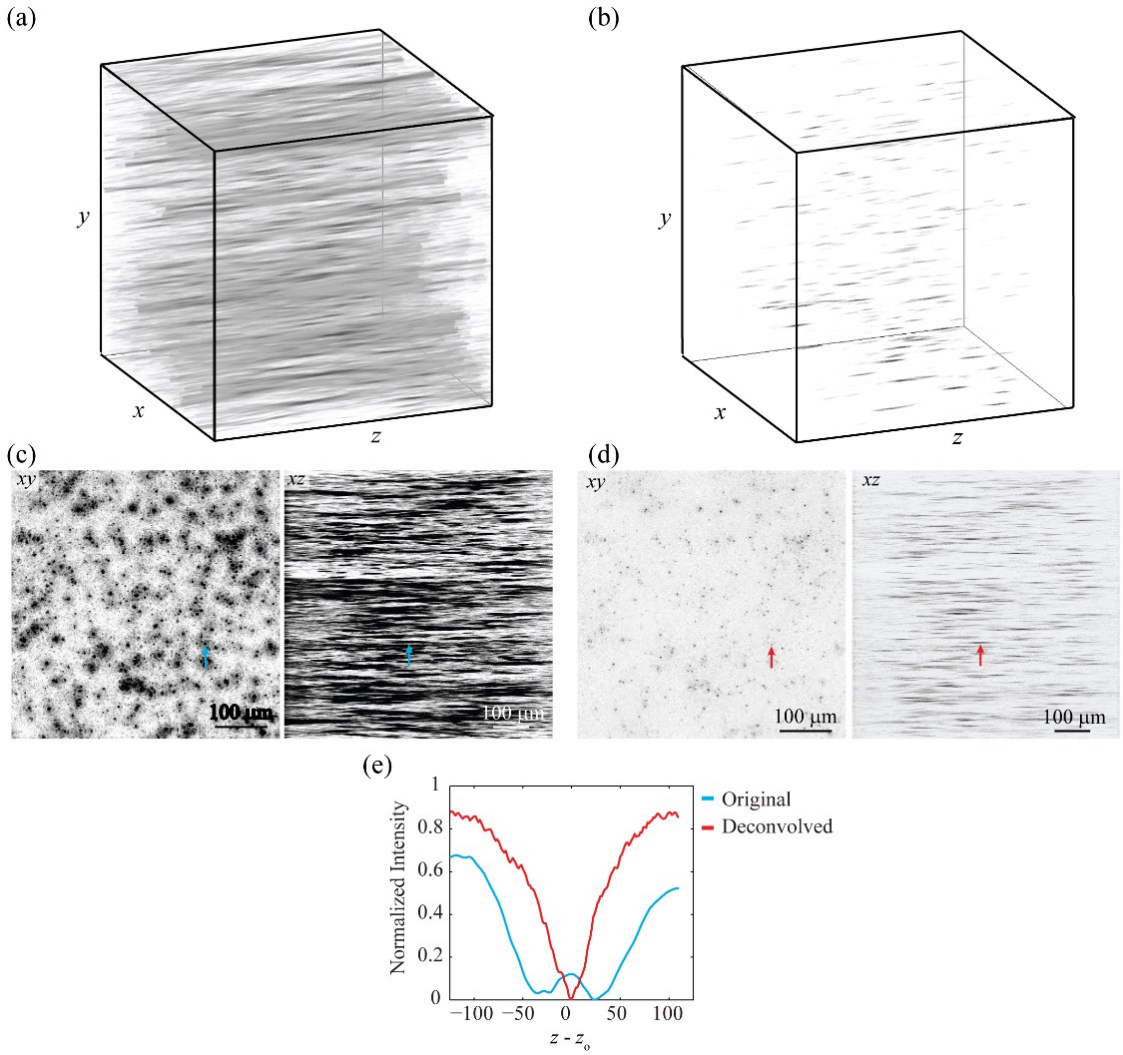

Figure 3.9: (a) Original and (b) deconvolved 3D reconstruction of a sample hologram of 2 μm-diameter silver coated silica tracer particles. (c) The *xy* and *xz* plane minimum intensity maps of (c) the original and (d) the deconvolved 3D optical fields. (e) A normalized longitudinal intensity profile of a sample particle before and after deconvolution at the location pointed by the arrow. Note that the intensity values at different longitudinal locations presented here are the mean values averaged over the lateral cross-sections of the particle.

However, despite the significant improvement of the longitudinal and lateral resolution, large variation in the intensity distribution of particles and the SNR still remains across the reconstructed 3D optical field after deconvolution, similar to that in the original reconstruction. This variation of SNR is caused by several factors including

inhomogeneous tracer concentration in the measurement volume, e.g. variation of particle-particle lateral closeness, and variations in particle size in the measurement volume, etc. In addition, the current deconvolution process inevitably reduces or even eliminates the signature of tracer particles close to the borders of measurement volume or whose fringes are contaminated by neighboring objects. This drawback results in significantly less detectable tracers, and subsequently reduces the spatial resolution of vector fields for DIH-PTV. These issues that are remained after deconvolution or induced by deconvolution will be addressed in subsequent sections 3.2.3 and 3.2.4.

3.2.3 Eliminating human intervention: automatic 3D SNR enhancement, thresholding and segmentation

To minimize human intervention and consequently reduce measurement uncertainty during particle extraction, we develop a high-fidelity automatic process to segment 3D particles from a reconstructed 3D optical field. As mentioned in Sec. 3.2.2, a large variation of SNR still remains across the reconstructed 3D optical field after deconvolution. Therefore, a single value of intensity threshold (e.g. Guildenbecher *et al.* 2012) is not adequate for segmenting tracer particles effectively in DIH-PTV applications, leading to different degrees of oversampling or under-sampling of objects. To overcome this issue, Singh and Panigrahi (2015) proposed a 2D automatic thresholding technique that calculates a set of different threshold values for each reconstructed cross sections. Although this approach takes into account the longitudinal variation of SNR, it is ineffective to deal with the variation of threshold due to the particle concentration inhomogeneity along the lateral directions. On the other hand, the existing approach using 3D thresholding (Sheng *et al.* 2006) involves a number of user defined parameters and may introduce measurement uncertainty caused by human intervention. To overcome these issues, our proposed method consists of three steps. The intensity of the deconvolved 3D optical field is first equalized using a 3D local SNR enhancement. Then, a threshold calculation algorithm is applied to automatically determine the optimal intensity threshold for the entire optical field. Finally, the 3D objects are formed by joining neighboring voxels together within the thresholded optical field. The detail description of each step is provided below.

3D Local SNR Enhancement: The 3D local SNR enhancement first divides the deconvolved optical field into object domain and background using a single threshold, and

then performs local intensity normalization on the object domain. The threshold for isolating background from regions with particles, I_{Thr0}, is automatically determined using 2D minimum intensity map of the optical field as follows:

$$I_{Thr0} = Avg(I_{min}) - Avg(I_{\sigma}) - \sigma\,(I_{\sigma}) \qquad (3.7)$$

where $Avg()$ and $\sigma()$ are average and standard deviation operators, I_{min} and I_{σ} represent the minimum and standard deviation of intensity of pixels within an interrogation window which scans over the entire 2D minimum intensity map of the optical field with 50% overlap. The size of interrogation window is selected to be $4\times D_p$ in order to preserve sufficient information of the particle fringes, where D_p is the particle diameter, e.g. 8 × 8 pixels for 2 × 2 pixels particles. Considering the objects (i.e. tracer particles) are dark spots in the optical field, the background is defined as the domain with voxel intensities above I_{Thr0} and these voxels are assigned with the value of the maximum intensity of the 3D optical field. The subsequent local intensity normalization is conducted through 3D min-max filtering over the object domain as below:

$$I'(x,y,z) = \frac{I(x,y,z) - \mathrm{Min}(I_{\forall})}{\mathrm{Max}\,(I_{\forall}) - \mathrm{Min}(I_{\forall})} \qquad (3.8)$$

where $I\,(x, y, z)$ and $I'\,(x, y, z)$ are the original and the normalized intensity values of a voxel located at (x, y, z), respectively, and the Min() and Max() are the minimum and maximum calculation operators, respectively, and I_v represents the intensity distribution within the corresponding interrogation block shifting over the entire object domain with 50% overlap. The size of these blocks is determined using the DOF estimate of particle objects through synthetic hologram simulation with similar magnification and for largest tracer used in the experiment. The DOF is defined as the distance between the 75% intensity peaks around the particle centroids (Sheng *et al.* 2006), and to account for the noises present in the actual experiment, we double the synthetically calculated DOF as an estimate of DOF. This estimate is in a good agreement with the available experimental data of similar magnifications and particle sizes (e.g. (Sheng *et al.* 2006)).

To demonstrate the effectiveness of this method, Figure 3.10a and Figure 3.10b show the *xy* and *xz* minimum intensity maps from the same 3D optical field used in Fig. 3, before and after 3D local SNR enhancement. As the figures show, the uniformity of particle intensity is improved and the background noise is suppressed significantly after 3D SNR

enhancement, which facilitates the subsequent processing steps. It is noteworthy that particle concentrations, C_p, for experimental holograms are calculated from the tracking trajectories of particles in time, i.e. only those particles are counted real that are present in trajectories with matching pairs from five consecutive holograms.

Automatic thresholding: After 3D local SNR enhancement, a single threshold value can be applied to the entire measurement volume to segment the particles from the background. The value is automatically determined using intensity histogram of *xy* 2D minimum intensity map of the reconstructed 3D optical field. As shown in Figure 3.10c, a clear separation between background and objects is achieved after SNR enhancement. Therefore, the detection threshold value is automatically calculated from the histogram of intensity values of the SNR enhanced minimum intensity map by finding the maximum intensity within the object domain.

Local thresholding window size adjustment: in the first version of the automatic thresholding algorithm proposed in Toloui and Hong (2015), a single threshold is used for isolating background from regions with particles in the 3D reconstructed optical field. The threshold value is automatically determined through scanning the 2D minimum intensity map using window sizes of four times the tracer particle diameter (D_p) for all iterations of particle extraction. Although this method worked effectively for holograms representing small sampling volumes (e.g. micro-channels or turbulent channel flows with local seeding), it results in under-sampling of tracers in the holograms acquired from volumetrically seeded large sampling volumes. To overcome this issue, the algorithm is improved by modifying the thresholding window size in each iteration. Specifically, the thresholding starts with a window size of $6\times D_p$ and the window size decreases in a step of D_p after each iteration (until reaching a size of D_p). We implemented this modified method for holograms of a sampling volume of $14.7 \times 50 \times 14.4$ mm^3, which results in up to 40% increase in the number of extractable tracers from the holograms.

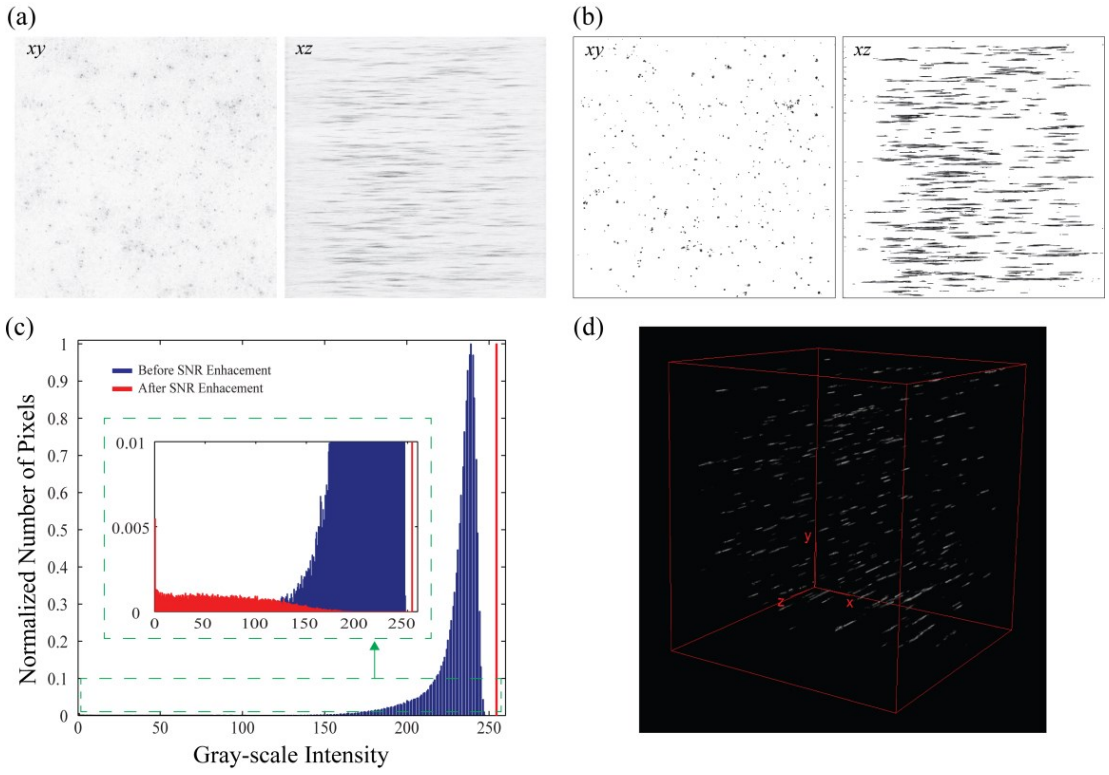

Figure 3.10: The *xy* and *xz* plane minimum intensity maps of the deconvolved 3D reconstruction (a) before and (b) after 3D local SNR enhancement, for $Cp \approx 3000$ particles/mm^3. (c) The intensity distribution profiles of minimum intensity images after and before 3D local SNR enhancement for (d) corresponding thresholded and 3D segmented particle field.

3D object segmentation: After automatic thresholding, the 3D object segmentation algorithm joins the 2D segments into 3D objects through merge operator connecting thresholded voxels located within certain distance from each other as shown in Figure 3.10d. Through preliminary testing, the distance is selected to be $2\times D_p$. To reduce the false positives during particle segmentation, a subsequent size filter is applied to eliminate false particles. It is noteworthy that unlike tomographic PIV where the size of the reconstructed particles does not reveal an appreciable difference between fake and real particles (Elsinga 2013), there is a distinction between particles and noises in DIH-PTV. The fake particles resulted from cross-interference or out-of-focus diffraction do not exhibit clear longitudinal elongation, and therefore yield considerably smaller longitudinal length compared to real ones. The lowest estimate of DOF for the particle field is employed in order to perform this filtration on detected 3D blobs, i.e. particles are those blobs with longitudinal length longer or equal to this DOF length. This length criterion is automatically calculated through a

synthetic hologram simulation with similar magnification and for smallest tracer size used in the experiment. Particle centroids (x_i, y_i, z_i), diameters (D_{pi}) and in-focus cross sections (A_{pi}) are finally calculated based on geometrical center for filtered 3D blobs. A velocity vector field is calculated for any two consecutive holograms using their corresponding extracted centroid fields (i.e. x_i, y_i, z_i).

3.2.4 Increasing detectable particle concentration: iterative inverse particle extraction

As mentioned in Sec. 3.2.2, the current 3D deconvolution process inevitably reduces or eliminates the signature of particle objects, specifically for those contaminated by cross-interference and those located close to the borders of reconstructed 3D optical field. The latter case results in truncation of the signal from 3D particle image, which reduces its correlation with the prescribed PSF (Latychevskaia and Fink 2014). These issues significantly limit the concentration of particles that can be segmented effectively.

To increase the concentration of detectable particles, an algorithm is developed to keep updating the reconstructed 3D optical field by removing extracted particles from it and conduct the aforementioned particle extraction steps on the updated optical field in an iterative fashion. This algorithm, namely iterative inverse particle extraction (IIPE), can accentuate the fringe patterns of the previously contaminated/hidden particles, allowing higher concentration of particles to be extracted. Specifically, each extracted particle is removed from the reconstructed optical field by filling its in-focus cross section with the average complex value of the reconstructed optical field (background). The updated optical field (with extracted particles signature removed) is then used to generate the updated hologram through backward diffraction for the next round of particle extraction. This iterative process can be formulated in following steps:

$$u_p(A_{pi}(x_i, y_i), z_i)|_n = Avg\,(u_p\,(x, y, z_i))\,|_n \qquad (3.9)$$

$$I_h^{'}\,|_{n+1}(x,y) = \; u_p(x,y,z_i)|_n \otimes h(x,y,z_i) \quad \& \quad i{=}i{+}1 \qquad (3.10)$$

where i represents the particle ID number ranging from 1 to N_p (the total number of detected particles at removal iteration n), A_{pi} is the in-focus cross section of particle i (calculated in 3D object segmentation step), and $I'_h|_n$ and $u_p(x,y,z_i)_n$ represent the particle removed hologram and the corresponding particle-removed optical field after n iterations, respectively. Note that the order of particles does not matter in our particle removal

process, and each iteration ends when all the detected particles from previous iteration are removed, i.e. $i = N_p$. The flowchart of IIPE algorithm is also depicted in Figure 3.11a.

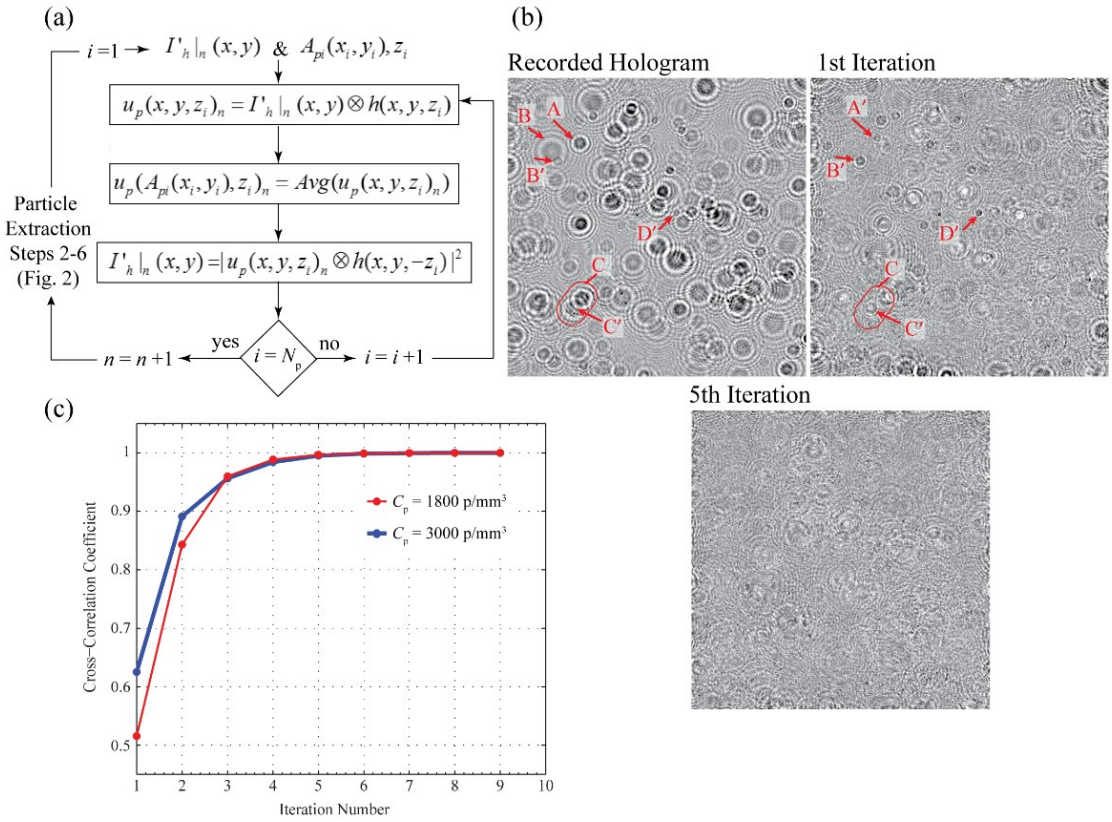

Figure 3.11: (a) The IIPE algorithm flowchart. (b) Iterative particle-removal (for hologram C_p = 1800 particles/mm^3): recorded and the corresponding particle-removed holograms after different iterations. To provide examples of the particle removal, the letter symbols without prime are used to mark a few particles with high SNR that are extracted in the first iteration. The particles marked using letter symbols with prime indicate the particles whose fringe patterns are recovered/enhanced after removing those high SNR particles in the first iteration (e.g. After removing the particle A in the first iteration, the fringes of particle A' which is laterally-close to A but at different longitudinal location appears). (c) The cross-correlation between successive particle-removed holograms for both cases of $C_p \approx$ 1800 and 3000 particles/mm^3.

The iteration ends when the cross-correlation coefficient of the two consecutive updated holograms reaches 0.99, indicating that there is almost no particle that can be further extracted from the updated holograms. To illustrate this process, the iterative inverse particle extraction is implemented on the same hologram used in Figure 3.9 and 3.10 (see Figure 3.11b). As the figure shows, substantial number of particles can be

extracted through each iteration, and the entire process ends after 5 iterations when the cross-correlation coefficient exceeds the value of 0.99 (see Figure 3.11c). Compared with single-pass particle extraction, about 30% more particles are extracted through the iterative inverse algorithm from the experimental holograms of the laminar flow within a 1×1 mm^2 cross-section microchannel seeded with 2000-3000 particles/mm^3 of 2 μm particles. This result highlights the necessity and effectiveness of IIPE for DIH-PTV.

Notably, our approach of particle removal is fundamentally different from the inverse algorithm proposed by Soulez *et al.* (2007). Specifically, our approach is performed in the 3D reconstructed optical field and does not require synthesizing model holograms. In addition, the technique proposed by Soulez *et al.* (2007) performs the removal on the hologram plane, which can alter the fringes of particles located laterally close to the removed particles, causing larger uncertainty and lower extraction rate for concentrated holograms. In contrast, the proposed method here enables particle removal from highly-concentrated field without deteriorating the fringes of residual particles, and thus it elevates the SNR of previously hidden/distorted particles to a sufficient level for being extracted.

3.2.5 Particle extraction assessment

In inline holography, different experimental parameters such as volume depth (L_z), particle concentration (C_p) and particle size (D_p) have substantial effects on SNR, and consequently the rate and position accuracy of particle extraction (Meng *et al.* 1993, Malek, *et al.* 2004 and Zhang *et al.* 2006). In order to quantify these effects on the accuracy and effectiveness of our particle extraction method, we implemented the algorithm on a set of synthetic holograms generated using Rayleigh-Sommerfield diffraction theory, similar to the approach used by Zhang *et al.* (2006) and Soulez *et al.* (2007). Following the approach employed by Gao (2014), the 512×512 synthetic holograms are cropped out of originally simulated holograms of size 2048×2048 to reduce the aliasing effect. A total of 30 holograms are synthesized with the hologram plane to particle field distance of 600 μm, and the lateral resolution of 1 μm/pixel and the illumination of 632 nm laser. The particle hologram includes randomly distributed monodisperse tracers with C_p ranging from 1600−4800 particles/mm^3. Different tracer size (i.e. D_p = 3 and 6 μm) and volume depth (i.e. L_z = 0.5 and 1 mm) are employed. After implementing our particle extraction

algorithm, the extracted particle centroids are compared to their extract pairs in order to quantify the extraction rate (E_p) and position error (δ) of our algorithm for each hologram. Using the distribution of positioning errors for all particles within a hologram (positioning error for a particle is the distance between its exact and calculated centroids), δ is defined for each hologram as the maximum positioning error for individual particles which 95% of the particles lie within $-\delta$ *to* δ. In addition, the extraction rate is calculated for each hologram as the ratio of accurately extracted particles, i.e. the particles extracted with positioning errors of $\delta \leq 2 \times D_p$, to the total number of particles.

The results of particle extraction for all 30 holograms are presented in Fig. 6. The comparison between the particle fields extracted for holograms of $D_p = 3$ µm and $L_z = 0.5$ mm using iterative (IIPE) and non-iterative algorithms , Figure 3.12a, shows that the E_p drops ~ 60% as the particle concentration increases from 1600 to 4800 particles/mm^3 without IIPE, while the extraction rate stays above 97% using IIPE algorithm. It is noteworthy that the number of falsely extracted particles is less than 3% of the total number of particles using IIPE method for all of the test cases. These results highlight the effectiveness of our novel inverse iterative particle extraction method compared to the non-iterative approach, which is particularly important for DIH-PTV where the spatial resolution and accuracy of velocity measurements are directly related to extracted particle concentration. As Figure 3.12a shows, the current algorithm can reconstruct the 3D particle fields up to < 55 µm particle spacing within a 1 mm^3 for highly concentrated particle fields (C_p > 3000 particles/mm^3).

It is noteworthy that the shadow density ($Sd = C_p \times D_p^2 \times L_z$, introduced by Royer 1974), which has been commonly used to estimate the SNR and extraction efficiency (e.g. Malek, *et al.* 2004 and Gao 2014), does not serve as an appropriate parameter to evaluate the particle extraction rate of our method, which has stronger dependency on L_z than D_p. For example, comparing the case of $D_p = 6$ µm and $L_z = 0.5$ mm with $D_p = 3$ µm and $L_z = 1$ mm, our method results in higher E_p for $D_p = 6$ µm and $L_z = 0.5$ mm whose Sd is double of the other. Similarly, the shadow density fails to estimate the positioning error variations, since its variation depends more on D_p than L_z , as shown in Figure 3.12b. The positioning error (δ) for $D_p = 3$ µm and $L_z = 0.5$ is almost the same as that of the case with $D_p = 3$ µm and $L_z = 1$ mm, while Sd for the first case is the half of the second one. This higher

dependency of δ can be attributed to DOF relation with D_p (i.e. DOF $\propto D_p^2/\lambda$, from Katz and Sheng 2010).

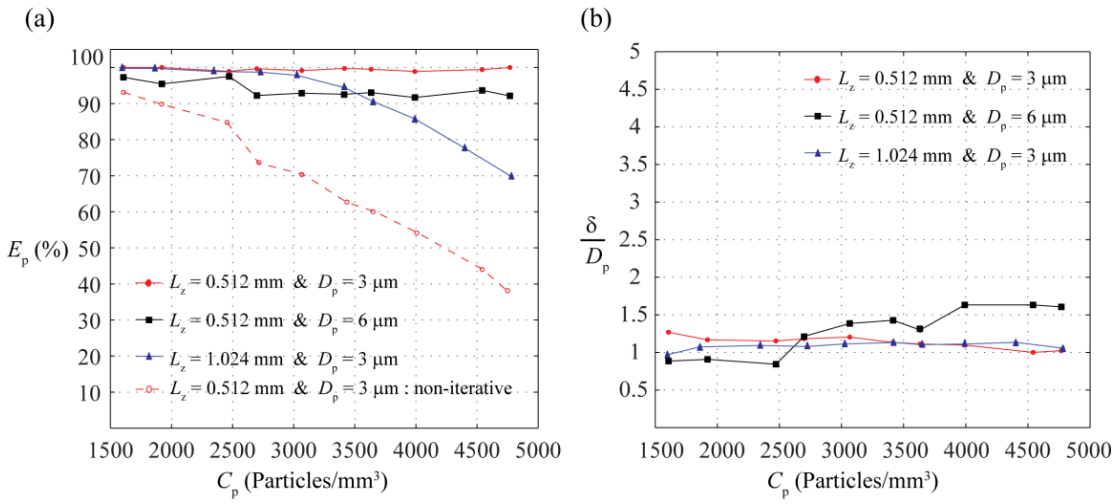

Figure 3.12: The variation of (a) particle extraction rate and (b) positioning error with particle concentration, diameter and measurement volume obtained from the hologram simulation using synthetic particle fields.

Moreover, for 3D PIV implementations, small-size particle tracers are usually employed to yield good traceability, and high tracer concentration and large sample volume are generally favored for capturing flow structures with broad dynamic range of scales. These requirements indicate the significance of both C_p and L_z, in contrast to the shadow density, for evaluating the accuracy and effectiveness of DIH-PTV.

3.3 Velocity/Displacement Field Calculation

3.3.1 Multi-pass 3D Tracking

In DIH-PTV, the 3D velocity fields for every pair of successively recorded holograms are calculated through implementation of 3D tracking on extracted particles fields (i.e. the centroids of elongated particle ellipsoids). Several different methods of 3D tracking has been developed and implemented in DIH-PTV and other 3D PTV methods (e.g. Yu *et al.* 2014, Pierra *et al.* 2006). PTV techniques typically use the nearest neighbor criteria to identify particle pairs (tracks/trajectories), which leads to particle misidentification for cases with high seeding densities, which are proper for high resolution velocimetry. Similarly, majority of DIH-PTV studies have been focused on low or moderate seeding densities within a sampling volume with limited longitudinal length. Therefore, to avoid particle misidentification and track the particle motions within dense particle solutions (C_p

≥ 3000 particles within 1024 × 1024 holograms), we developed a multi-pass 3D tracking algorithm utilizing an iterative predictor–corrector scheme that limits the number of possible particle candidates and increases the validity of tracks. Specifically, in the first pass we obtain a coarse displacement field through restricting the validity of a trajectory to the length of the dataset (i.e. 9 sequences long trajectories in the case of implementing tracking on 10 consecutive particle fields). These tracks belong to the particles with persistent strong signal as they travel through the entire sampling volume. Then, resulted displacement field is used to calculate the displacement bounds for each particle through spatial interpolation. In order to achieve higher number of valid tracks with more accurate displacements in each time step, these local bounds are used and then updated in the following passes of tracking (i.e. we iteratively refine the particle tracks). It is noteworthy that the 3D tracking at each pass is performed using an improved version of open source 3D particle tracking program developed by Crocker and Grier (1996).

To evaluate the effectiveness of our multi-pass tracking algorithm method, we implement this method on holographic recordings of a water flow in a micro-channel (Toloui and Hong 2015). This test case is selected, since the laminar flow yields a known displacement/velocity field (i.e. parabolic analytical solution). A detailed description of experimental set-up and conditions are presented in Chapter 4 (Section 4.1). A series of 10 unstructured 3D velocity fields are calculated, the corresponding streamwise velocity magnitude at different passes of the tracking algorithm as well as the corresponding percentage of tracked particles are shown in Figure 3.13. As it shows, the first pass of the tracking results in a huge number of invalid velocities (e.g. negative u values, while the flow direction $u>0$ is known). In the second pass, the velocity values of those particles with the longest tracks (i.e. 10 sequence long tracks in this experiment) are used to estimate the bounds of correct displacement across the channel. These bounds are then used in the following pass of the tracking, which results in much higher number of valid velocity values or tracks (i.e. almost the same number of tracks as of the first pass). Notably, the validity of the calculated velocities are evaluated through comparison with the parabolic profiles of a Poiseuille flow within the microchannel.

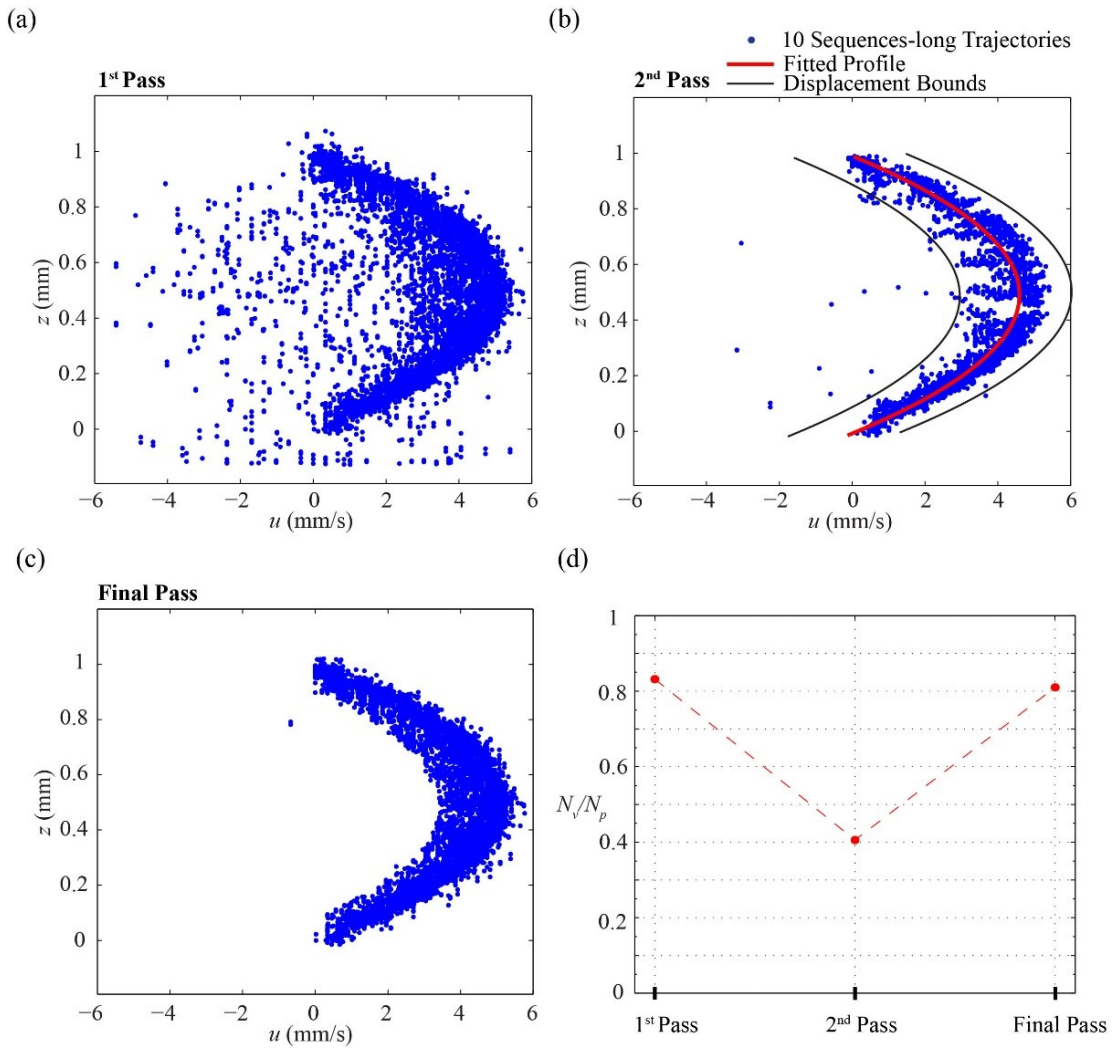

Figure 3.13: The resulted streamwise velocity distribution along the micro-channel after (a) first pass, (b) second-pass and (c) final pass of tracking. (d) The variation of tracked particles over total number of particles at different steps (passes) of tracking algorithm.

3.3.2 Cross-correlation Based Displacement Refinement

As mentioned before, the extended DOF of DIH recording results in significantly lower longitudinal resolution for 3D imaging, consequently reducing the accuracy of velocity measurements in the longitudinal direction. As shown in the Section 3.2.2, this effect can be greatly reduced through 3D deconvolution and 3D local SNR enhancement. However, the effect becomes more severe as the longitudinal extent of the sampling volume increases (above ~1 cm), limiting the implementation of the developed algorithms to sampling volumes in the scale regime of other 3D PIV techniques. Holographic recording with multiple cameras imaging the same sampling volume from different angles (e.g.

orthogonal) has so far been the most robust solution to minimize this DOF issue (Soria and Atkinson 2008). However, this approach demands a cumbersome calibration process, and similar to other multi-view 3D PIV techniques, it is difficult to apply in environments with limited optical access. To retain the intrinsic advantages of single camera DIH (i.e. low-cost, compact, single axis and easy calibration process), we improve our computational approach through coupling the multi-pass 3D tracking algorithm with a cross-correlation based refinement of the longitudinal and lateral displacement of particles. This cross-correlation based refinement method consists of two major steps as follows.

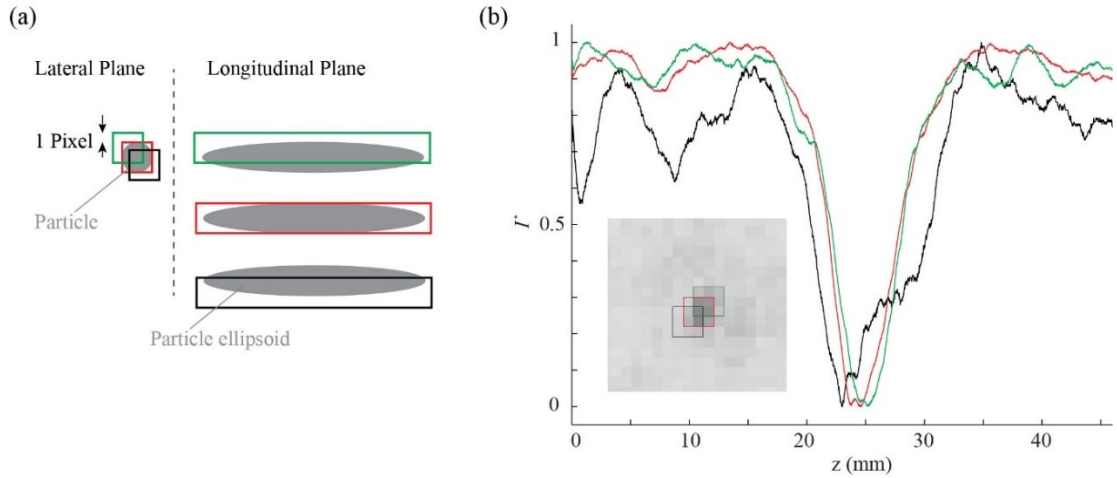

Figure 3.14: (a) A schematic showing the shifted interrogation windows around the lateral center of a particle and (b) a sample of longitudinal intensity profiles for three interrogation windows around a lateral center of a 10 µm silver-coated hollow glass sphere particle in a turbulent channel flow.

First, we extract the longitudinal intensity profiles of each particle pairs acquired from the first step. The intensity profiles are obtained using the overall 3D deconvolved optical fields for holograms, which have the same size as deconvolved fields of each iteration, and their voxels are assigned to the minimum intensity value of corresponding voxels from all IIPE iterations. For each particle, we extract its longitudinal intensity profiles by first extruding a cylinder of diameter D_p over the particle length and calculating the averaged intensity at each particle cross-section along the longitudinal direction, i.e. $\bar{I}(z)$, where z is the longitudinal coordinate. The intensity profile of each particle is then normalized using its minimum and maximum intensities as $I^*(z) = \bar{I}(z) - \bar{I}_{min} / \bar{I}_{max} - \bar{I}_{min}$. In the final step, we perform cross-correlation on intensity profiles of each particle pair to refine their longitudinal displacements. However, as shown in Figure 3.14a, any small uncertainty (e.g.

1 pixel) in the lateral position of a particle centroid will result in a significant variation in its longitudinal intensity profile and longitudinal centroid location. To address this issue, we first use an interrogation window of size $D_p \times D_p$ with its center shifted in the close proximity of the lateral location of each particle centroid and extract the corresponding longitudinal intensity profiles ($I^*(z)$). The longitudinal intensity profile from each shifted window of the first particle in each particle pair is then cross-correlated with the intensity profiles from all the shifted windows of the second particle in the pair to form a cross correlation map over different lateral and longitudinal displacements. The peak of the cross correlation map corresponds to the refined longitudinal and lateral displacements. It is noteworthy that the cross-correlation is only performed within a search domain whose size is restricted to the maximum expected longitudinal displacement.

To evaluate our cross-correlation based displacement refinement method, we implement this method on holographic recordings of a water flow in a micro-channel (the same holograms which are used in the previous Section), where the laminar flow yields a parabolic analytical solution with zero out-of-plane velocity magnitudes. A sample of instantaneous DIH-PTV recording along with its displacement measurement in both streamwise and longitudinal directions are presented in Figure 3.15b and c. The distribution of longitudinal displacement component (Figure 3.15c), clearly highlights the effectiveness of the cross-correlation method in reducing the measurement uncertainty to below 0.5 D_p.

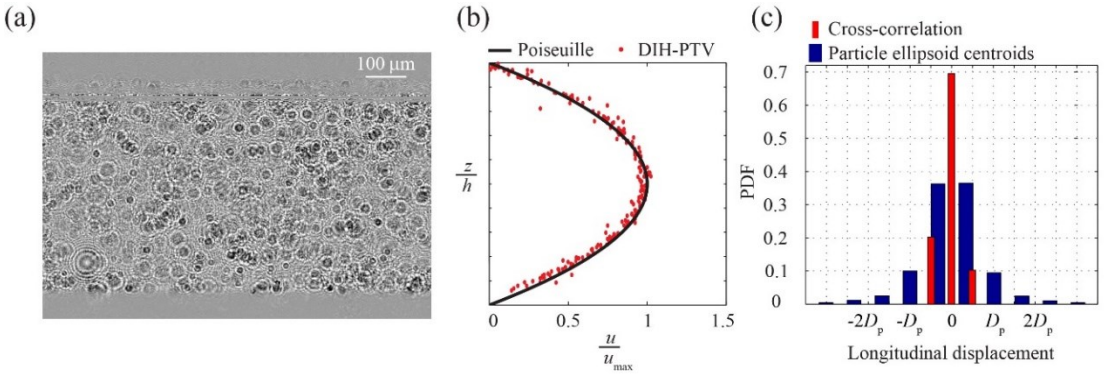

Figure 3.15: (a) A sample hologram from a water flow within micro-channel (seeded with D_p = 2 µm tracer particles of up to 3000 particles/mm^3 concentration), (b) an instantaneous streamwise velocity profile measured with DIH-PTV and (c) the histograms of the corresponding longitudinal velocity component using cross-correlation based refinement method versus geometrical centroid method.

3.4 Summary and Discussion

A novel DIH-PTV method including 3D deconvolution, automatic 3D SNR enhancement and thresholding, iterative inverse particle extraction, multi-pass 3D tracking and cross-correlation based longitudinal displacement refinement is developed and accelerated using GPU-based computational algorithm. The method is evaluated using simulated holograms consisting of concentrated synthetic particle fields with different particle concentration, particle size and volume in-depth lengths. Our method yields high accuracy of particle positioning ($\delta < 1.6\ D_p$) and high extraction rate ($E_p > 93\%$) for concentrated particle fields (up to $C_p \sim 5000$ particles/mm^3), making it an ideal method for high resolution 3D flow measurements. The method has also been implemented to quantify 3D flow fields in a laminar flow microchannel seeded with concentrated tracers ($C_p \sim 3000$ particles/mm^3).

Overall, our method has significantly improved the existing DIH-PTV approach by overcoming its major limitations including poor longitudinal resolution, human intervention and limited tracer concentration, limited sampling volume longitudinal length and expensive computations. Such improvements substantially enhance the implementation of DIH-PTV for 3D flow measurements in wide range of applications from microfluidics to turbulent channel flow measurements resulting in the potential commercialization of this technique. Moreover, our achievement has also broadened the range of DIH applications to metrology and other *in situ* measurements in highly concentrated suspensions and natural flows for characterizing 3D motion and concentration. It is also worth noting that future improvements on deconvolution algorithm, inverse iterative particle extraction scheme as well as GPU-based computation can potentially push the boundary of our method for sub-pixel resolution particle extraction with concentration above 10^5 particles/mm^3 in real-time.

Chapter 4: Application of Digital Inline Holographic PTV to Flow Measurements: from Microfluidics to Turbulent Channel Flows

Overview

The proposed DIH-PTV method has been successfully applied to measure instantaneous 3D velocity fields in a wide range of applications from micro-fluidics to turbulent channel flows. In this chapter, we present the experimental details as well as the results of some of these applications. Specifically, the applicability of the technique is validated using the experiment of laminar flow in a microchannel and the synthetic tracer flow fields replicating a DNS turbulent channel flow database. In addition, the proposed method is applied to a smooth-wall turbulent channel flow under two different settings of high-resolution near-wall and the whole-channel measurement (i.e. sampling volume covers the entire depth of the channel). In the first case, using microscopic objective and local seeding, DIH-PTV resolves near-wall flow structures within a sampling volume of $1 \times 1.5 \times 1$ mm^3 (streamwise × wall-normal × spanwise) with velocity resolution of ~100 μm per vector. In the second case, the measurement volume is extended to the whole-channel depth by seeding the entire channel. Under this setting, the 3D velocity fields are obtained within a sampling volume of $14.7 \times 50.0 \times 14.4$ mm^3 with a velocity resolution of ~1.3 mm vector spacing, comparable to other the-state-of-the-art 3D whole-field flow measurement techniques. Overall, the presented DIH-PTV measurements under two different settings highlight the potential of DIH-PTV to obtain 3D characterization of the turbulent structures over a full range of scales, covering both the near wall and the out-layer regions of wall-bounded turbulent flows.

4.1 Laminar Flow within a Micro-channel

Our DIH-PIV technique is employed to quantify 3D velocity fields from the holograms recorded for a microchannel flow experiment. A motorized syringe is used to pump the low speed (Re = 10, based on the channel width) water flow seeded up to C_p ~ 3000 particles/mm^3 with 2 μm silver coated fused silica particles through a 130 mm long glass microchannel with a 1 mm^2 square cross-section. The DIHM set-up contains a CMOS

camera (2048×1088 pixels Flare 2M360-CL), a 12 mW He-Ne laser (λ = 632 nm) as the coherent light source, a spatial filter and a collimator lens. A long working distance infinity-corrected 5X objective lens (5X EO M Plan Apo) is used to record magnified holograms of the microchannel flow with 1.1 µm/pixel lateral resolution. Figure 4.1 shows the experimental and optical set-up used in this experiment and a sample of corresponding holographic recordings.

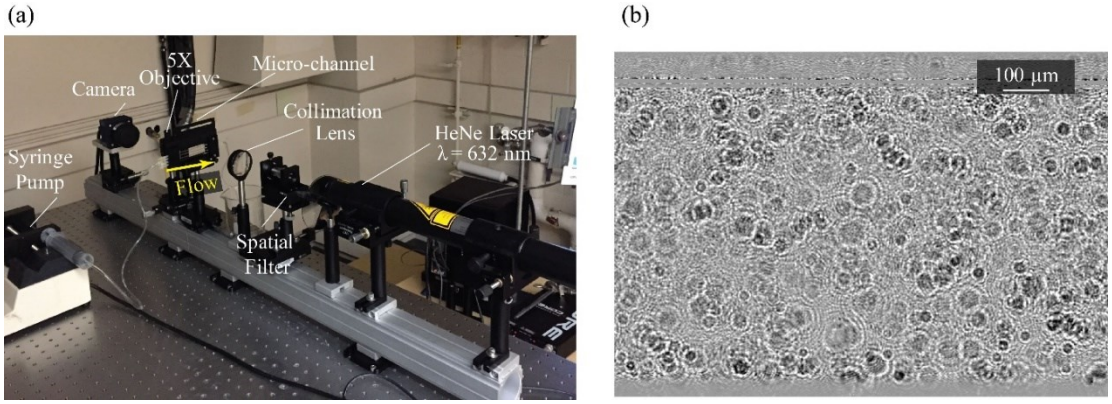

Figure 4.1: (a) Experimental set-up of DIH-PTV measurements from a micro-channel and (b) a sample hologram recorded from water flow within the micro-channel seeded with 2 µm tracer particles of up to 3000 particles/mm^3 concentration.

The 3D velocity fields are then calculated through implementing our multi-pass 3D tracking algorithm on the consecutive tracer fields extracted using five iterations of the IIPE method. The process generates a series of unstructured 3D velocity fields as illustrated in Figure 4.2a. Since the flow is fully developed within the microchannel, these velocity fields are expected to replicate the parabolic profiles of a Poiseuille flow within the microchannel. The comparison between the analytical solution (Poiseuille flow profile) and the measured stream-wise velocity profile is presented in Figure 4.2c. As it shows, our DIH-PIV measurements match the analytical solution with less than a 5% difference in magnitude, which is attributed to both the velocimetry uncertainty and the discrepancy between the flow condition within the channel and those of the analytical solution.

The 3D velocimetry capability of the DIH-PTV technique eliminates the uncertainty resulted from out-of-plane error associated with μPIV systems. Notably, through iterative particle extraction and multi-pass particle tracking the proposed DIH-PTV method provides much higher spatial resolution compared to other existing DIH-PTV methods used in microfluidics (e.g. 60-100 µm velocity resolution within 1×1×1 mm^3 or ~30-40 µm

velocity resolution within 1×0.5×1 mm^3). In addition, since holography acquires the volumetric information only in a single shot/acquisition, DIH-PTV recordings achieve superior temporal resolutions compared to confocal μPIV systems.

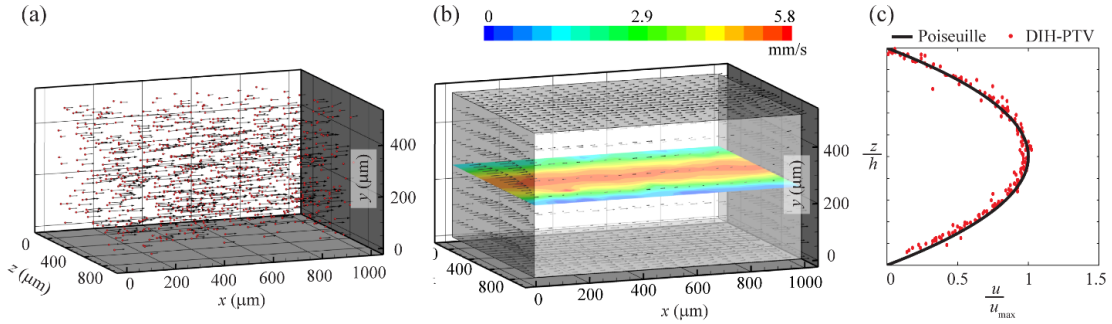

Figure 4.2: (a) A sample of instantaneous velocity vector field measured using our DIH-PIV and (b) the corresponding structured vector field superimposed with the contours of the streamwise velocity magnitude. (c) A comparison of a sample of instantaneous streamwise velocity profile measured from DIH-PIV and Poiseuille profile in the channel. The instantaneous profile is spatially averaged over a region of 50 μm thick and 100 μm in length around the *xz*-middle plane.

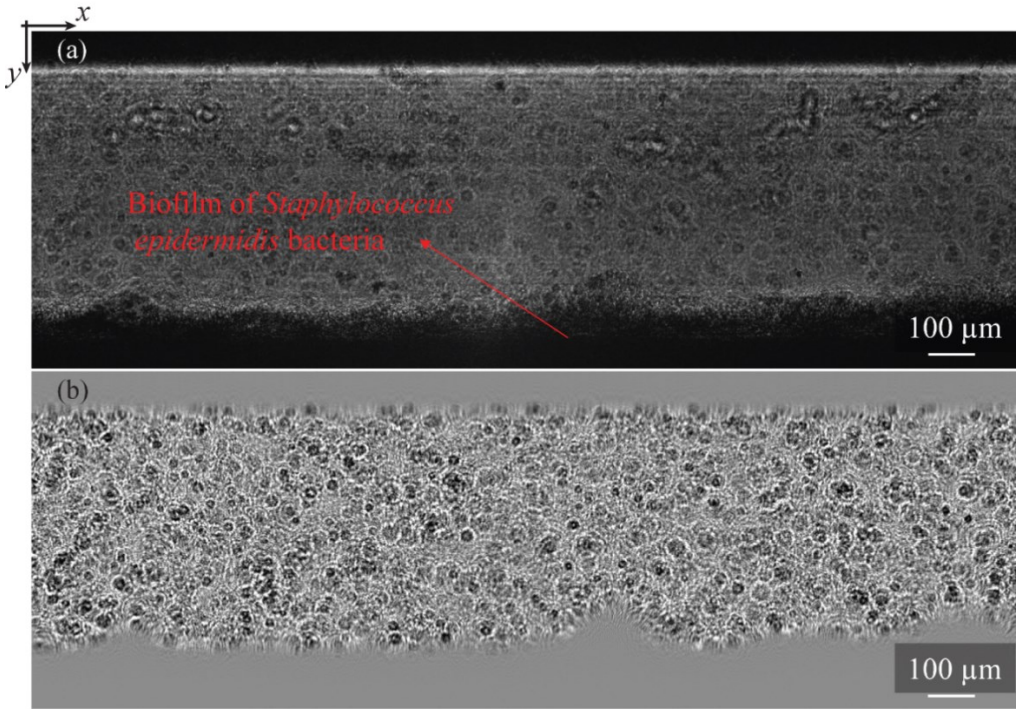

Figure 4.3: A sample of holographic recordings from the water flow over a biofilmed micro-channel seeded with 2 μm tracer particles of up to 3000 particles/mm^3 concentration: (a) before and (b) after implementation of hologram SNR enhancement and biofilm removal.

4.2 3D Flow Monitoring within a Biofilmed Microchannel

Biofilm formation, i.e. biofouling or biological fouling, changes the surface roughness, which consequently affects the near-wall hydrodynamics. For example, biofouling on vessels increases hull roughness and hydrodynamic drag (Schultz 2007), which leads to decreases in speed and maneuverability, an increase in fossil fuel consumption, and as a result increased emission of greenhouse gases (Poloczanska *et al.* 2010). In addition, the near-wall hydrodynamics regulate the biofilm development (Kim *et al.* 2014). A full understanding of this interplay between the biofilm formation and the near-wall hydrodynamics requires simultaneous monitoring of both 3D flow fields and the biofilm growth and structure.

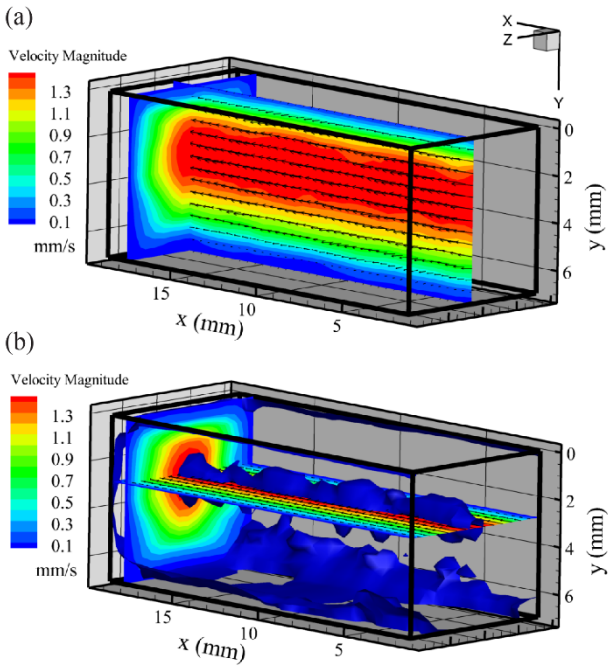

Figure 4.4: (a) A sample of instantaneous velocity field measured using our DIH-PIV and (b) the corresponding distribution of minimum vorticity magnitude representing the 3D extent of the biofilm. Note that the blue iso-surface represents the regions of minimum resolvable vorticity magnitudes.

Here, we conduct an experiment demonstrating this capability of our DIH-PTV method. Specifically, the biofilm of *Staphylococcus epidermidis* bacteria is formed on the bottom wall of a glass micro-channel of a 1 mm^2 square cross-section and 130 mm long. A syringe pump is used to circulate a water flow seeded with 2 µm silver coated fused silica particles within the micro-channel. The digital inline holographic imaging set-up (as described in

the previous section) is used to image the biofilm and the moving particles above it in 3D. In addition to hologram SNR enhancement, the biofilm is removed from the corresponding reconstructed 3D optical fields of the holographic recordings, to achieve higher SNR in near-biofilm region resulting particle detection in close vicinity of the biofilm (Figure 4.3b).

The particle extraction, multi-pass 3D tracking and out-of-plane displacement refinement algorithms are applied in sequence to the holograms to calculate the corresponding 3D velocity fields. The iso-surface of the minimum value of the resolvable vorticity magnitude, based on our minimum velocimetry resolution (vector spacing) and minimum resolvable displacement (i.e. 75 µm and 1 pixel, respectively), is employed to visualize the 3D extent of the biofilm. Therefore, as Figure 4.4 shows, both the instantaneous 3D flow field and the 3D extent of the biofilm are simultaneously characterized for this biofilmed micro-channel in time.

4.3 DNS Turbulent Channel Flow

Synthetic tracer field in a turbulent channel flow is constructed using the DNS database from Johns Hopkins University (Li *et al.* 2008 and Graham *et al.* 2015). Specifically, an initial tracer field is generated with concentration of 2200 particles/mm^3 uniformly spaced within a 512×512×1024 µm^3 volume of interest. Then the generated tracer field is advected using the 3D velocity field extracted from the DNS channel flow database to produce consecutive tracer fields in time. Based on a similar approach used in the previous section, the corresponding synthetic holograms are generated from these tracer fields, simulating red light illumination and 1 µm/pixel resolution for particles of 2 µm in diameter. Subsequently, the tracer fields are extracted through our IIPE algorithm with more than 97% extraction rate and less than 3 µm positioning error for successively simulated holograms. Following the procedure explained in Case #1, the unstructured 3D velocity fields are computed for every two successively recorded holograms. The 3D displacement fields from the exact (DNS) and measured (DIH-PTV) are presented in Figure 4.5. Evidently, the DIH-PTV results demonstrate a good replication of the exact 3D velocity field from DNS. The displacement uncertainty defined similar to the positioning error δ, i.e. maximum error for 95% of extracted vectors, is < 8% in magnitude.

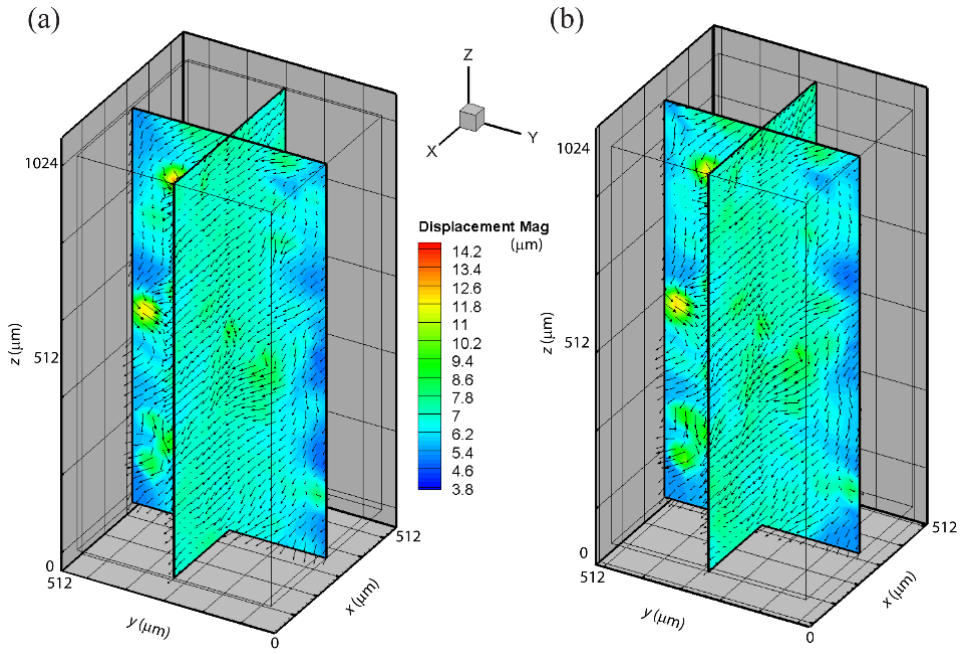

Figure 4.5: (a) A sample of instantaneous 3D displacement vector field from JHU-DNS database superimposed with its displacement magnitude contour, (b) corresponding 3D displacement vector field calculated through our DIH-PTV similarly superimposed with its displacement magnitude contour.

4.4 Turbulent Channel Flow

The SNR of interference patterns captured on particle holograms for in-line holography is inversely related to tracer concentrations and the longitudinal length of sampling volumes. This imposes a significant challenge on the implementation of DIH-PTV for wall-bounded turbulent flow measurements, where the flow domain/channel size is at least in the order of a few centimeters. As reviewed in Chapter 2, this has been tackled through local seeding (Sheng *et al.* 2008 and Talapatra and Katz 2013), i.e. introduction of the tracer particles immediately upstream of the sampling volume. The local seeding method limits the scattering depth within the sampling volume without sacrificing the spatial resolution (i.e. particle spacing), which enables DIH-PTV measurements to achieve the best velocity spatial resolution for wall-bounded turbulent flows. For example, velocity spatial resolution of 51 μm × 136 μm × 17 μm for smooth-wall DIH-PTV measurements (Sheng *et al.* 2008) using a single camera compared to 0.69 mm for Tomographic PIV with four cameras (Zhang *et al.* 2015). However, the DIH-PTV measurements have been restricted to much smaller sampling volumes (a few mm^3) compared with those of tomographic PIV and defocusing PIV. Accordingly, the scales of resolvable flow structures are limited to the

extent of a small seeded region. In addition, the local seeding yields some intrinsic challenges including the difficulty of maintaining consistent and sufficient tracer concentration in the sampling volume, especially over surfaces with prominent roughness features. These limitations prevent this technique from being widely used for turbulent wall-bounded flow measurements.

Our novel DIH-PTV method (presented in Chapter 3) minimizes the aforementioned challenges enabling application of DIH-PTV to both high-resolution near-wall flow measurement (local seeding) and the whole-channel measurement with whole-field seeding (i.e. sampling volume covers the entire depth of the channel). In this section, we present the applications of our improved DIH-PTV method for turbulent channel flow measurements under both near-wall and whole-channel (large sampling volume) settings. Specifically, in the first case, high-resolution near-wall measurements are performed through local seeding and using a 10X microscopic objective lens for imaging. In the second case, the measurement field is extended to the whole-channel width using whole-field seeding (i.e. seeding the entire flow facility) and a 1X imaging lens with velocity resolution and sampling volume size comparable to other 3D PIV techniques.

4.4.1 Experimental Facility

A refractive-index-matched (RIM) turbulent channel flow facility is designed and manufactured (Figure 4.6) for this study. This flow facility has a test section of 1.2 m long acrylic channel of square cross section (50 mm × 50 mm), which is equipped with three 25 cm long replaceable windows equally spaced at the upstream, mid-section and the downstream of the channel. The upstream and the mid-section windows are designed to provide incoming flow manipulations. The downstream window is the measurement region, which can be replaced with plates of different roughness elements for rough-wall channel flow measurements. Optical refractive index matching method using sodium iodide water solution is employed for rough-wall measurements in order to reduce the imaging aberrations at the working fluid-roughness plate interface. To achieve higher quality particle images, the flow loop is equipped with two inline filters of dual gradient density spun polypropylene carriages (25 micron pre-filter; 1 micron post-filter) to remove undissolved NaI salt crystals and other debris from the working fluid. In the experiments presented in this study, the sodium iodide solution of 40 % by weight with refractive index

of n =1.41 is employed as the working fluid, since the roughness samples are fabricated from PDMS (e.g. *Dow Corning Sylgard* 184).

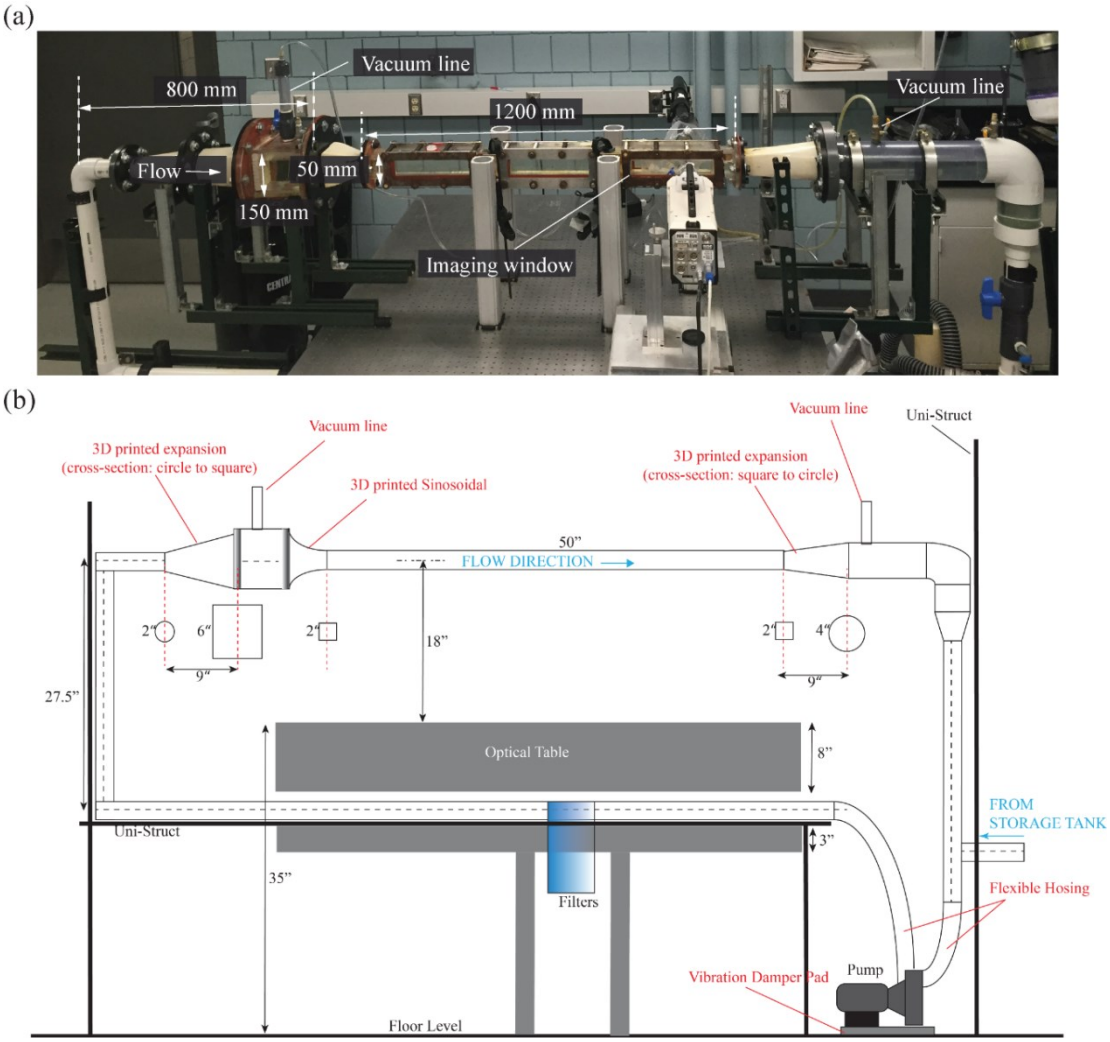

Figure 4.6: (a) A photograph and (b) a schematic of the refractive-index-matched flow facility operated with sodium iodide solution.

As Figure 4.6b shows, the incoming flow passes through a 3D printed expansion nuzzle with less than seven degrees of expansion angle, which minimizes the flow separation possibility. This nozzle supplies the fluid to a settling chamber that is connected to the vacuum line from the top to remove the floating bubbles from the working fluid. After passing through two sets of honeycombs, flow converges into the acrylic test section via a nozzle of sinusoidal profile. It is noteworthy that the settling chamber has a height offset of ~ 1 cm with these nuzzles on top, which decelerates the fluid at the top layer to augment

the bubble removal process. The flow is driven using a frequency controlled 0.5 *hp* centrifugal pump (*Dayton*), which enables operating of the facility with a wide range of Reynolds numbers (based on the width and centerline velocity of the channel) ranging from Re_h = 20000 to 60000. To reduce the vibration noise in our imaging system, the pump is isolated from the rest of the facility as well as the ground using flexible hosing and flexible padding, respectively. The flow facility is operated at Re_h = 22770, corresponding to the centerline velocity of U_c = 0.45 ms^{-1} for both experiments presented in this chapter.

4.4.2 DIH-PTV for near-wall measurements of a smooth-wall channel flow (local seeding)

A microscopic DIH-PTV set-up complemented with a local particle injection system (schematic is shown in Figure 4.7a) is employed to quantify near-wall 3D velocity fields of a smooth-wall turbulent channel flow. This high resolution DIH imaging system consists of an NAC Memrecam HX-5 high-speed camera equipped with a 10X EO-M-Plan infinity-corrected microscopic objective lens (NA = 0.45), and a 12 mW HeNe laser (λ = 632 nm). The focus plane of the camera is placed at the inner wall of the channel. Holograms are recorded on 1024×1024 pixel sensor at 6000 frames/s with 1 μm/pixel resolution from the channel flow locally seeded with 2 μm silver-coated silica particles. The local seeding is introduced through a set of ten holes of 200 μm in diameter, situated ~300 hole diameters upstream of the sampling volume to ensure that the seeding causes minimum disturbance to the flow. The sampling volume is located ~1 m from the inlet of the test section, and has the volume of 1.0 × 1.5 × 1.0 mm^3 (streamwise × wall-normal × spanwise) starting from ~100 μm away from the wall.

We use our DIH-PTV processing algorithms to calculate the instantaneous 3D velocity fields, with 100 μm spatial velocity resolution (vector spacing), from the corresponding holographic recordings. A sample of these 3D instantaneous velocity fields is presented in Figure 4.7b. The results demonstrate the capability of our DIH-PTV method for resolving the drastic change of velocity magnitude in the near-wall region of the wall-bounded turbulent flows. In addition, the high resolution DIH-PTV enables us to resolve coherent structures of a few hundred μm size within the inner layer of the turbulent flow profile (Figure 4.7c).

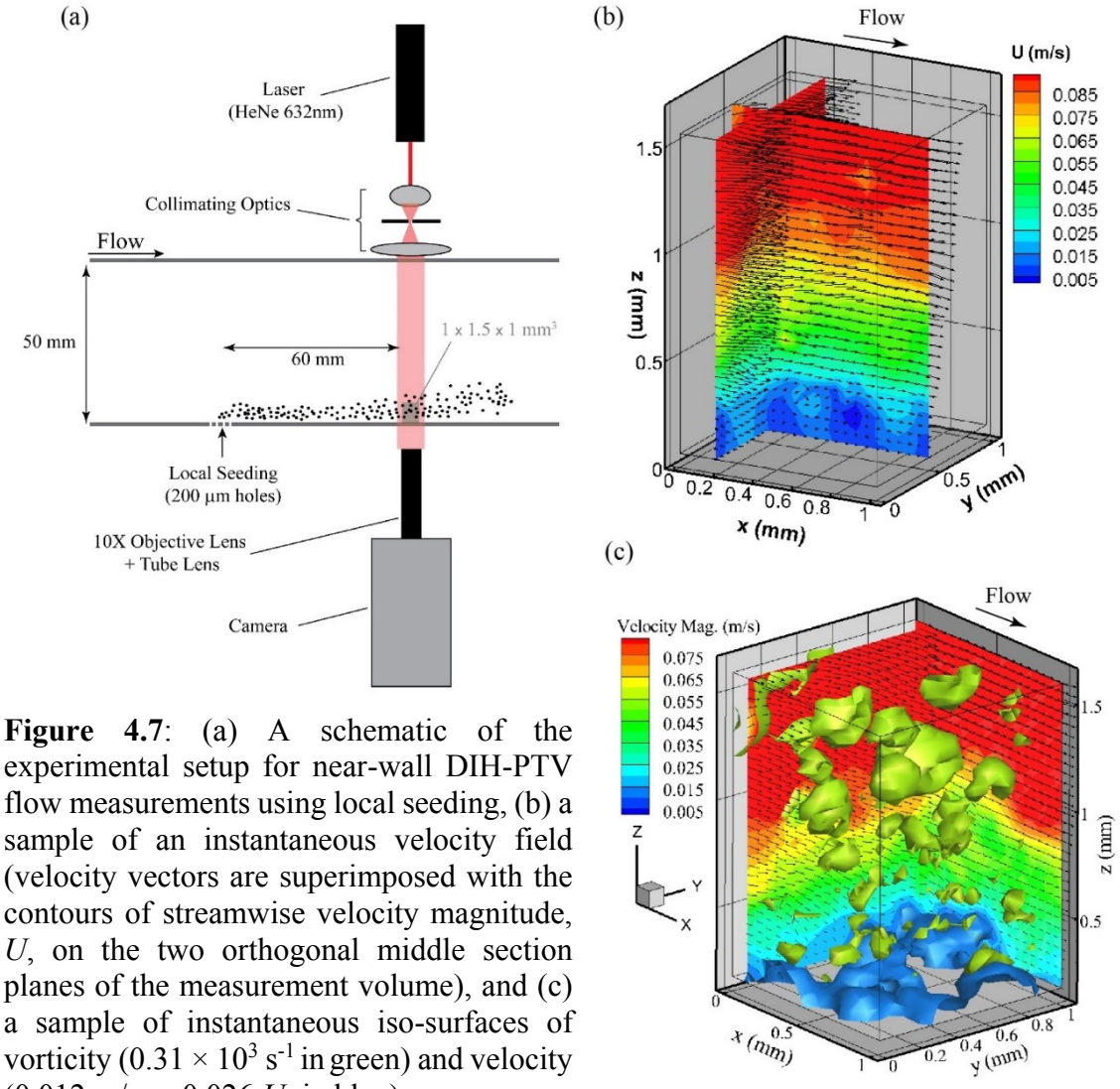

Figure 4.7: (a) A schematic of the experimental setup for near-wall DIH-PTV flow measurements using local seeding, (b) a sample of an instantaneous velocity field (velocity vectors are superimposed with the contours of streamwise velocity magnitude, U, on the two orthogonal middle section planes of the measurement volume), and (c) a sample of instantaneous iso-surfaces of vorticity (0.31×10^3 s^{-1} in green) and velocity (0.012 m/s or 0.026 U_c in blue).

4.4.3 DIH-PTV for whole-channel measurements of a smooth-wall channel flow (volumetric seeding)

In this experiment, we use a low magnification DIH-PTV imaging system to capture 3D flow fields over the entire depth of the channel. The flow facility is entirely seeded with silver-coated hollow glass spheres of 8-10 µm in diameter as tracer particles. The sampling volume is placed ~ 1 m downstream of the test section inlet. The high-speed camera (NAC Memrecam HX-5) for this experiment is equipped with a Nikon lens (Nikon 105mm f/2.8G), which is adjusted to 1:1 magnification (Figure 4.8a). The corresponding holograms of 1472 × 1448 pixels are recorded at 3080 frame/s with 10 µm/pixel resolution, resulting in a sampling volume of 14.7 × 50.0 × 14.4 mm^3. A sample

of holographic recordings before and after hologram SNR enhancement is presented in Figure 4.8b and c.

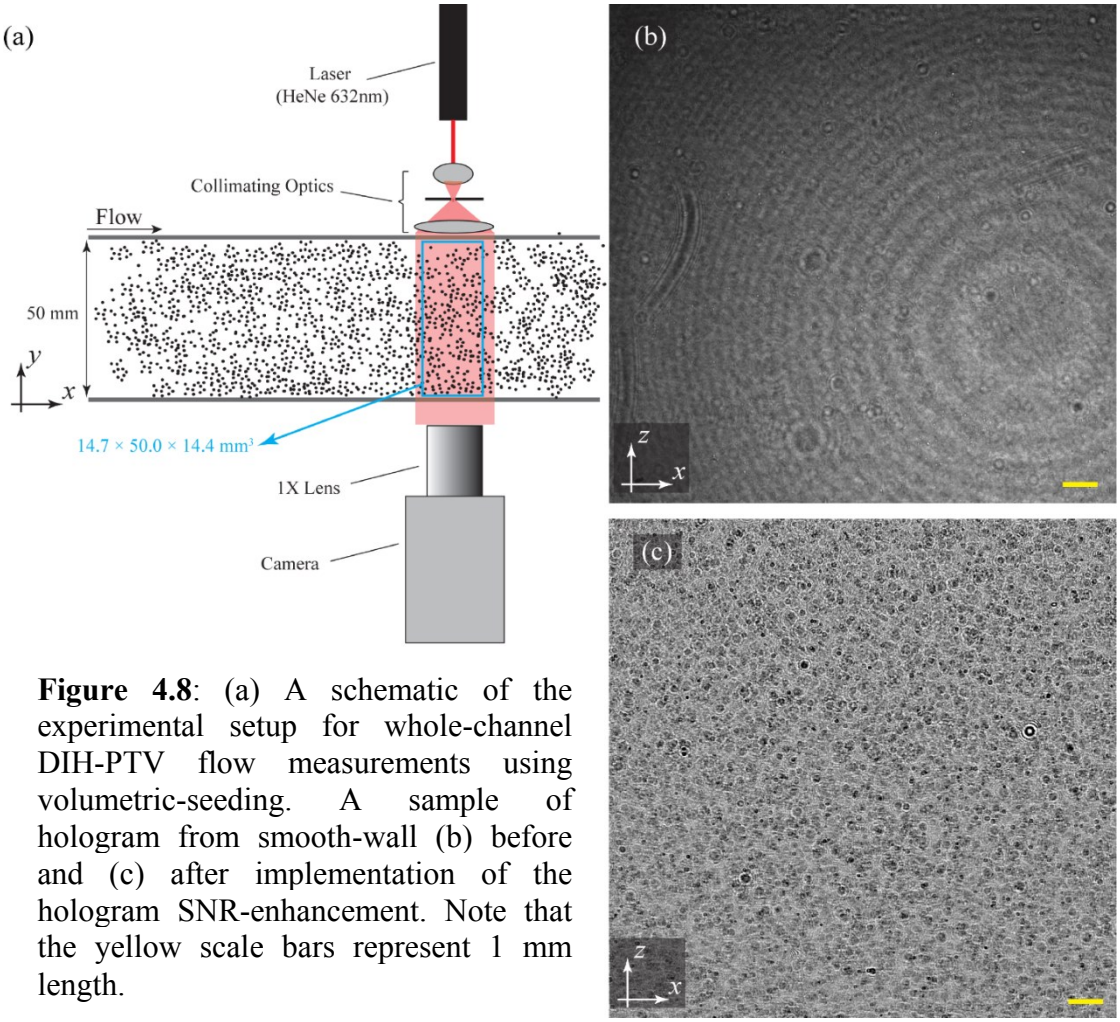

Figure 4.8: (a) A schematic of the experimental setup for whole-channel DIH-PTV flow measurements using volumetric-seeding. A sample of hologram from smooth-wall (b) before and (c) after implementation of the hologram SNR-enhancement. Note that the yellow scale bars represent 1 mm length.

Our DIH-PTV particle extraction (with five IIPE iterations) allows almost 70% increase in the valid particle extraction rate for these holograms of large sampling volumes. Note that this value is higher than previously reported value (i.e. ~40%) for microfluidic applications. Each pair of successively recorded holograms results in 3500-4000 valid tracks, which corresponds to ~ 1.3 mm velocity spatial resolution (vector spacing) in 3D. We implemented our DIH-PTV algorithm on a Linux machine containing an Intel Core i5-4690S processor at 3.20 GHz, 16 GB of RAM, and an Nvidia GeForce GTX-970 GPU. The processing time for generating a 3D vector field from a pair of successively recorded holograms (conducting the entire process illustrated in Figure 3.3) is less than 20 minutes.

The unstructured 3D velocity fields resulted from the multi-pass 3D tracking algorithm are finally interpolated onto a structure grid. The interpolation algorithm is developed based on Taylor series and using least-square technique proposed by Talapatra and Katz (2013). Notably, the interpolation is only applied within a longitudinal band of the unstructured velocity fields containing adequate number of velocity vectors (more than 80 unstructured vectors per slab). The histogram of vector distribution within the unstructured 3D velocity fields (resulted from 3D tracking) for the holographic recordings is used to identify this band. The average numbers of velocity vectors in each 1.25 mm long longitudinal slabs of the sampling volume for more than 750 statistically independent vector fields spanning >18 seconds of smooth-wall DIH-PTV recordings are presented in Figure 4.9. Therefore, to achieve consistent velocity resolution (~ equal vector spacing within the sampling volume), the interpolation for the current dataset is performed only within the band of 1 mm < y < 49 mm.

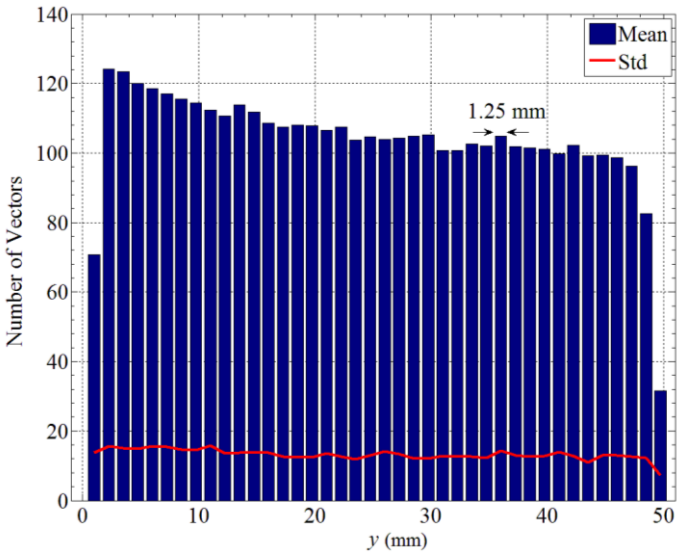

Figure 4.9: The distribution of tracked velocity vectors in longitudinal 1.25 mm slabs within > 18 seconds of DIH-PTV recordings from smooth-wall channel flow.

A sample of structured instantaneous velocity fields is presented in Figure 4.10a, which shows the capability of DIH-PTV in capturing the variation of velocity within the entire depth of the channel. In Figure 4.10b and c, the consecutive snapshots from the time series of velocity vector volumes are superimposed by the iso-surfaces of vorticity and low speed velocity magnitudes in green and blue, respectively. As they show, both coherent structures associated with the low-speed streaks in near-wall regions and those of the outer layer

region are detected.

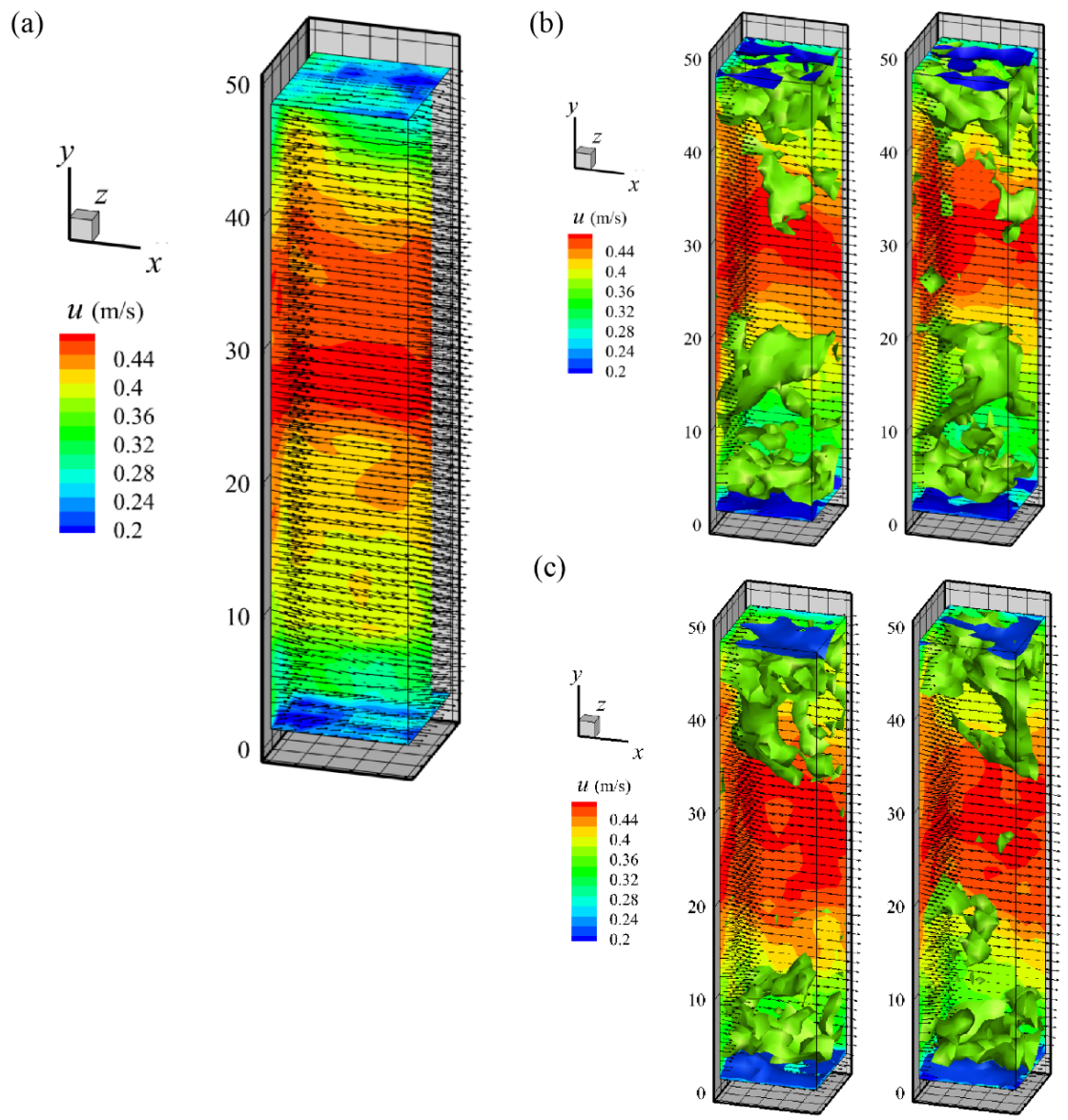

Figure 4.10: (a) A sample of instantaneous 3D velocity field (velocity vectors are superimposed with the contours of streamwise velocity magnitude on the orthogonal planes within the measurement volume). (b) The corresponding iso-surfaces of velocity magnitude of 0.3 U_c (blue) and vorticity of 1.5 U_{max}/δ (green) illustrating low-speed regions above top and bottom walls and the associated large-scale vortex structures, respectively.

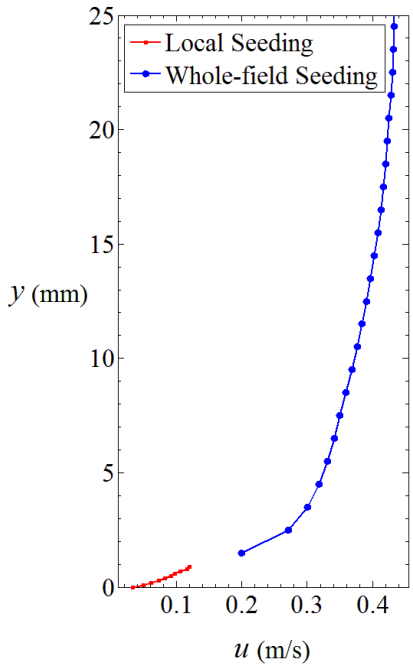

Figure 4.11: The measured mean velocity profiles using: (a) high resolution near-wall DIH-PTV using local seeding set-up and (b) low-magnification whole-channel DIH-PIV using whole-field seeding method.

In this study, a time-resolved digital in-line holographic PTV is employed in two different settings (i.e. high resolution near-wall and low magnification whole-channel) to investigate the near-wall and whole-channel turbulent flow structures as well as turbulent statistics. Notably, the sampling volume size of the near-wall microscopic DIH-PTV matches the vector spacing (i.e. the resolution) of the low-magnification DIH-PTV where the sampling volume is extended to the entire depth of the channel. This highlights the potential capability of our DIH-PTV to resolve the entire velocity profile, i.e. within both near-wall and outer-layer regions, as well as flow structures in a wide range of scales. To illustrate this capability, the 3D average velocity fields are calculated for both measurement volumes using 750 and 300 instantaneous velocity field samples spanning ~18.5 and 5 seconds of recordings, respectively. The ensemble averaged velocity profiles for both measurements are presented in Figure 4.11. The plot shows a continuous increase of velocity as y (wall-normal) increases, i.e. closer to the core of the channel flow (from 1.5 mm to 25 mm), and the slower moving boundary layer regions in close vicinity of the wall (from 100 µm to 900 µm). The offset between two measurements volumes covers a region

of 0.9 mm to 1.5 mm away from the wall, and this explains ~ >0.07 m/s difference between the minimum value of velocity measured by whole-field DIH-PTV and the maximum measured by high resolution near-wall DIH-PTV.

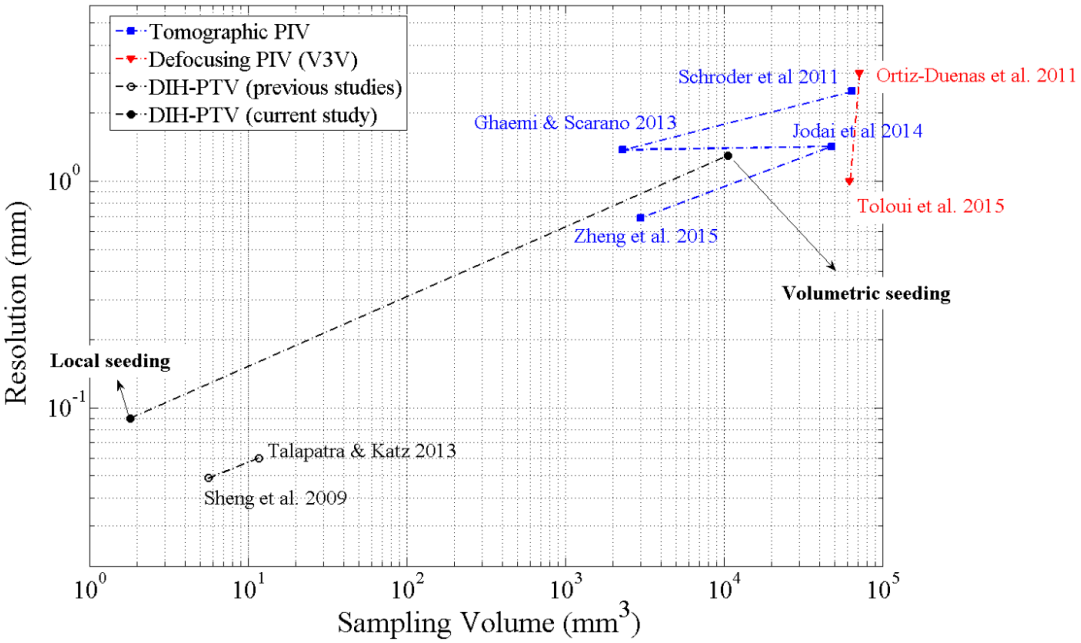

Figure 4.12: A comparison of 3D whole-field flow measurement techniques used for wall-bounded turbulent flows based on their sampling volume and spatial resolution.

4.5 Summary and Discussion

The accuracy and applicability of the proposed DIH-PTV method for microchannel flows is evaluated. Specifically, the measured instantaneous velocity fields from a laminar flow micro-channel matches the analytical Poiseuille profile with less than 5% difference. In the case of wall-bounded turbulent flow measurements, first, the accuracy of 3D velocity measurement is validated using synthetic holograms replicating a DNS turbulent channel flow dataset. The results show less than 0.2 D_p in magnitude difference between the measured 3D turbulent flows from our method and the corresponding exact solutions. Finally, DIH-PTV technique is implemented for turbulent channel flow measurements under both near-wall (sampling volume of 1.0 × 1.5 × 1.0 mm^3 , streamwise × wall-normal × spanwise , with <100 μm vector spacing) and whole-channel (sampling volume of 14.7 × 50 × 14.4 mm^3 with ~1.3 mm vector spacing) settings in our turbulent channel flow facility. Notably the sampling volume size of the near-wall microscopic DIH-PTV matches

the vector spacing (i.e. the resolution) of the low-magnification whole-channel DIH-PTV where the sampling volume is extended to the entire depth of the channel. This highlights the potential capability of our DIH-PTV to resolve flow structures in a wide range of scales.

Figure 4.12 compares the sampling volume and spatial resolution for different 3D whole-field turbulent flow measurement techniques. Note that the Figure 4.12 is only intended to provide a ballpark comparison of the sampling volume and the resolution since it does not take into account of the variation of camera sensor sizes that are used for these measurements. As the figure shows, DIH-PTV using local seeding provides an unmatchable velocity spatial resolution, although it is restricted to smaller sampling volume near wall. On the other hand, other 3D whole-field measurement techniques (e.g. tomographic PIV and defocusing PIV) are only capable of quantifying relatively large-scale flow motions of turbulent boundary layer with limited resolution near the surface. Here, our current study extends the application of DIH-PTV for large sampling volumes in smooth-wall turbulent flows with spatial resolution comparable to other 3D flow measurement techniques. Overall, the presented DIH-PTV measurements under two different settings highlight the potential of DIH-PTV to obtain 3D characterization of the turbulent structures over a full range of scales, covering both the near wall region and the out-layer of wall-bounded turbulent flows.

Chapter 5: Experimental Investigation of Turbulent Channel Flow using DIH-PTV: Rough-wall vs. Smooth-wall

5.1 Introduction

The effect of surface roughness on mass, heat and momentum transport mechanisms in wall-bounded turbulent flows is of substantial interest in a variety of engineering applications. These applications range from internal flows in oil and gas pipelines (e.g. Allen *et al.* 2007) to the atmospheric boundary layer (e.g. Morris *et al.* 2007), from heat transfer in heat exchangers (e.g. Park *et al.* 2004) to cooling of electronics (e.g. Avelino *et al.* 2004) and finally from drag reduction to self-cleaning or anti-biofouling effects of biological surfaces (e.g. Walsh 1984, Oeffnerand Lauder2012 and Bixler and Bhushan 2012).

Flack and Schultz (2014) reviewed the findings of their 15 years consecutive experimental research on rough-wall-bounded turbulent flows. As they mentioned, attempts on understanding the effects of surface roughness on wall-bounded turbulent flows started over 80 years ago, where Nikuradse (1933) conducted pressure drop measurement in pipes with uniformly coated sand surfaces. Later in 1954 (Clauser 1954 and Hama 1954), roughness function (ΔU^+) was introduced as the first metric to characterize the effect of different surface roughness geometries on wall-bounded turbulent flows. In 1976, Townsend introduced his similarity hypothesis, which assumes the roughness effect on the outer layer is only on a mean momentum deficit and the impact of roughness is confined to the inner layer (Townsend 1976). This hypothesis, i.e. assuming the roughness sublayer only affects a few roughness heights from the wall, has become the core of rough-wall turbulent flow modeling algorithms. However, some studies reported roughness types where this theory was invalid (Flack *et al.* 2007). For example, Krogstad and Antonia (1999) performed Pitot tube and hot-wire measurements on a smooth-wall and two different rough-walls, where they observed the effect of roughness on turbulent Reynolds stresses penetrated far beyond the wall region. Moreover, in a wind tunnel experiment Keirsbulck *et al.* (2002) performed PIV over a *k*-type rough-wall of square cross-section elements. Their results show that the wake strength of the mean velocity

depends on wall-roughness, which implies that the effect of surface roughness might extend to the outer region. In addition, recently, based on refractive-index-matching (RIM) technique, Hong *et al.* (2011 and 2012) have examined the turbulent flow structures within and above the roughness sublayer over a rough wall composed of pyramidal roughness elements using high resolution 2D PIV. They reported that the roughness elements generate unique coherent structures which can significantly alter the turbulent energy transport across a wide range of scales within and above the inner layer. Therefore, a better understanding of the near-wall turbulence and its interactions with the outer layer is necessary in order to obtain a comprehensive assessment on the wall similarity theorem. Nevertheless, the sharp gradient of refractive index in near-wall region distorts or even blocks the illumination and results in measurement voids, making non-invasive near-wall flow measurements (e.g. LDV and PIV) an extremely challenging task. In addition, the flow field above 3D roughness elements show high level of three-dimensionality that imposes certain issues to application of simple planar PIV measurements of turbulent flows in near-rough-wall regions. In an effort to overcome these technical issues, Talapatra *et al.* (2013) employed a 3D microscopic holographic PTV using local seeding within a refractive index matched rough-wall channel of pyramidal roughness elements. Although, through minimizing the interface aberrations by RIM they could resolve super small scale flow structures induced by the roughness elements in near-wall region, their measurement volume was confined to a small region within and slightly above the roughness sublayer which limits their access to flow characteristics in the outer layer.

In order to overcome these limitations, we conducted a series of time-resolved digital inline holographic PTV measurements within the entire depth of our refractive index-matched turbulent channel flow facility under both rough- and smooth-wall conditions. The experiments were carried out under the same experimental conditions, and the coherent structures and turbulent statistics are presented and compared between rough- and smooth-wall cases.

5.2 Experimental set-up and Data Processing

The experiments are conducted at different time within an optically index-matched turbulent flow facility. The measurement windows of smooth- and rough-wall samples are placed ~ 1 m downstream from the inlet section of a 1.2 m long acrylic channel of 50 mm

square cross section (more details on the flow facility in Section 4.4.1). The roughness sample is a 200 mm (length) × 50 mm (width) stretch of tapered cylindrical elements of 0.35 mm in diameter, 1.5 mm in height (k) and center-to-center spacing of 2 mm in an aligned layout (Figure 5.1a). The roughness plate is made out of Polydimethylsiloxane (PDMS) polymer (Dow Corning Sylgard 184 at the mixing ratio of 1:10). Refractive index matching (RIM) technique using NaI aqueous solution (40% by weight and n =1.41) is used to minimize the optical aberration at the roughness-fluid interface and achieve optical access through the roughness sample (See Figure 5.1b).

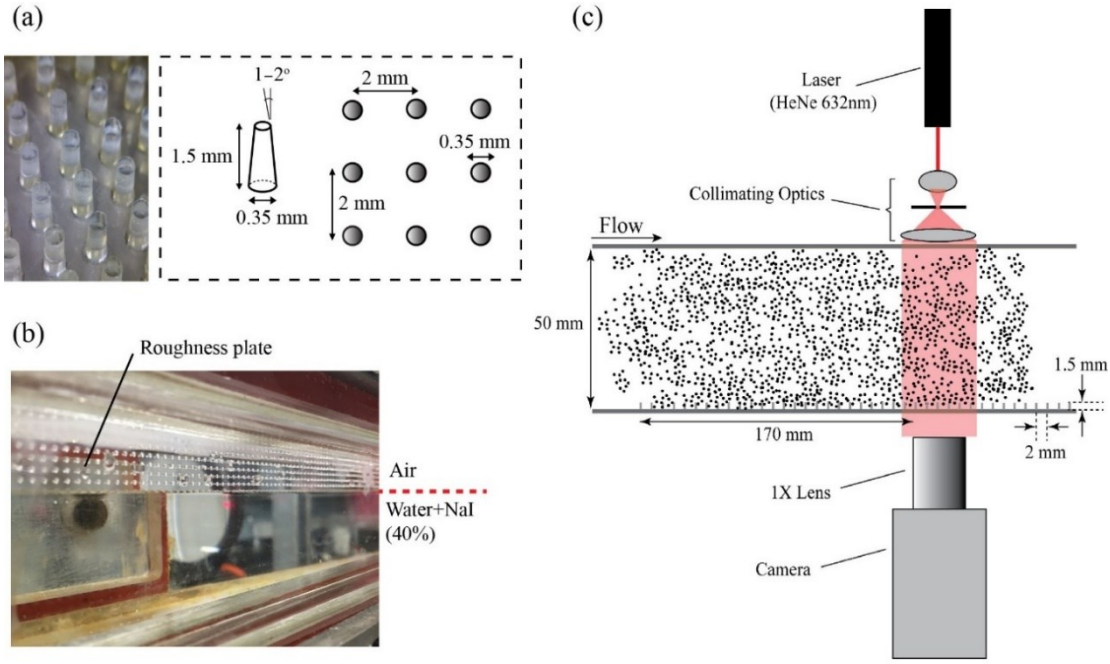

Figure 5.1: (a) A close-up view of the PDMS cylindrical roughness elements and a schematic presenting its geometric configuration, (b) a photograph of the half-filled test section demonstrating the index matching of PDMS rough-surface composed of an array of tapered cylinders and (c) the schematic of DIH-PTV setup.

The experiments are performed at $Re_H = U_c \times h/\nu \approx 22770$, where U_c, h, and ν represent centerline velocity, channel width and the kinematic viscosity of the working fluid, respectively. DIH-PTV was employed for time-resolved 3D flow field measurements covering the entire depth of the channel within a sampling volume of 14.7 × 50.0 × 14.4 mm^3. The entire channel facility is seeded with silver-coated hollow glass spheres of D_p = 8–10 μm in diameter as tracer particles. The DIH-PTV optical set-up is presented in Figure 5.1c. As it shows, the set-up includes a 12 mW HeNe laser (λ = 632 nm) as the light source, a spatial filter (including a 20X objective and a 20 μm pin-hole), and a collimator lens

generating a collimated coherent laser beam of 5 cm in diameter. The interference pattern of the tracer particles' forward scattering with the reference light forms particle holograms on the sensor plane of a high-speed camera (NAC Memrecam HX-5). The camera is focused on the inner surface of the channel-wall, and is equipped with a Nikon lens (Nikon 105mm f/2.8G) which is adjusted to 1:1 magnification. The corresponding holograms of 1472 × 1448 pixels are recorded at 3080 frame/s with 10 μm/pixel resolution. The recordings include seven time-resolved datasets each contain >16000 images and recorded with 20 minutes separation (time required for data transfer from onboard memory of the camera to the computer) from each other. To achieve statistically independent velocity samples, these holographic recordings are subsampled every 0.5 sec to small statistically independent time-series containing 21 holograms (i.e. 20 velocity vector fields).

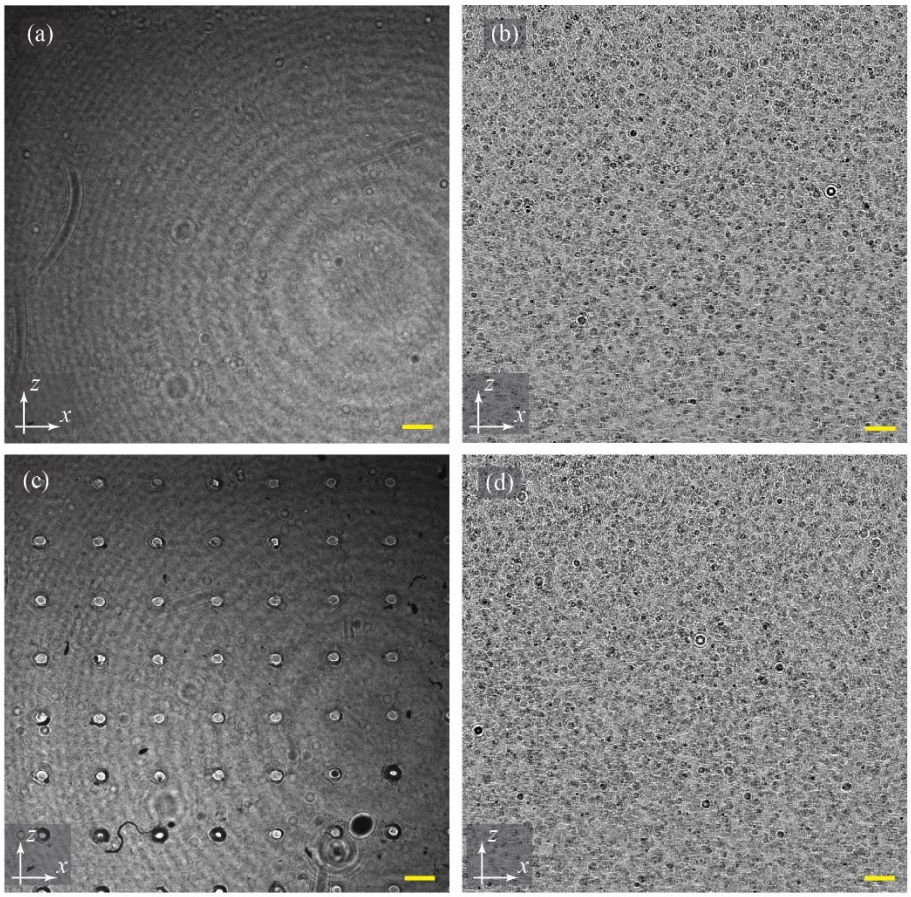

Figure 5.2: Samples of holographic recordings for (a,b) smooth-wall, (c,d) rough-wall experiments before and after hologram SNR-enhancement implementation. Note that the yellow scale bars represent 1 mm length.

Samples of holographic recordings before and after hologram SNR enhancement are presented in Figure 5.2a and 5.2b, which highlights the effectiveness of both RIM and SNR-enhancement in obtaining high SNR particle fringe patterns from high seeding density particle holograms. The SNR-enhanced holograms are then fed into our GPU accelerated DIH-PTV processing algorithm (Figure 3.3) including the steps of 3D deconvolution, automatic thresholding and 3D segmentation, iterative inverse particle extraction (IIPE), multi-pass 3D tracking and cross-correlation based displacement refinement. Each pair of successively recorded holograms yields 3500-4000 valid tracks, which results in ~ 1.3 mm velocity spatial resolution (vector spacing) in 3D. The uncertainty of the displacement measurement is less than 0.5 D_p for the lateral components (streamwise u and spanwise w) and around D_p in the longitudinal direction (wall-normal v). Notably, due to the limitations on 3D tracking for such highly concentrated particle fields the sampling rate of the holographic recoding is adjusted to achieve lateral displacements of 4−16 pixels, which corresponds to longitudinal displacements of 4−16 μm (assuming $v \sim 10\%$ of u). This longitudinal displacement range is comparable to the uncertainty band of longitudinal displacement detection of our algorithm for these size of tracers (i.e. $D_p = 10$ μm). In addition, memory limitation restricts our scanning resolution to ~ 61 μm in longitudinal direction (i.e. 1024 longitudinal scans for 1472 × 1448 pixels holograms).

5.3 Results

5.1.1 Turbulent statistics

Mean velocity: The 3D average velocity fields are calculated using 750 realizations of instantaneous velocity fields for each of the smooth- and rough-wall measurements. The ensemble averaged 3D velocity fields for both experiments are presented in Figure 5.3. These velocity fields span the entire depth of the channel (within a sampling volume of 14.7 × 50.0 × 14.4 mm^3). Therefore, a continuous increase of velocity is evident in both measurements as y (wall-normal) increases from the slower moving boundary layer regions (blue), on top and bottom walls, towards the core (red) of the channel. Notably, the presence of the roughness plate of cylindrical elements at the bottom wall (i.e. $y = 0$) of the channel breaks the symmetry of the velocity field and the corresponding profile for the rough-wall case compared to the smooth-wall case. This also expands the extent of the low momentum

layer in the vicinity of the bottom wall of the channel (representing the wake of cylindrical roughness elements) compared to the smooth-wall case.

The wall-bounded turbulent flows over smooth surfaces have been characterized into two principal regions of near-wall (viscous-dominated region) and outer-layer (where viscosity effect is negligible). It has shown that a logarithmic profile represents the mean velocity profile in the overlapping region of the inner and outer layers, which can be presented as the following composite velocity profile:

$$U^+ = \kappa^{-1} \log (y^+) + \beta \qquad (5\text{-}1)$$

The y^+ is the wall-normal distance from the wall and U^+ represents the streamwise velocity, which are normalized with the inner layer length and velocity scales (i.e. ν/u_τ and u_τ, where ν is the kinematic viscosity and u_τ is the friction velocity), respectively. The κ and β are the Karman constants (0.41 and 5.2) and are believed to be universal. In the case of rough-wall turbulent flows, the presence of surface roughness alters the mean velocity profile in near-wall region and consequently the resultant friction drag. Nevertheless, the logarithmic velocity distribution for the mean velocity profile could still be used in the wall layer, with the same values of the Karman constants as over smooth walls (Jimenez 2004). To account for roughness effect, a roughness function (ΔU^+) is added to the logarithmic equation as

$$U^+ = \kappa^{-1} \log (y^+) + \beta - \Delta U^+ \qquad (5\text{-}2)$$

The roughness function accounts for the wall-normal shift of the mean velocity profile caused by the flow resistance induced by the wall roughness (Marchis and Napoli 2012).

The non-dimensional mean velocity profiles for both experiments (i.e. smooth- and rough-wall) are presented in a semi-log plot in Figure 5.3d. The y^+ is measured from the same wall-normal plane (i.e. the inner surface of the channel), whose location is obtained from manually examining the corresponding 3D reconstructed optical field, for both cases. The wall units and friction velocities are calculated through a logarithmic fit to the mean streamwise velocity profiles measured by DIH-PTV (within the range of y = 1 mm to 6 mm from the wall). The friction velocities are calculated to be 0.022 m/s and 0.049 m/s corresponding to wall units of ~45 μm and ~21 μm and time scales of τ^+ = 2.3 ms and τ^+ = 0.5 ms for the smooth- and rough-wall experiments. As Figure 5.3d shows, both

cases have a well-defined logarithmic regions. Notably, the velocity profile in the rough-wall case is negatively shifted (as expected) by a roughness function of 13.28 U^+.

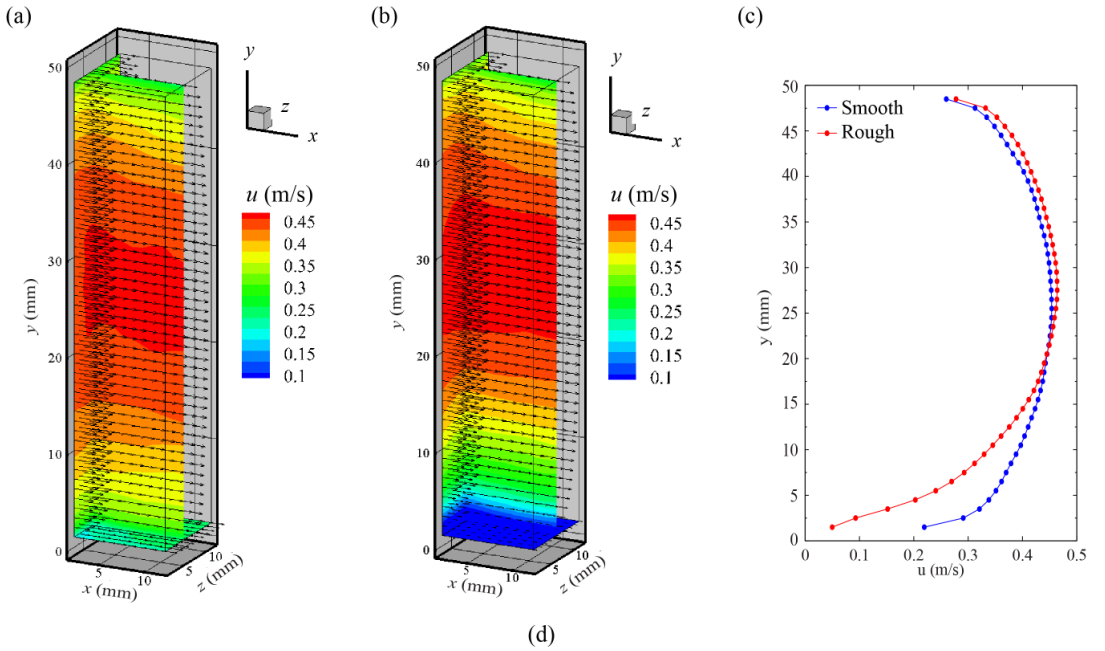

Figure 5.3: The measured mean velocity vector fields superimposed with the contours of streamwise velocity magnitude on three orthogonal planes of the measurement volume for: (a) smooth-wall and (b) rough-wall experiments. The corresponding mean velocity profiles on (c) a linear plot and (d) a semi-log plot representations.

To evaluate the quality of both measurements and the logarithmic fits, the calculated roughness function is compared to those of some other rough-wall studies in the literature. Specifically, the roughness function values for our experiment and a collection of seven other rough-wall studies are plotted against their corresponding values of δ/k (the ratio of the boundary layer thickness to the roughness height) in Figure 5.4. As it shows, the roughness function calculated for our experiment sits nicely within the general trend of ΔU^+ variation for different ratios of δ/k.

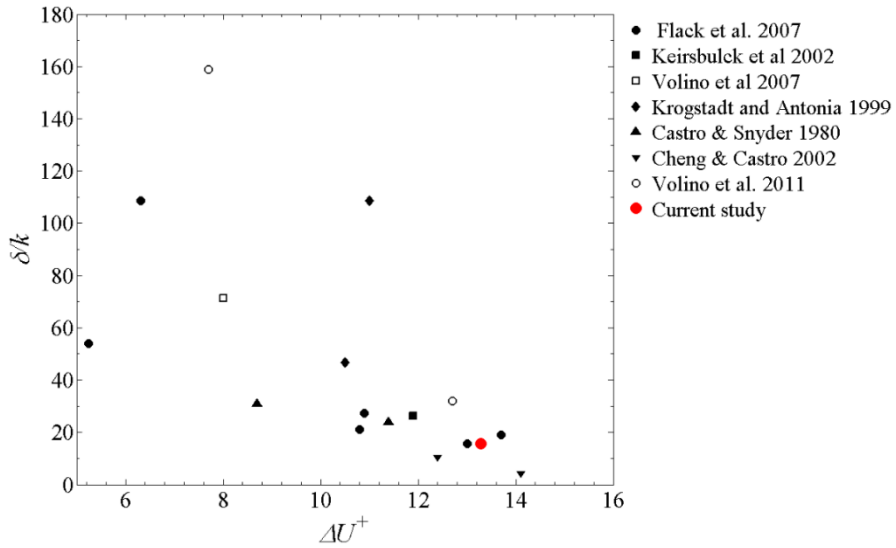

Figure 5.4: A comparison of ΔU^+ versus δ/k for a collection of rough-wall studies.

Turbulent kinetic energy: Turbulent kinetic energy (TKE) as a higher order turbulent statistic is calculated for both smooth- and rough-wall cases (see Figure 5.5) to obtain a better quantitative understanding of the roughness effects on our turbulent channel flow. The TKE profiles for both cases start at 1.25 mm or 0.05δ distance from the wall, where δ represents the turbulent boundary layer thickness or the half-width of the channel.

In Figure 5.5d, the TKE values are normalized with the corresponding values of u_τ^2. The trend of TKE variation for smooth-wall matches those of reported in the literature (e.g. Lee *et al.* 2011), and the peak of the TKE profile is most likely located beyond the reach of our current measurement, i.e. closer to the wall than our first data point ($y < 0.05\delta$). This peak for the rough-wall case appears around the wall-normal distance of $0.22\delta - 0.26\delta$ from the wall. Notably, the Reynolds stresses and consequently the TKE profiles for 3D rough-walls have been reported to reach a maximum peak around $0.05\delta - 0.1\delta$ and reduce as y increases (e.g. Lee *et al.* 2011 for 3D rough-wall of cubical elements and Hong *et al.* 2011 for pyramidal 3D roughness). This difference can be probably attributed to considerably higher ratio of k/δ, i.e. taller roughness elements respect to the half channel-width height, in our experiments ($k = 0.06\delta$) compared to other ones (e.g. $k = 0.018\delta$ in Hong *et al.* 2011). This consequently results in a thicker roughness sublayer (i.e. $3k - 5k = 0.18\delta - 0.3\delta$) and does not satisfy the well-characterized condition of rough-wall proposed by Jimenez (2004), i.e. $\delta/k \geq 50$.

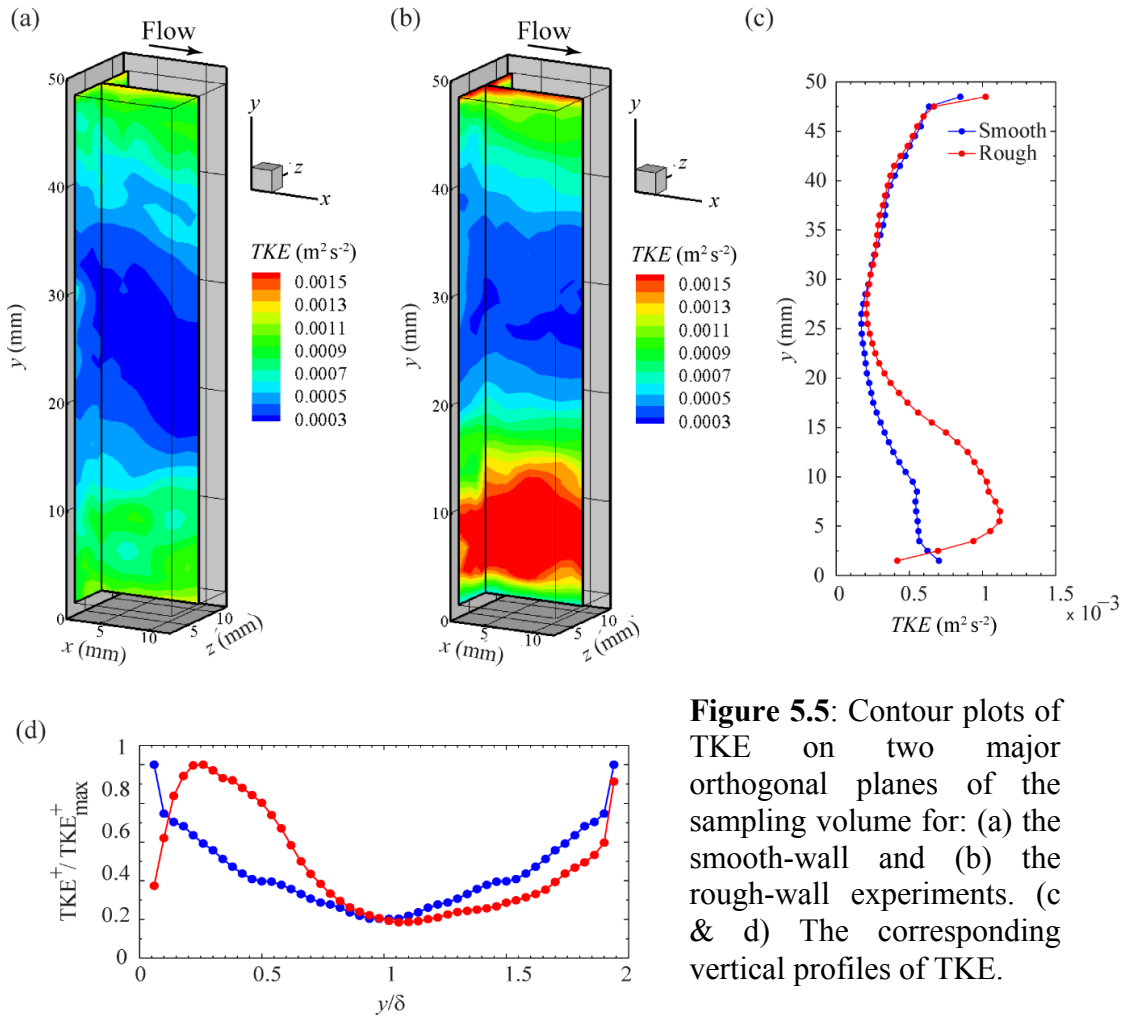

Figure 5.5: Contour plots of TKE on two major orthogonal planes of the sampling volume for: (a) the smooth-wall and (b) the rough-wall experiments. (c & d) The corresponding vertical profiles of TKE.

5.1.2 Instantaneous 3D velocity vector fields and coherent flow structures

In addition to 750 statistically independent velocity fields that are used to calculate the turbulent statistics, 300 time-resolved velocity fields are computed for each case to observe the evolution and distribution of the velocity fields and the coherent structures in time. The velocity fluctuations (u', v', w') are also calculated by subtracting the instantaneous velocity fields from the corresponding time-average velocity field (Figure 5.3a and b). Some samples of these instantaneous velocity fields and the normalized velocity fluctuation fields (u'/u_τ, v'/u_τ , w'/u_τ) for both cases (i.e. smooth and rough) are presented in Figure 5.6 and Figure 5.7, respectively. The iso-surface of vorticity ($\vec{\omega} = \nabla \times \vec{V}$) is employed to visualize the distribution and evolution of turbulent coherent vortical structures in time (e.g. see Figure 5.6). The blue iso-surface represents regions of low

streamwise velocity (0.3 U_{max}) and the green iso-surface indicates the vorticity magnitude of 1.5 U_{max}/δ. In both cases, the variation of velocity within the channel including slow moving streaks in near-wall region as well as the high-speed core of the channel are captured. Of note in the rough-wall case is the extension of low-speed region up to >3 mm $\approx 2k$. On smooth sides of the channel (i.e. both walls in smooth- and top wall for rough-wall cases) elongated vortical structures growing towards the outer layer with an inclination angle are observed. These vortex packet structures are significantly disturbed by the surface roughness presence over the bottom wall of the rough-wall case.

To visualize the effect of cylindrical roughness elements on near-wall streaky structures, the contour plots of streamwise velocity fluctuations at three different elevations from the wall (i.e. $y = k$, 3.6 k and 6.3 k) are examined. A couple of snapshots of these contour plots are presented in Figure 5.6 for both smooth- and rough-wall cases. The contours are normalized by the corresponding friction velocity in each case, and the blue and red contours indicate the low and high values of u'. Elongated low and high speed neighboring streaks are evident in the smooth-wall case, while these structures are broken down into smaller sizes and meander through the cylindrical roughness elements in the rough-wall case. In addition, the visualized spacing between these low-speed streaks are ~150 y^+ on the plane of $y^+ = 27$ in the smooth-wall case, which is in a good agreement with the values reported by experimental study of Smith & Metzler (1983) and DNS analysis of *Kim et al.* (1997) for Re_τ of a similar range.

To further investigate the size of these structures by a quantitative measure, the two-point correlation in space is applied to streamwise velocity fluctuations on $y = 0.06\ \delta$ planes. The results are presented in Figure 5.8. The two point correlation results show shorter streamwise extent of R_{uu} for the rough-wall compared to the smooth-wall (Figure 5.7), which is consistent with our visualizations. Notably, the rough- and smooth-wall results of R_{uu} become considerably similar after $y > 6k$ (not shown for brevity), indicating the extent of the roughness sublayer.

Notably, the extent of the coherent structures for the rough-wall case calculated from R_{uu} contour plot is limited to 0.08δ, which matches the spanwise spacing of cylindrical roughness elements (i.e. 2 mm).

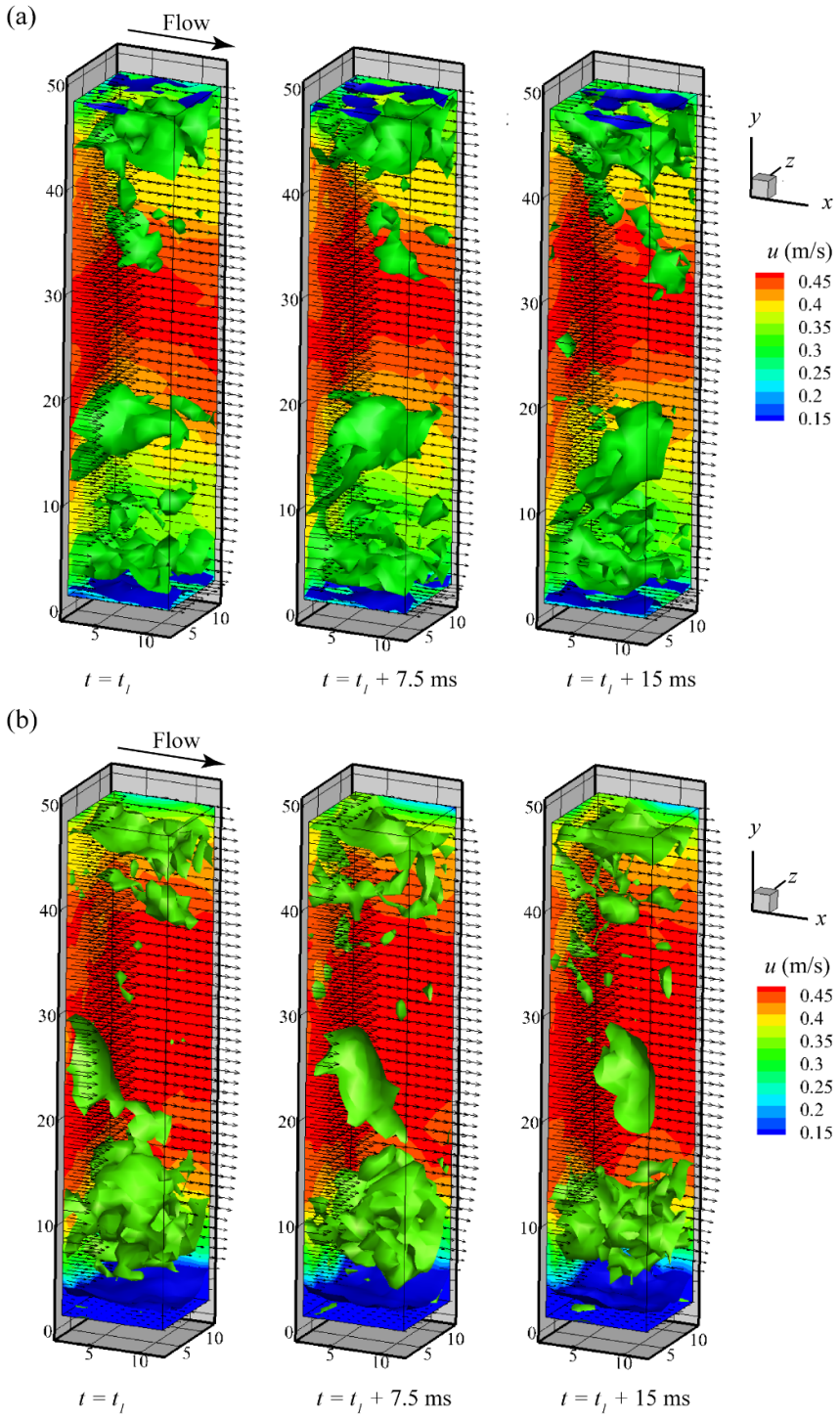

Figure 5.6: Sample of three consecutive instantaneous velocity fields and their corresponding coherent structure distributions for: (a) the smooth-wall and (b) the rough-wall cases. Note that the velocity vectors are superimposed with the contours of streamwise velocity magnitude on three orthogonal planes within the measurement volumes.

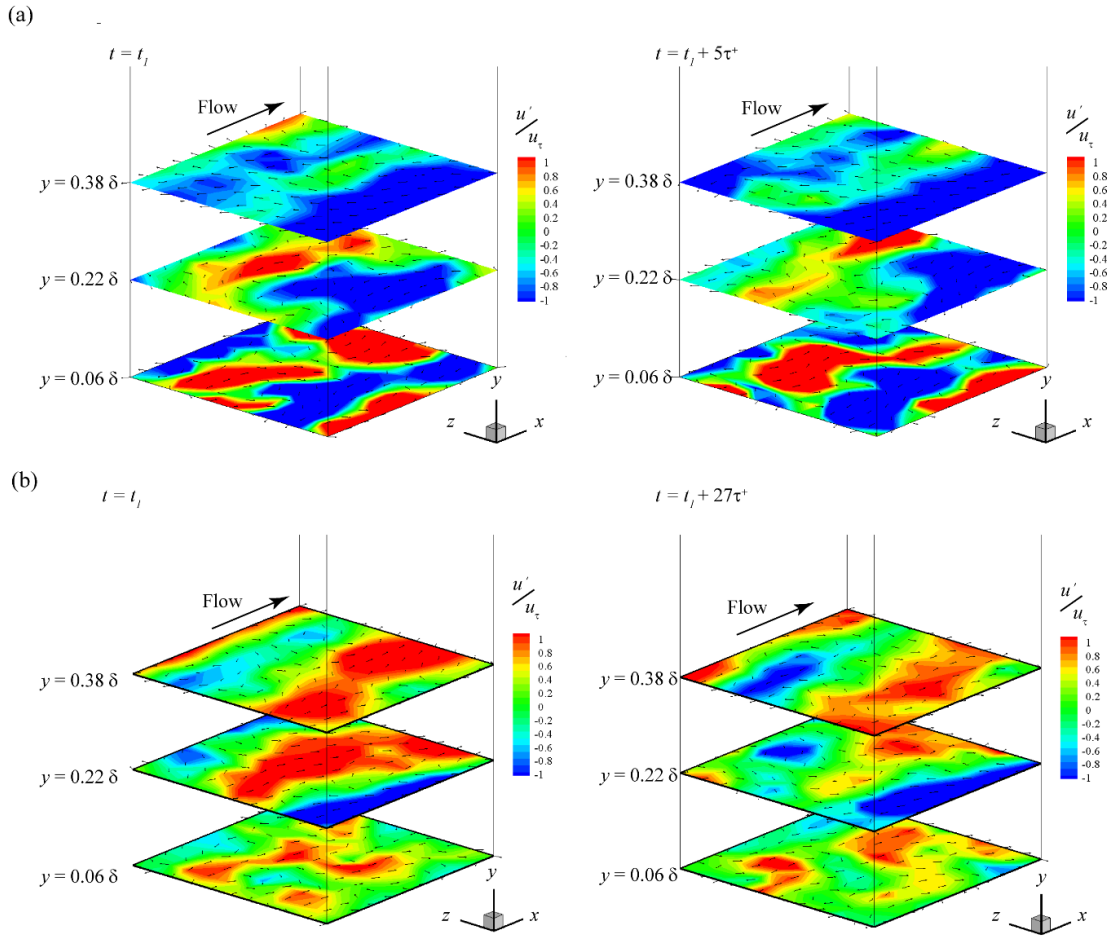

Figure 5.7: Contour plots of u'/u_τ on three wall-normal (i.e. x-z) planes of y = 0.06 δ, 0.22 δ and 0.38 δ for two successive realizations with ~ 12 ms separation in time for: (a) the smooth-wall and (b) the rough-wall experiments.

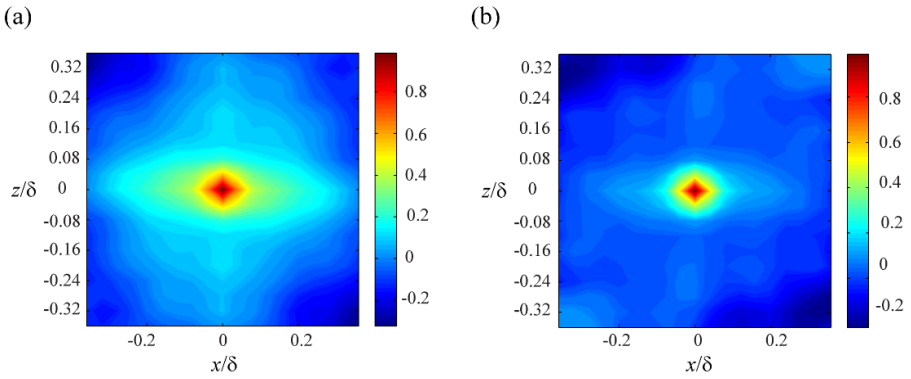

Figure 5.8: Contour plots of two-point correlations of the streamwise velocity fluctuations (i.e. R_{uu}) on wall-normal plane of y = 0.06 δ for: (a) the smooth-wall and (b) the rough-wall experiments.

5.4 Summary and Conclusion

Utilizing optical index matching turbulent channel flow, time-resolved DIH-PTV is applied to investigate both instantaneous velocity fields and turbulent statistics of wall-bounded turbulent channel flows over rough- and smooth-wall surfaces. The channel was operated at bulk Reynolds number of Re = 23000 and $Re_\tau \approx 540$ and 1220 for smooth- and rough-wall cases, respectively. Implementing DIH-PTV with 1:1 imaging magnification allows velocity measurements within a sampling volume of $14.7 \times 50 \times 14.4$ mm^3 and with <1.3 mm vector spacing, which covers the entire depth of the channel. Analyzing sufficient number of statistically independent samples, the turbulence statistics for rough-wall boundary layers are evaluated as follows: (1) the roughness function representing the wall-normal shift of the mean velocity profile is calculated to be 13.28, which matches with the general trend from the collection of other rough-wall studies (i.e. Figure 5.4); (2) as a representative of higher order turbulent statistic, TKE profiles for both cases of rough- and smooth-wall cases follow the expected variation trend reported by other studies.

The 3D extent of the wake formed by cylindrical elements can be clearly visualized from both the instantaneous and the average 3D velocity fields. The vortical coherent structures are captured and visualized in time-resolved measurements of both rough- and smooth-wall. One-sided hairpin legs are observed in the smooth-wall velocity fields in near both bottom and top walls of the channel, although they are absent or suppressed in size in the rough-wall velocity fields. This may be attributed to the presence of the surface roughness that restructures the near-wall flow structures (e.g. accentuating the turbulent structures of its own size). In addition, the characteristics (i.e. size and spacing) of near-wall low-speed streaks for both cases are visualized in spatial distribution of streamwise velocity fluctuations in time, which shows comparatively smaller structures for rough-wall case. This observations are confirmed through computation of corresponding two-point correlations. Overall, the presented measurements and results highlight the capability of DIH-PTV to obtain 3D characterization of the turbulent structures for rough- and smooth-wall-bounded turbulent flows.

Chapter 6: Summary and Future Work

6.1 Summary

The current study aimed to introduce a series of novel holographic particle reconstruction and displacement calculation methods (illustrated in Figure 3.3) to minimize the challenges associated with conventional DIH-PTV and make this technique a mature technique for 3D flow measurements. Specifically, to increase longitudinal resolution of DIH, we enrich the holographic processing algorithms with a 3D deconvolution technique, which results in 3–5 folds reduction in the DOF of tracer particles based on several experimental cases. To minimize human intervention and enable automatic particle extraction, an automatic 3D local SNR enhancement and thresholding for 3D segmentation is developed. To maximize high fidelity particle extraction for concentrated tracer particle holograms and extend the application of DIH-PTV to sampling volume with longer in-depth lengths, an inverse iterative particle extraction (IIPE) algorithm is introduced that increases the number of detectable tracers 30–70%. These particle reconstruction/extraction algorithms complemented with our displacement calculation algorithms including a multi-pass 3D tracking method and a cross-correlation based longitudinal displacement refinement scheme. Finally, the entire DIH processing is accelerated using graphics processing units (GPUs), which reduces the computation time required for DIH processing. The DIH-PTV method is validated using experimental and synthetic holographic data. For the experimental case, the instantaneous velocity profiles measured from laminar water flow within a micro-channel are validated against the analytical solution (Poiseuille velocity profile) with less than 5% difference in magnitude. In addition, the resulted velocity fields from the DIH-PTV method applied to synthetic holographic data, replicating direct numerical simulation (DNS) of turbulent channel flow, demonstrate reproduction of the exact 3D velocity fields with <8% error for >95% of calculated vectors.

In addition, the proposed DIH-PTV method has been successfully applied to measure instantaneous 3D velocity fields in a wide range of applications from micro-fluidics to turbulent channel flows. Specifically, the applicability of the technique is validated using the experiment of laminar flow in a microchannel and the synthetic tracer flow fields generated using a DNS turbulent channel flow database. In addition, the proposed method

is applied to both smooth-wall and rough-wall turbulent channel flow measurements under two different settings of high-resolution near-wall and the whole-channel measurement (i.e. sampling volume covers the entire depth of the channel). In the first case, using microscopic objective and local seeding, DIH-PTV resolves near-wall flow structures within a sampling volume of $1 \times 1.5 \times 1$ mm^3 (streamwise × wall-normal × spanwise) with velocity resolution of ~100 μm/vector. In the second case, the measurement volume is extended to the whole-channel depth by seeding the entire channel. Under this setting, the 3D velocity fields are obtained within a sampling volume of $14.7 \times 50.0 \times 14.4$ mm^3 with a velocity resolution of ~1.3 mm/vector, comparable to other the-state-of-the-art 3D whole-field flow measurement techniques. Overall, the presented DIH-PTV measurements under two different settings highlight the potential of DIH-PTV to obtain 3D characterization of the turbulent structures over a full range of scales, covering both the near wall region and the out-layer of wall-bounded turbulent flows.

6.2 Future Work

Towards zero longitudinal uncertainty

Despite all these improvements and significant reduction of longitudinal localization and displacement uncertainties, the longitudinal uncertainty, mainly for cases of turbulent channel flow measurements via whole-field seeding, still remains a challenging issue. In order to further reduce this uncertainty and make DIH-PTV a more reliable 3D measurement technique for wall-bounded turbulent flows, we are working on a double-view DIH-PTV method with an easy and robust auto-calibration scheme. Holographic recording with multiple cameras imaging the same sampling volume from different angles (e.g. orthogonal) has so far been the most robust solution to minimize this DOF issue (e.g. Soria and Atkinson 2008). However, its previous implementations have suffered from a number of limitations such as: (1) low concentration of extractable particles; and (2) a cumbersome calibration process. Since our current processing algorithms for DIH-PTV proved a great capability in minimizing the limitations on both seeding density and sampling volume size (e.g. > 4000 valid tracks within a $14.7 \times 50.0 \times 14.4$ mm^3 for macro-scale and >3000 valid tracks within a $1 \times 1 \times 1$ mm^3 micro-scale flow experiments), the only remaining issue to extend its application to double-view DIH-PTV is development of

an easy calibration process. Below, the preliminary design, methodology and approach for this project are presented.

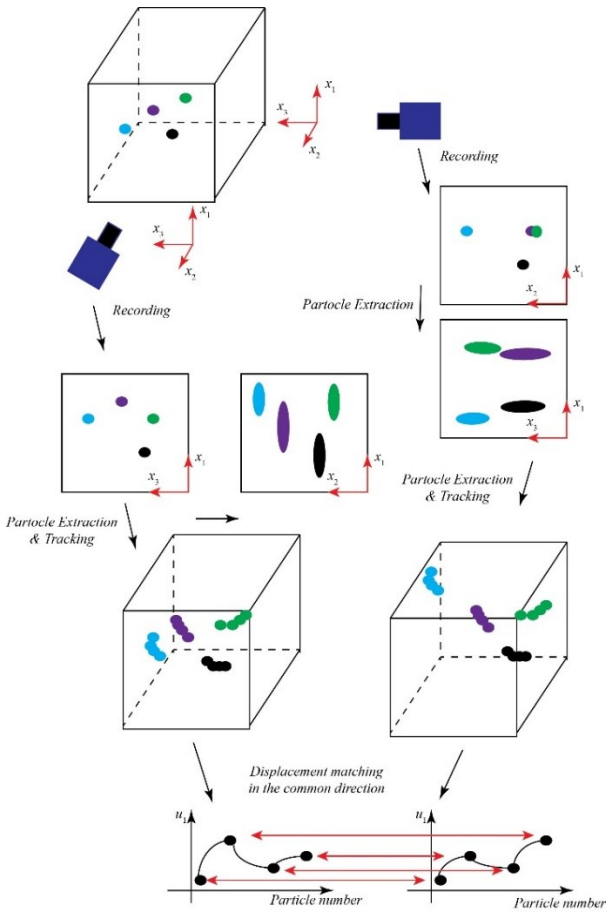

Figure 6.1: The schematic shows the preliminary idea of auto-calibration for double-view DIH-PTV.

To simplify the calibration step, first, the working fluid within test section will be filtered from tracer objects or debris. Then, a low concentration particle solution will be added to the working fluid in the test section. The particle extraction will be applied to the holograms and through tracking the corresponding 3D displacement fields will be calculated. The projection of calculated displacement vectors on the common direction of both views (i.e. x_1 in Figure 6.1) will be extracted as a 1D signal. This signal will be used as a characteristic of the particle to match the particle images and calculate the offset between two views. In the next step, the overall 3D segmented optical fields are superimposed voxel by voxel, i.e. each voxel will be assigned to the maximum (1 or white) intensity value of the corresponding voxels from two reconstructed optical fields. A search

block of size DOF is centered at the centroid of the particles extracted from each hologram to find the nearest possible crossing shape of every two orthogonal blobs.

Bibliography

- Adhikari, D., Gemmell, B.J., Hallberg, M.P., Longmire, E.K. and Buskey, E.J., 2015. Simultaneous measurement of 3D zooplankton trajectories and surrounding fluid velocity field in complex flows. *Journal of Experimental Biology*, *218*(22), pp.3534-3540.
- Adrian, R.J., 1991. Particle-imaging techniques for experimental fluid mechanics. *Annual review of fluid mechanics*, *23*(1), pp.261-304.
- Agard, D.A., 1984. Optical sectioning microscopy: cellular architecture in three dimensions. *Annual review of biophysics and bioengineering*, *13*(1), pp.191-219.
- Allano, D., Malek, M., Walle, F., Corbin, F., Godard, G., Coëtmellec, S., Lecordier, B., Foucaut, J.M. and Lebrun, D., 2013. Three-dimensional velocity near-wall measurements by digital in-line holography: calibration and results. *Applied optics*, *52*(1), pp.A9-A17.
- Allen, J.J., Shockling, M.A., Kunkel, G.J. and Smits, A.J., 2007. Turbulent flow in smooth and rough pipes. *Philosophical Transactions of the Royal Society of London A: Mathematical, Physical and Engineering Sciences*,*365*(1852), pp.699-714.
- Avelino, M., dos Anjos, G.R. and Kakaç, S., 2004. Turbulent Forced Convection Air Cooling of Electronics. In *10th Brazilian Congress of Thermal Engineering and Sciences*.
- Barnhart, D.H., Adrian, R.J. and Papen, G.C., 1994. Phase-conjugate holographic system for high-resolution particle-image velocimetry. *Applied Optics*, *33*(30), pp.7159-7170.
- Beals, M.J., Fugal, J.P., Shaw, R.A., Lu, J., Spuler, S.M. and Stith, J.L., 2015. Holographic measurements of inhomogeneous cloud mixing at the centimeter scale. *Science*, *350*(6256), pp.87-90.
- Brücker, C., 1992. Dreidimensionale quantitative Vermessung des Wirbelaufplatzens mit der Particle Tracking Velocimetry (PTV) kombiniert mit Lichtschnitt-Scanning. *DGLR BERICHT*, pp.445-445.
- Brücker, C., 1997. 3D scanning PIV applied to an air flow in a motored engine using digital high-speed video. *Measurement Science and Technology*, *8*(12), p.1480.
- Bruun, H.H., 1996. Hot-wire anemometry: principles and signal analysis.
- Burns, N. and Watson, J., 2007, June. Data extraction from underwater holograms of marine organisms. In *OCEANS 2007-Europe* (pp. 1-6). IEEE.
- Cao, L., Pan, G., de Jong, J., Woodward, S. and Meng, H., 2008. Hybrid digital holographic imaging system for three-dimensional dense particle field measurement. *Applied optics*, *47*(25), pp.4501-4508.

- Cheng, Y., Torregrosa, M.M., Villegas, A. and Diez, F.J., 2011. Time Resolved Scanning PIV measurements at fine scales in a turbulent jet.*International Journal of Heat and Fluid Flow*, *32*(3), pp.708-718.
- Chamorro, L.P., Troolin, D.R., Lee, S.J., Arndt, R.E.A. and Sotiropoulos, F., 2013. Three-dimensional flow visualization in the wake of a miniature axial-flow hydrokinetic turbine. *Experiments in fluids*, *54*(2), pp.1-12.
- Cheng, H. and Castro, I. P. 2002 Near-wall flow over urban-type roughness. Boundary-Layer Meteorol. 104, 229–259.
- Crocker, J.C. and Grier, D.G., 1996. Methods of digital video microscopy for colloidal studies. *Journal of colloid and interface science*, *179*(1), pp.298-310.
- De Marchis, M. and Napoli, E., 2012. Effects of irregular two-dimensional and three-dimensional surface roughness in turbulent channel flows. *International Journal of Heat and Fluid Flow*, *36*, pp.7-17.
- Dixon, L., Cheong, F.C. and Grier, D.G., 2011. Holographic deconvolution microscopy for high-resolution particle tracking. *Optics express*, *19*(17), pp.16410-16417.
- Elsinga, G.E., Scarano, F., Wieneke, B. and van Oudheusden, B.W., 2006. Tomographic particle image velocimetry. *Experiments in fluids*, *41*(6), pp.933-947.
- Elsinga, G.E., 2008. *Tomographic particle image velocimetry and its application to turbulent boundary layers* (Doctoral dissertation, TU Delft, Delft University of Technology).
- Elsinga, G.E., 2013, July. Complete removal of ghost particles in Tomographic-PIV. In *PIV13; 10th International Symposium on Particle Image Velocimetry, Delft, The Netherlands, July 1-3, 2013*. Delft University of Technology, Faculty of Mechanical, Maritime and Materials Engineering, and Faculty of Aerospace Engineering.
- Flack, K. A., Schultz, M. P. and Connelly, J. S., 2007. Examination of a critical roughness height for boundary layer similarity," Phys. Fluids 19, 095104
- Flack, K.A. and Schultz, M.P., 2014. Roughness effects on wall-bounded turbulent flowsa). *Physics of Fluids (1994-present)*, *26*(10), p.101305.
- Flack, K.A., Schultz, M.P. and Connelly, J.S., 2007. Examination of a critical roughness height for outer layer similarity. *Physics of Fluids (1994-present)*,*19*(9), p.095104.
- Flammang, B.E., Lauder, G.V., Troolin, D.R. and Strand, T., 2011. Volumetric imaging of shark tail hydrodynamics reveals a three-dimensional dual-ring vortex wake structure. *Proceedings of the Royal Society of London B: Biological Sciences*, p.rspb20110489.
- Gao, J., 2014. *Development and applications of digital holography to particle field measurement and in vivo biological imaging* (Doctoral dissertation, PURDUE UNIVERSITY).

- Graham, J., Kanov, K., Yang, X.I.A., Lee, M., Malaya, N., Lalescu, C.C., Burns, R., Eyink, G., Szalay, A., Moser, R.D. and Meneveau, C., 2016. A Web services accessible database of turbulent channel flow and its use for testing a new integral wall model for LES. *Journal of Turbulence*, *17*(2), pp.181-215.
- Ghaemi, S. and Scarano, F., 2013. Turbulent structure of high-amplitude pressure peaks within the turbulent boundary layer. *Journal of Fluid Mechanics*, *735*, pp.381-426.
- Goodman, J., 1968, Introduction to Fourier Optics (McGraw-Hill).
- Hinsch, K.D. and Herrmann, S.F., 2004. Signal quality improvements by short-coherence holographic particle image velocimetry. *Measurement Science and Technology*, *15*(4), p.622.
- Graham, G.W. and Smith, W.M., 2010. The application of holography to the analysis of size and settling velocity of suspended cohesive sediments.*Limnology and Oceanography: Methods*, *8*(1), pp.1-15.
- Guildenbecher, D.R., Gao, J., Reu, P.L. and Chen, J., 2012, September. Digital holography reconstruction algorithms to estimate the morphology and depth of nonspherical absorbing particles. In *SPIE Optical Engineering+ Applications* (pp. 849303-849303). International Society for Optics and Photonics.
- Hong, J., Talapatra, S., Katz, J., Tester, P.A., Waggett, R.J. and Place, A.R., 2012. Algal toxins alter copepod feeding behavior. *PloS one*, *7*(5), p.e36845.
- Hong, J., Katz, J. and Schultz, M.P., 2011. Near-wall turbulence statistics and flow structures over three-dimensional roughness in a turbulent channel flow. *Journal of Fluid Mechanics*, *667*, pp.1-37.
- Hori, T. and Sakakibara, J., 2004. High-speed scanning stereoscopic PIV for 3D vorticity measurement in liquids. *Measurement Science and Technology*,*15*(6), p.1067.
- Hove, J.R., Köster, R.W., Forouhar, A.S., Acevedo-Bolton, G., Fraser, S.E. and Gharib, M., 2003. Intracardiac fluid forces are an essential epigenetic factor for embryonic cardiogenesis. *Nature*, *421*(6919), pp.172-177.
- Im, H., Castro, C.M., Shao, H., Liong, M., Song, J., Pathania, D., Fexon, L., Min, C., Avila-Wallace, M., Zurkiya, O. and Rho, J., 2015. Digital diffraction analysis enables low-cost molecular diagnostics on a smartphone.*Proceedings of the National Academy of Sciences*, *112*(18), pp.5613-5618.
- Jiménez, J., 2004. Turbulent flows over rough walls. *Annu. Rev. Fluid Mech.*,*36*, pp.173-196.
- Jodai Y, Westerweel J and Elsinga G E 2014 Time-resolved Tomographic-PIV measurement in the near-wall region of a turbulent boundary layer *17th international symposium on applications of laser techniques to fluid mechanic*s (Lisbon, Portugal).

- Kaikkonen, V.A., Ekimov, D. and Makynen, A.J., 2014. A holographic in-line imaging system for meteorological applications. *Instrumentation and Measurement, IEEE Transactions on*, *63*(5), pp.1137-1144.
- Katz, J. and Sheng, J., 2010. Applications of holography in fluid mechanics and particle dynamics. *Annual Review of Fluid Mechanics*, *42*, pp.531-555.
- Keirsbulck, L., Labraga, L., Mazouz, A. and Tournier, C., 2002. Surface roughness effects on turbulent boundary layer structures. Journal of fluids engineering, 124(1), pp.127-135.
- Kim, J., Moin, P. and Moser, R., 1987. Turbulence statistics in fully developed channel flow at low Reynolds number. *Journal of fluid mechanics*, *177*, pp.133-166.
- Krogstadt, P.Å. and Antonia, R.A., 1999. Surface roughness effects in turbulent boundary layers. *Experiments in Fluids*, *27*(5), pp.450-460.
- Lai W, Pan G, Menon R, Troolin D, Graff E, Gharib M and Pereira F 2008 Volumetric three-component velocimetry: a new tool for 3D flow measurement *14th international symposium on applications of laser techniques to fluid mechanic*s (Lisbon, Portugal)
- Latychevskaia, T., Gehri, F. and Fink, H.W., 2010. Depth-resolved holographic reconstructions by three-dimensional deconvolution. *Optics express*, *18*(21), pp.22527-22544.
- Latychevskaia, T. and Fink, H.W., 2014. Holographic time-resolved particle tracking by means of three-dimensional volumetric deconvolution. *Optics express*, *22*(17), pp.20994-21003.
- Lawson, J.M. and Dawson, J.R., 2014. A scanning PIV method for fine-scale turbulence measurements. *Experiments in Fluids*, *55*(12), pp.1-19.
- Le, T.B., Troolin, D.R., Amatya, D., Longmire, E.K. and Sotiropoulos, F., 2013. Vortex phenomena in sidewall aneurysm hemodynamics: experiment and numerical simulation. *Annals of biomedical engineering*, *41*(10), pp.2157-2170.
- Lee, J.H., Sung, H.J. and Krogstad, P.Å., 2011. Direct numerical simulation of the turbulent boundary layer over a cube-roughened wall. *Journal of Fluid Mechanics*, *669*, pp.397-431.
- Li, Y., Perlman, E., Wan, M., Yang, Y., Meneveau, C., Burns, R., Chen, S., Szalay, A. and Eyink, G., 2008. A public turbulence database cluster and applications to study Lagrangian evolution of velocity increments in turbulence. *Journal of Turbulence*, (9), p.N31.
- Lima, R., Wada, S., Tsubota, K.I. and Yamaguchi, T., 2006. Confocal micro-PIV measurements of three-dimensional profiles of cell suspension flow in a square microchannel. *Measurement Science and Technology*, *17*(4), p.797.

- Lindken, R., Westerweel, J. and Wieneke, B., 2006. Stereoscopic micro particle image velocimetry. *Experiments in Fluids*, *41*(2), pp.161-171.
- Liu, Y., Cheng, B., Barbera, G., Troolin, D.R. and Deng, X., 2013. Volumetric visualization of the near-and far-field wake in flapping wings. *Bioinspiration & biomimetics*, *8*(3), p.036010.
- Malek, M., Allano, D., Coëtmellec, S. and Lebrun, D., 2004. Digital in-line holography: influence of the shadow density on particle field extraction.*Optics Express*, *12*(10), pp.2270-2279.
- Meng, H., Pan, G., Pu, Y. and Woodward, S.H., 2004. Holographic particle image velocimetry: from film to digital recording. *Measurement Science and Technology*, *15*(4), p.673.
- Meng, H., Anderson, W.L., Hussain, F. and Liu, D.D., 1993. Intrinsic speckle noise in in-line particle holography. *JOSA A*, *10*(9), pp.2046-2058.
- Morris, S.C., Stolpa, S.R., Slaboch, P.E. and Klewicki, J.C., 2007. Near-surface particle image velocimetry measurements in a transitionally rough-wall atmospheric boundary layer. *Journal of Fluid Mechanics*, *580*, pp.319-338.
- Nezu, I. and Rodi, W., 1986. Open-channel flow measurements with a laser Doppler anemometer. *Journal of Hydraulic Engineering*, *112*(5), pp.335-355.
- Nikuradse, J., 1976, Laws of flow in rough pipes, NACA Technical Memorandum 1292, 1933
- Oeffner, J. and Lauder, G.V., 2012. The hydrodynamic function of shark skin and two biomimetic applications. *Journal of Experimental Biology*, *215*(5), pp.785-795.
- Olsen MG, Adrian RJ (2000a) Brownian motion and correlation in particle image velocimetry. Opt Laser Technol 32(7–8): 621–627.
- Olsen MG (2009) Directional dependence of depth of correlation due to in-plane fluid shear in microscopic particle image velocimetry. *Meas Sci Technol* 20(1):015402.1–015402.9
- Ortiz-Dueñas C, Ryan M D and Longmire E K 2011 Modification of turbulent boundary layer structure using immersed wall-mounted cylinders 7th *Turbulence and Shear Flow Phenomena VII* (Ottawa, Canada)
- Pan G and Meng H 2001 Digital in-line holographic PIV for 3D particulate flow diagnostics *4th international symposium on particle image velocimetry* (Goettingen, Germany)
- Park, K., Choi, D.H. and Lee, K.S., 2004. Optimum design of plate heat exchanger with staggered pin arrays. *Numerical Heat Transfer, Part A: Applications*, *45*(4), pp.347-361.
- Pereira, F. and Gharib, M., 2004. A method for three-dimensional particle sizing in two-phase flows. *Measurement Science and Technology*, *15*(10), p.2029.

- Pereira, F., Stüer, H., Graff, E.C. and Gharib, M., 2006. Two-frame 3D particle tracking. *Measurement science and technology*, *17*(7), p.1680.
- Poloczanska, E.S. and Butler, A.J., 2010. Biofouling and climate change.*Biofouling*, *333*.
- Pothos, S., Troolin, D., Lai, W. and Menon, R., 2009. V3V-Volumetric three-component velocimetry for 3D flow measurements main principle, theory and applications. *Revista Termotehnica*, *2*, p.2009.
- Pu Y; Meng H., 2000. An advanced off-axis holographic particle image velocimetry (HPIV) system. *Experiments in Fluids*, Vol 29, 184-197
- Raffel, M., Willert, C. and Kompenhans, J., 1998. Particle Image Velocimetry; A Particle Guide.
- Scarano, F., 2012. Tomographic PIV: principles and practice. *Measurement Science and Technology*, *24*(1), p.012001.
- Schröder, A., Geisler, R., Staack, K.É.A.A., Elsinga, G.E., Scarano, F., Wieneke, B., Henning, A., Poelma, C. and Westerweel, J., 2011. Eulerian and Lagrangian views of a turbulent boundary layer flow using time-resolved tomographic PIV. *Experiments in fluids*, *50*(4), pp.1071-1091.
- Seo, S., Su, T.W., Tseng, D.K., Erlinger, A. and Ozcan, A., 2009. Lensfree holographic imaging for on-chip cytometry and diagnostics. *Lab on a Chip*,*9*(6), pp.777-787.
- Sheng, J., Malkiel, E. and Katz, J., 2008. Using digital holographic microscopy for simultaneous measurements of 3D near wall velocity and wall shear stress in a turbulent boundary layer. *Experiments in fluids*, *45*(6), pp.1023-1035.
- Sheng, J., Malkiel, E. and Katz, J., 2006. Digital holographic microscope for measuring three-dimensional particle distributions and motions. *Applied optics*, *45*(16), pp.3893-3901.
- Singh, D.K. and Panigrahi, P.K., 2015. Three-dimensional investigation of liquid slug Taylor flow inside a micro-capillary using holographic velocimetry, *Experiments in Fluids*, *56*(1), pp.1-15.
- Smith, C.R. and Metzler, S.P., 1983. The characteristics of low-speed streaks in the near-wall region of a turbulent boundary layer. *Journal of Fluid Mechanics*, *129*, pp.27-54.
- Soodt, T., Schröder, F., Klaas, M., van Overbrüggen, T. and Schröder, W., 2012. Experimental investigation of the transitional bronchial velocity distribution using stereo scanning PIV. *Experiments in fluids*, *52*(3), pp.709-718.
- Soulez, F., Denis, L., Fournier, C., Thiébaut, É. and Goepfert, C., 2007. Inverse-problem approach for particle digital holography: accurate location based on local optimization. *JOSA A*, *24*(4), pp.1164-1171.

- Soria J and Atkinson C 2008 Towards 3C-3D digital holographic fluid velocity vector field measurement: tomographic digital holographic PIV (tomo-HPIV) *Measurement Science Technology 19*(7), 074002
- Sullivan, J., Katz, J., Talapatra, S., Twardowski, M., Hong, J. and Donaghay, P., 2011, June. Using in-situ holographic microscopy for ocean particle characterization. In *OCEANS, 2011 IEEE-Spain* (pp. 1-6). IEEE.
- Schultz, M. P. and Flack, K. A., 2007, The rough-wall turbulent boundary layer from the hydraulically smooth to the fully rough regime. J. Fluid Mech. **580**, 381–405.
- Talapatra, S. and Katz, J., 2012. Three-dimensional velocity measurements in a roughness sublayer using microscopic digital in-line holography and optical index matching. *Measurement Science and Technology*, *24*(2), p.024004.
- Tian, L., Loomis, N., Domínguez-Caballero, J.A. and Barbastathis, G., 2010. Quantitative measurement of size and three-dimensional position of fast-moving bubbles in air-water mixture flows using digital holography. *Applied optics*, *49*(9), pp.1549-1554.
- Toloui M, Lai W, Troolin D and Hong J 2015 3D Turbulent Flow Measurements Combining V3V and Digital Inline Holographic PIV *11th international symposium on Particle Image velocimetry* (Santa Barbra, USA).
- Toloui M and Hong J 2015 High fidelity digital inline holographic method for 3D flow measurements *Optics Express* 23, 27159-27173.
- Townsend, A. A., 1976. The Structure of Turbulent Shear Flow, 2nd ed. (Cambridge University Press, 1976).
- Volino, R.J., Schultz, M.P. and Flack, K.A., 2007. Turbulence structure in rough- and smooth-wall boundary layers. *Journal of Fluid Mechanics*, *592*, pp.263-293.
- Volino, R. J., Schultz, M. P. & Flack, K. A. 2011 Turbulence structure in boundary layers over periodic two- and three-dimensional roughness. J. Fluid Mech. 676, 172–190.
- Wereley, S.T. and Meinhart, C.D., 2010. Recent advances in micro-particle image velocimetry. *Annual Review of Fluid Mechanics*, *42*, pp.557-576.
- Westerweel, J., Elsinga, G.E. and Adrian, R.J., 2013. Particle image velocimetry for complex and turbulent flows. *Annual Review of Fluid Mechanics*, *45*, pp.409-436.
- Willert, C.E. and Gharib, M., 1992. Three-dimensional particle imaging with a single camera. *Experiments in Fluids*, *12*(6), pp.353-358.
- Yoon, S.Y. and Kim, K.C., 2006. 3D particle position and 3D velocity field measurement in a microvolume via the defocusing concept. *Measurement Science and Technology*, *17*(11), p.2897.

- Yu, X., Hong, J., Liu, C. and Kim, M.K., 2014. Review of digital holographic microscopy for three-dimensional profiling and tracking. *Optical Engineering*,*53*(11), pp.112306-112306.
- Zhang, C., Miorini, R. and Katz, J., 2015. Integrating Mach–Zehnder interferometry with TPIV to measure the time-resolved deformation of a compliant wall along with the 3D velocity field in a turbulent channel flow.*Experiments in Fluids*, *56*(11), pp.1-22.